

Two-particle correlations on transverse rapidity in Au+Au collisions at $\sqrt{s_{NN}} = 200$ GeV at STAR

Principal Authors:

Lanny Ray, ray@physics.utexas.edu

Alex Jentsch, alexmichaeljentsch@gmail.com

Michael Daugherty, mike.daugherty@acu.edu

Prabhat Bhattacharai, prabhatb@physics.utexas.edu

Elizabeth Oldag, elizabeth.oldag@gmail.com

Target Journal: Phys. Rev. C

Goals of the paper

Two-particle correlation measurements with respect to two-dimensional transverse momentum coordinates (p_{t1}, p_{t2}), for the particle production in relativistic heavy-ion collisions, allow access to certain aspects of the collision dynamics beyond that which can be studied using angular correlations alone. Measurements of two-particle correlations on transverse momentum together with two-dimensional angular correlations as functions of (p_{t1}, p_{t2}) allow a complete determination of two-particle correlations in these collisions. Here, we report non-identified charged-particle correlations from Au + Au minimum-bias collisions at $\sqrt{s_{NN}} = 200$ GeV taken with the STAR detector at the Relativistic Heavy-Ion Collider (RHIC). Correlations are presented for like-sign, unlike-sign and all charged-particle pairs, as well as for particle pairs whose relative azimuth angles are $< \pi/2$, $> \pi/2$, or including pairs with all relative azimuth angles. Complex correlation structures are observed which monotonically evolve with collision centrality. The all-charge, all-azimuth correlation measurements are compared with predictions of HIJING and EPOS. Implications of these new measurements and the comparisons to theory are discussed, focusing on the origin of transverse momentum fluctuations within the hydrodynamic paradigm, and on the relevance of fragmenting longitudinal and transverse partons. These new correlation measurements provide a unique vantage point for studying such effects.

Table of Contents

I. Analysis Details	3
A. Analysis method summary	3
B. Data sets	3
C. Analysis codes and locations	4
D. Event, track and track-pair cuts	5
E. Analysis steps	6
II. Pre-Factor	7
III. Systematic Uncertainties	10
A. Secondary particle contamination	10
B. Two-track inefficiency correction uncertainty	13
C. Pile-up filter and correction uncertainty	13
D. Z-vertex mixing bin width uncertainty	14
E. Conversion electron backgrounds	15
F. Correlation measure bias	17
G. Tracking efficiency dependences – RefMultCorr	18
H. Pre-factor errors	18
I. Combined errors	18
J. Plots of errors and offsets	18
K. Plots of individual error sources	25
IV. Pre-Factor Charge and Azimuth-Dependent Scale Factors	31
V. Resonance Contributions	32
VI. Additional Analysis	33
VII. Figures for the paper	34
References	41
Appendix A – Z-vertex and ZDC-rate Uncertainties	

Appendix B – Pre-Factor Statistical and Systematic Errors

I. Analysis Details

A. Analysis method summary

The correlation quantity used here was derived in Ref. [MCBias] in order to eliminate statistical bias as explained in this reference. The basic correlation quantity $\Delta\rho/\rho_{\text{ref}}$ was separately computed for like-sign and unlike-sign pairs using Eqs. (22) and (24) in [1] in terms of the number of same-event and mixed-event pairs, average charge-particle multiplicities, and event-wise charged-particle multiplicity weight factors which are needed to eliminate bias. Track pairs were also selected based on their relative azimuth angle corresponding to all angles, near-side pairs with $\Delta\phi < \pi/2$, and away-side pairs with $\pi/2 < \Delta\phi < \pi$. Pre-factors, defined in the present paper draft, were multiplied bin-by-bin over the 2D range. Transverse momentum coordinates are replaced with transverse rapidity y_t , where $y_t = \log[(p_t + m_t)/m_0] \sim \log(p_t)$, $m_t = \sqrt{(p_t^2 + m_0^2)}$ and m_0 is taken as the pion mass which effectively regulates the singularity at $p_t = 0$. Transverse rapidity coordinates are used to display the correlations in order to optimize visual access to both low- and higher-momentum structures and to provide a natural coordinate for studying transverse fragmentation. Correlations are displayed on 2D (y_{t1}, y_{t2}).

The mixed-event reference was constructed by filling buffers of events for normal and reverse magnetic field, within the same primary z-vertex bin and event-multiplicity sub-bin, by mixing track pairs from one event with those in the next two events listed in the buffer. This process continues until all events in the buffer have been used. The statistical errors for this specific type of event-mixing were derived in Ref. [2] and are proportional to the total number of same-event and mixed-event pairs in each transverse momentum bin. Errors for all charges, like-sign and unlike-sign combinations use standard, uncorrelated error propagation.

Event centrality was based on TPC primary track number using track cuts listed below, and the cuts defined in [3,4] for the Run 2, 200 GeV Au+Au minimum-bias data set. The same cuts were used for Run 4 because the STAR configurations were the same in Runs 2 and 4 and the multiplicity frequency distributions were consistent. The raw track multiplicity cuts and centrality binning are listed in the following Table I. The peculiar cross section ranges date back to the Run 2 analysis [3] where trigger inefficiency corrections were determined well after the data analysis was completed. We adopt those same centrality bins in the present analysis in order to match these new (y_t, y_t) correlations with the previous 2D angular correlation measurements.

B. Data sets

Run 4, 200 GeV, productionMinBias, runNumber > 5023098 (runs with a symmetric z-vertex window), production P05ic. This analysis was initially performed at the Texas Advanced Computing Cluster (TACC) in Austin, Texas. The final, bias corrected data analysis was conducted at the RHIC Computing Facility.

Raw Centrality (%)	Corrected Centrality (%)	Multiplicity N_{ch}	ν
90 - 100	84 - 93	2 - 14	1.40
80 - 90	74 - 84	15 - 34	1.68
70 - 80	64 - 74	35 - 67	2.00
60 - 70	55 - 64	68 - 116	2.38
50 - 60	46 - 55	117 - 151 152 - 186	2.84
40 - 50	38 - 46	187 - 233 234 - 280	3.33
30 - 40	28 - 38	281 - 340 341 - 401	3.87
20 - 30	18 - 28	401 - 450 451 - 500 501 - 550	4.46
10 - 20	9 - 18	551 - 613 614 - 675 676 - 738	5.08
5 - 10	5 - 9	739 - 795 796 - 851	5.54
0.25 - 5	0 - 5	852 - 901 902 - 951 952 - 1001	5.95

Table I: Raw TPC track multiplicity cuts versus centrality for Run 4.

C. Analysis codes and locations

The basic steps in calculating the two-particle correlation is contained in the Event Structure analysis code, in CVS under StRoot/StEStructPool. The command to execute this phase is essentially:

```
.x doEStruct.C("list1.list","$SCRATCH","$SCRIPTSDIR",0)
```

where list1.list is a list of MuDSTs, \$SCRATCH points to the scratch directory where the data will be stored until it is copied to a permanent directory, and \$SCRIPTSDIR points to the directory where the cut-file ,Cuts.txt, exists. Cuts.txt contains all of the track, event, and pair cuts. The exact copy of doEstruct.C used in these analyses can be found at RCF in:

```
"/star/institutions/uta/ewingf2/codeForTechnicalNote/data/phase1/mode3AuAu200noPileUpFullField/scripts/"
```

After running doEstruct.C output is stored in a “data/” directory with files called dataHistsM01.root where M0 refers to the multiplicity bin 0, and 1 corresponds to the list number (list1.list). Also, QA and cutHists root files will be generated with general information

about the events and cuts. Four passes are made through the data in phase 1 for the configurations: Reversed Full Field with pileup filter, Full Field with pileup Filter, Reversed Full Field with no pileup Filter, and Full Field with no pileup filter. The pileup filter refers to eliminating events that have a potential pileup vertex less than 20 cm from the reconstructed primary vertex.

The source code is stored in StRoot in the directory
`“/star/institutions/uta/ewingf2/codeForTechnicalNote/”`.

Entire copies of example data are also in this directory labeled by the appropriate phase of the analysis chain.

Update to original analysis for bias correction: The statistical bias correction was worked out after the above instructions were written and are based on the method developed in [MCBias].
`StRoot/StEStructP ool/Correlations/StEStruct2ptCorrelations.cxx`

To address the new pair weighting algorithm root files:

`Run4RevFullFieldAveragesAndLannysFactor.root`

and

`Run4FullFieldAveragesAndLannysFactor.root`

are used in the .cxxfile. In the edited macro, the pairing scheme has been changed (see near the middle of the file). Yt-Yt correlations were measured keeping all parameters and cuts the same as described in the above four phases. The updated Estruct code is in the following location:

At UT Austin:

`libra:/data3/prabhatb/FinalAnalysisCodeAugust2016/LizsRun4VersionEStruct/EStructYtYtNormaliza`
`tionUsingMeanPt`

At RCF:

`rcas:/star/u/prabhatb/LizsRun4VersionEStruct/EStructYtYtNormalizationUsingMeanPt`

Monte Carlo code versions: HIJING, version 1.382; EPOS, version 3.210(c)

D. Event, track and track-pair cuts

```
# ****
# ***** Event Cuts *****
# *** format = variable,minvalue,maxvalue ***
# ****
centrality,1,2000      #centrality cut, number of tracks in |eta| < 0.5.
triggerWord,AuAu200GeVProductionMinBiasB2004      #Trigger tag for 2004
ProductionMinBias, runnumber > 5023098, AuAu data at 200GeV.
```

```

primaryVertexZ,-25,25      #cut on position of primary vertex.
pileup,-20,20      #Exclude events with predicted pileup vertex between min
and max distances..

# ****
# ***** Track Cuts *****
# *** format = variable,minvalue,maxvalue ***
# ****
Flag,0,2000      #Require good flag.
Charge,-1,1      #charge cut.
NFitPoints,15,50      #Number of fit points.
NFitPerNMax,0.52,1.1      #Ratio of Fit points / Maximum points on track.
GlobalDCA,0.0,3.0      #DCA of global track.
Chi2,0.0,3      #chi squared cut.
Pt,0.15,15.45      #pt cut.
Phi,-1,1      #phi cut.
Eta,-1,1      #eta cut.
NSigmaElectron,-1.5,1.5      #electron cut.

# ****
# ***** Pair Cuts *****
# *** format = variable,value1,value1 ***
# ****
GoodDeltaZDeltaXY,50,50      #dZ, dXY: Pairs with larger separation on either
variable never get cut.
Merging2,5,5      #mid TPC Z, XY separations (Usually 5cm).
Crossing2,5,5      #Mid, Exit TPC Z separations for tracks that crossed in phi
(usually 5cm) .

```

E. Analysis steps

Phase 1: The first step is to produce pair count histograms, which will later be combined to form correlations. All of the accepted tracks within an event (cuts described below) are formed into all possible unique pairs and binned in a histogram as a function of transverse rapidity. These are called same-event, or sibling pairs, as they come from the same event. Mixed event pairs are also produced using two particles from different events as explained above. Events are only mixed if they fall within the same multiplicity bin (centrality bins are subdivided into multiplicity bins if they are greater than approx. 50 tracks wide), and if they fall in the same primary z-vertex bin (10 bins were used in the three most central centrality fractions to cover the full range of -25 to +25 cm). Two mixed-events are produced for each event processed. Separate sibling and mixed pair count histograms are made for each of the four charge combinations: + +, + -, - +, and - -. The event, track, and pair cuts are described next. In summary, the track cuts are: $p_t > 0.15 \text{ GeV}/c$, $|\eta| < 1.0$, global DCA $< 3 \text{ cm}$, $15 < \text{NFitPoints} < 50$, $0.52 < \text{NfitPerNMax} < 1.1$, $0 < \text{Flag} < 2000$. There is also a cut applied to suppress electron/positron pairs by excluding particles with $\text{NsigmaElectron} < 1.5$ if $0.2 < p < 0.45 \text{ GeV}/c$ or $0.7 < p < 0.8 \text{ GeV}/c$. The events are selected in the primary vertex range $|z| < 25\text{cm}$. Two, track-pair cuts are used. A track merging cut excludes pairs (both sibling and mixed) if the separation distance in the TPC is $< 5 \text{ cm}$ in the x-y plane and $< 5 \text{ cm}$ in the z plane at three check points. A track crossing cut excludes pairs with a separation distance in the TPC of $< 35 \text{ cm}$ in the x-y plane and $< 5 \text{ cm}$ in the z plane only if the pair may

cross (in detail: Delta-Phi and Delta-P_t have opposite signs for ++ pairs or the same signs for -- pairs, Delta-Phi is positive for +- pairs or negative for -+ pairs) for three check points.

Centrality is complicated by the fact that refMult cannot be used in this analysis owing to artifacts introduced in the η -dependence of the correlations when event multiplicity is constrained within a smaller pseudorapidity range (see Ref. [5]). Instead, we produced multiplicity distributions based on the event and track cuts, estimate trigger and primary event reconstruction inefficiency, account for multiplicity dependent track reconstruction efficiency, and integrate the corrected multiplicity frequency distribution to get the centrality bins. The mapping is listed in Refs. [4,6,7]. By matching the corrected distribution to a Monte Carlo Glauber simulation [8] estimates of bin-averaged impact parameter, N_{part} , and N_{bin} , were determined for each centrality bin. For example, the original uncorrected 90-100% centrality bin, based on the raw multiplicity frequency distribution, is estimated to actually measure 84-93%.

Phase 2: The histograms of Full and Reversed Field data are kept separate but stored in one root file. This is done with the “addCentralities.C” macro. The pileup filter and no pileup filter configurations are kept completely separated. The bias corrected normalization is done in the combineHistograms3.C macro and the actual normalization code is in Support/StEStructSupport.cxx (but see below for the update information). Then we divide the same-event histograms by the corresponding mixed-event histogram to form a ratio and these ratios are combined across all z-vertex bins and all multiplicity bins (if the centrality has been subdivided), while separating reverse field and full field, using a weighted average based on the total number of same-event pairs. The different charge and angle combinations near-side, away-side, like-sign, unlike-sign (NS, AS, LS, US) are added together and the factors listed in the paper draft are applied in order to produce the charge-independent (CI) and charge-dependent (CD) correlations.

Phase 3: The efficiency of the pileup filter is estimated to be about 75%. The ratio, $\Delta\rho/\rho$, can be extrapolated to a fully pileup corrected sample by solving two equations outlined in Ref. [3]. This extrapolation procedure is done by running the macro “subtractPileup.C” where the input is the root file for the data with and without the pileup filter. The output is the final version of the data in the form $\Delta\rho/\rho$.

Phase 4: Next the value of $\Delta\rho/\rho$, which is the ratio of the number of same-event minus mixed-event pairs divided by mixed-event pairs, is multiplied by a prefactor. The prefactor, $P^{\text{CI,all-azimuth}}$ is fully explained in the paper draft.

II. Pre-Factor

The charge-particle pre-factor is an essential part of the correlation measurement which is required to remove the “volume,” or system size dependence. Other definitions, such as the “soft pre-factor” require further motivation and will no longer be used in the analysis and paper. The charge pre-factor does include statistical and systematic errors which must be included in the

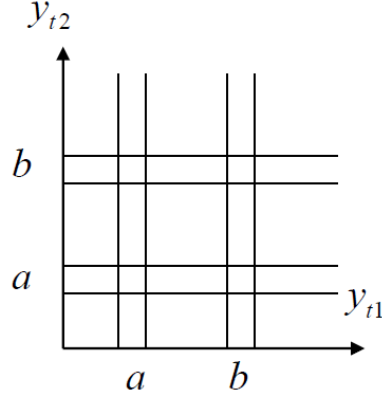
reported measurements. In particular, the correlation peak near $(y_t, y_t) = (3, 3)$ is not an arbitrary structure created by the pre-factor. For example, the correlation maximum at this specific transverse momentum, or rapidity, has physical meaning, namely the peak shows where the maximum number of correlated pairs occur relative to the number of particle, or precisely, the geometric mean of the product of the number of particles in the bins at y_{t1} and y_{t2} . As such, these measurements impose physically meaningful constraints on models.

The starting point for two-particle correlations is the normalized (within the range $[-1, +1]$) covariance:

$$\frac{\langle (n_{a1} - \langle n_{a1} \rangle)(n_{b2} - \langle n_{b2} \rangle) \rangle}{\sqrt{\sigma_{a1}^2 \sigma_{b2}^2}} = \frac{\langle n_{a1} n_{b2} \rangle - \langle n_{a1} \rangle \langle n_{b2} \rangle}{\sqrt{\sigma_{a1}^2 \sigma_{b2}^2}}$$

$$\xrightarrow{\text{Poisson}} \frac{\langle n_{a1} n_{b2} \rangle - \langle n_{a1} \rangle \langle n_{b2} \rangle}{\sqrt{\langle n_{a1} \rangle \langle n_{b2} \rangle}} \equiv \frac{\Delta\rho}{\sqrt{\rho_{ref}}}$$

Where n_a is the number of particle in single-particle bin a , $n_a n_b$ is the number of pairs in 2D bin (a, b) , subscripts 1 and 2 denote particle labels, σ^2 is the variance of the event-wise distribution of particle number in a bin, and brackets indicate event averages over all events in the centrality bin of the event ensemble. The 2D binning and labels are shown in the following diagram.



In the last step in the above equation the Poisson limit is assumed for the variances. The normalized covariance, or Pearson's correlation, is bounded from $[-1, +1]$ regardless of the number of particles in the system. The quantity $\Delta\rho/\rho_{ref}$ however, is not and scales with inverse multiplicity. Continuing with the Poisson limit produces the useful form of the normalized covariance given by

$$\begin{aligned}
\frac{\langle n_{a1}n_{b2} \rangle - \langle n_{a1} \rangle \langle n_{b2} \rangle}{\sqrt{\langle n_{a1} \rangle \langle n_{b2} \rangle}} &= \frac{\langle n_{a1} \rangle \langle n_{b2} \rangle}{\sqrt{\langle n_{a1} \rangle \langle n_{b2} \rangle}} \frac{\langle n_{a1}n_{b2} \rangle - \langle n_{a1} \rangle \langle n_{b2} \rangle}{\langle n_{a1} \rangle \langle n_{b2} \rangle} \\
&= \underbrace{\sqrt{\langle n_{a1} \rangle \langle n_{b2} \rangle}}_{\text{Estimate this with efficiency and acceptance corrected single-particle spectra data. We use either a Levy model or the event-average number of particles per } y_T \text{ bin.}} \underbrace{\frac{\langle n_{a1}n_{b2} \rangle - \langle n_{a1} \rangle \langle n_{b2} \rangle}{\langle n_{a1} \rangle \langle n_{b2} \rangle}}_{\text{Estimate this ratio using the pileup and two-particle tracking efficiency corrected pair data } \rho_{se} \text{ and } \rho_{me}.}
\end{aligned}$$

The spectra data used to form the above pre-factor include statistical fluctuations which co-vary with the fluctuations in quantity $\Delta\rho/\rho_{\text{ref}}$, given by the second factor on the RHS of the previous equation. The combined statistical errors are derived and discussed in Appendix B. For the measured correlations the tracking efficiency, acceptance and secondary particle contamination must be accounted for. The Levy model estimates include these corrections. The resulting systematic uncertainties in the corrected spectral distributions add to the total systematic uncertainty in the final correlation quantity $\Delta\rho/\sqrt{\{\rho_{\text{chrg}}\}}$ as discussed in Appendix B.

For increasing p_T it is increasingly likely that particle pairs are correlated, e.g. emitted from the same source such as a jet in the TCF model, or from a hot-spot or out-flowing plume in the BW language. The number of correlated pairs per particle must increase as p_T increases because the fraction of correlated pairs, relative to the total, is increasing when jets, hot spots or flowing plumes are present.

However, as p_T continues to increase the event-averaged number of correlated pairs will fall-off, even if the probability is increasing that those pairs which are found at higher p_T are correlated. The fall-off in pair number is faster than the fall-off in single particle number, hence the steady increase of the normalized covariance with p_T must reach a maximum and then fall-off.

The peak shows a physically meaningful quantity – it is where the number of correlated pairs relative to the number of particles is maximum. A numerical value of 1 would mean that the system, at that p_T , is maximally correlated, or that all the particles at that p_T are correlated. That puts a severe requirement on models.

III. Systematic Uncertainties

Initial estimates of systematic uncertainty in the data are described in Elizabeth Oldag's Ph.D. Thesis [6] Sec 5.5.1, page 109, and the magnitudes of several effects are shown in Ref. [9]. Other systematic offsets and uncertainties not discussed in the above thesis are discussed and presented below.

All known sources of systematic error encountered in previous correlation analysis from STAR were considered. Uncertainties caused by primary vertex lateral and longitudinal position resolution, z-vertex position dependence in the TPC (within the $|z| < 30$ cm acceptance), transverse momentum resolution, TPC central membrane crossing, large scale hardware time dependence during runs, possible intermittent TPC FEE outages during runs, multiplicity bin widths for event mixing, and uncorrected acceptance effects associated with charge-pair combinations and normal, reverse magnetic field direction were considered and found to negligible [3].

The remaining systematic uncertainties are discussed below. Some pertain only to nearside pairs, or only to unlike-charge-sign pairs etc. Also the prefactor differs in magnitude depending on the charges and relative azimuthal range for the particle pairs. The prefactor itself has both statistical and systematic uncertainties. But these are not correlation uncertainties, which is the topic considered in this note, but they do affect the overall magnitudes of the correlation quantity. Systematic variations in the estimates of $dN_{\text{soft}}/dy_t d\eta$ are presented in E. Oldag's thesis [6], in Sec 5.5.2 and in Fig. 5.19.

A. Secondary particle contamination

Weak decay daughter particles from the collision and particle production in the detector material which are mistakenly identified as primary particles from the collision contribute secondary backgrounds. The correlations among these secondary particles and between secondary and true primary particles is not known and may contribute to the measurement. The p_T distributions of primary and secondary particles have different shapes which have been measured for the present collision system [10]. Event-wise fluctuations in the relative magnitude of the secondary particles generate correlations. In addition, decay kinematics and scattering in the detector material will distort and likely will dissipate the correlations among the secondary particles generated by true primary parent particles. Both effects are estimated as described in the paper draft and below.

For event-wise fluctuations in the relative yield of secondary particles, the measured charge distribution is assumed to have the form

$$\frac{d^2N}{dy_t d\eta} = \bar{N} [(1 - \bar{\alpha}) \hat{\rho}_{\text{prim}}(y_t) + \bar{\alpha} \hat{\rho}_{\text{sec}}(y_t)]$$

in terms of the unit-normalized true-primary and secondary particle p_T distributions and average secondary contamination factor $\bar{\alpha} = 0.12$ for the RUN 4 STAR detector configuration and reconstruction assuming a 3 cm DCA cut on primaries. The average pair distribution is given by

$$\begin{aligned} \frac{d^4 N_{12}}{dy_{t1} d\eta_1 dy_{t2} d\eta_2} &= \bar{N}(\bar{N} - 1) \\ &\times \{[(1 - \bar{\alpha})^2 + \sigma_\alpha^2] \hat{\rho}_{\text{prim}}(y_{t1}) \hat{\rho}_{\text{prim}}(y_{t2}) \\ &+ (\bar{\alpha}^2 + \sigma_\alpha^2) \hat{\rho}_{\text{sec}}(y_{t1}) \hat{\rho}_{\text{sec}}(y_{t2}) \\ &+ [\bar{\alpha}(1 - \bar{\alpha}) - \sigma_\alpha^2] (\hat{\rho}_{\text{prim}}(y_{t1}) \hat{\rho}_{\text{sec}}(y_{t2}) \\ &+ \hat{\rho}_{\text{prim}}(y_{t2}) \hat{\rho}_{\text{sec}}(y_{t1}))\} \end{aligned}$$

where σ_α^2 is the variance of the event-wise distribution of α , assumed to be Poisson. The correlations resulting from event-wise fluctuations in α , for CI, all-azimuth are

$$\begin{aligned} \frac{\Delta\rho}{\sqrt{\rho_{\text{soft}}}}(y_{t1}, y_{t2})_{\text{sec}} &= \mathcal{P}_{12}^{\text{CI,All}}(y_{t1}, y_{t2}) \\ &\times \left[\frac{\frac{d^4 N_{12}}{dy_{t1} d\eta_1 dy_{t2} d\eta_2}}{\frac{\bar{N}-1}{\bar{N}} \frac{d^2 N}{dy_{t1} d\eta_1} \frac{d^2 N}{dy_{t2} d\eta_2}} - 1 \right]. \end{aligned}$$

The pion and proton secondary particle relative fractions (kaons and antiproton contributions are negligible) are plotted in Fig. 16 and listed in Table V, respectively, in Ref. [10]. These distributions were fitted with simple functions over the given p_T ranges, given by

$$\begin{aligned} F_{\text{sec}}^{\pi^\pm}(p_t) &= 0.04 + 0.155e^{-3.57(p_t - 0.15)} \\ F_{\text{sec}}^{\text{proton}}(p_t) &= -1.15(p_t - 0.15) + 0.65, \\ &\quad \text{for } 0.15 \leq p_t \leq 0.575 \\ &= 0.153e^{-8(p_t - 0.575)}, \quad p_t > 0.575 \end{aligned}$$

where p_T is in units of GeV/c . The overall fraction of charged pions and protons are $f_\pi = 0.85$ and $f_p = (0.53)(0.062)$. The secondary particle distribution is given by

$$\begin{aligned} \frac{d^2 N_{\text{sec}}}{dy_t d\eta} &= 2\pi p_t m_t \frac{d^2 N_{\text{ch}}}{2\pi p_t d p_t d\eta} \\ &\times \left[f_\pi F_{\text{sec}}^{\pi^\pm}(p_t) + f_p F_{\text{sec}}^{\text{proton}}(p_t) \right] \end{aligned}$$

where the total charged particle distributions in each centrality bin are parametrized by Levy distributions whose parameters are listed in Table II in the paper draft. Assuming Poisson fluctuations in the secondary particle yield, gives

$$\sigma_\alpha^2 = (\Delta N_{\text{sec}})^2 / \bar{N}^2 \approx \bar{N}_{\text{sec}} / \bar{N}^2 = \bar{\alpha} / \bar{N}.$$

This estimated secondary particle contribution is treated as an uncertainty, rather than a correction. One-half of the secondary particle correlation is subtracted from the data in each (y_t, y_t) bin and $\pm 1/2$ of the magnitude in each bin is considered a systematic uncertainty, thus encompassing the entire effect in each (y_t, y_t) bin.

To estimate the correlation contribution from event-wise fluctuations in the shape of the secondary particle distribution we express the single-particle distribution, the pair distributions, the correlations for primary particles only and for all particles including secondaries, and the secondary particle contribution as follows:

$$\begin{aligned} \frac{dN}{dy_t d\eta} &= \frac{dN_{prim}}{dy_t d\eta} [1 + F_{sec}(p_t)] \\ \frac{dN_{se}}{dy_{t1} d\eta_1 dy_{t2} d\eta_2} &= \frac{dN_{se, prim}}{dy_{t1} d\eta_1 dy_{t2} d\eta_2} + \frac{dN_{se, sec}}{dy_{t1} d\eta_1 dy_{t2} d\eta_2} [F_{sec}(p_{t1}) + F_{sec}(p_{t2}) + F_{sec}(p_{t1})F_{sec}(p_{t2})] \\ \frac{dN_{me}}{dy_{t1} d\eta_1 dy_{t2} d\eta_2} &= \frac{dN_{prim}}{dy_{t1} d\eta_1} \frac{dN_{prim}}{dy_{t2} d\eta_2} [1 + F_{sec}(p_{t1}) + F_{sec}(p_{t2}) + F_{sec}(p_{t1})F_{sec}(p_{t2})] \\ \frac{\Delta\rho_{primary}}{\sqrt{\rho_{soft}}} &= P_{12}^{CI, All} \left[\frac{\frac{dN_{se, prim}}{dy_{t1} d\eta_1 dy_{t2} d\eta_2}}{\frac{dN_{prim}}{dy_{t1} d\eta_1} \frac{dN_{prim}}{dy_{t2} d\eta_2}} - 1 \right] \\ \frac{\Delta\rho}{\sqrt{\rho_{soft}}} &= P_{12}^{CI, All} \left[\frac{\frac{dN_{se, prim}}{dy_{t1} d\eta_1 dy_{t2} d\eta_2}}{\frac{dN_{me}}{dy_{t1} d\eta_1 dy_{t2} d\eta_2}} - 1 \right] \\ \frac{\Delta\rho_{sec}}{\sqrt{\rho_{soft}}} &= \frac{\Delta\rho}{\sqrt{\rho_{soft}}} - \frac{\Delta\rho_{primary}}{\sqrt{\rho_{soft}}} \end{aligned}$$

The first equation defines the secondary particle distribution relative to that of the true primaries via quantity F_{sec} . The second equation introduces the two-particle same-event (se) distributions for primaries and for secondaries where we assume the same functional form for secondary – primary pairs and for secondary – secondary pairs. The final correlation quantity is the estimated secondary particle contribution to the measured correlations. Both pair distributions are assumed to be described by the 2D-Levy distribution [11] where the variance shifts, $\Delta(1/q)_{Vol}$ and $\Delta(1/q)_{cov}$, for primary particle pairs are assumed from the blast-wave model fits [12].

For secondary pairs we assume that the weak decay kinematics and scattering in the detector material weakens the correlation strength inherited from the primary parent particle, corresponding to a reduced covariance $\Delta(1/q)_{cov}$. The larger the decay Q-values and the more energy/momentum transferred in particle production, the more reduction we expect in the correlation amplitude. Typical Q-values for the dominant weak decays are of order 0.2 GeV and

typical momentum transfer for particle production (pions) and proton knock-out reactions in the detector material are also of order a few hundred MeV. Typical momentum for primaries is about 0.5 to 1 GeV/c, and we estimate a range of reduction of order 0.2/0.5 to 0.2/1.0, or a 30% reduction in $\Delta(1/q)_{\text{cov}}$ for secondary pairs. This crude estimate would not be sufficient if the effects were significant. However, as shown in the figures below the systematic shifts in the correlations based on these estimates are negligible.

B. Two-track inefficiency correction uncertainty

Two-track reconstruction efficiency is not simply the product of single track efficiencies as there are additional effects, e.g. merging and crossing, which adversely affect the pair reconstruction. Correction procedures are based on removing tracks which overlap within the TPC tracking volume. Those corrections are imperfect, resulting in some residual systematic uncertainty in the data. We estimate this possible residual as the difference between correlations, for the same data, computed using two variants of the correction procedure detailed in Michael Daugherty's Ph. D. Thesis [4]. The difference between the two methods involves the number of positions in the TPC where track separation distances are checked. One uses the average separations at three positions near the entrance, exit and mid-radius of the TPC; the other uses only the mid-radius [3]. The correlation differences display a slight depression from $y_t = 1.5$ to 3 of order -0.005 for bins 4-7. The best way to judge the efficacy of the two-track inefficiency cuts is with the angular correlations near the (0,0) origin. Comparing the 200 GeV Au+Au axial CI data in Mike Daugherty's thesis (Fig.6.3, p.121) using the three-position averaging method, with the published data [3], which used the mid-radius cut, we estimate that the remaining uncertainty in the two-track inefficiency correction is about $\pm 1/3$ of the above correlation difference. The systematic uncertainty in the $(y_t, y_t) \Delta\rho/\sqrt{\rho_{\text{soft}}}$ data can be modeled by a 2D Gaussian:

$$\pm 0.002 e^{-\frac{1}{2}[(y_{t1}-y_{t0})^2 + (y_{t2}-y_{t0})^2]/\sigma^2}$$

for centrality bins 18-55% and zero elsewhere. The parameters are:

cent.(%)	y_{t0}	σ	where
46-55	2.3	0.5	$y_t = \log\left(\frac{p_t + m_t}{m_0}\right)$ (transverse rapidity)
38-46	2.3	0.5	
28-38	2.5	0.6	$m_t = \sqrt{p_t^2 + m_0^2}$; m_0 is particle mass; pion mass
18-28	2.6	0.7	assumed for non - identified particles.

C. Pile-up filter and correction uncertainty

The issue here is that some effects of pileup may persist after the vertex ranking, and Duncan Prindle's pileup filter, described in Ref. [3] and correction procedure have been done. The best way to estimate the amount of pileup contamination present in events is by viewing the centrality trend of the axial CI fit parameter A_0 , the 1D Gaussian amplitude on $\eta_1 - \eta_2$. Mike Daugherty's

thesis [4] Fig. 6.7, p. 127 shows the no-pileup corrected A_0 for the Run 4, 62 GeV Au+Au data. Scaling these results down to the Run 2 Au+Au 200 GeV A_0 fit parameters for the three most-peripheral bins provides an estimate of the Run 4, 200 GeV no-pileup corrected A_0 . Comparing that trend to the actual Run 4, 200 GeV Au+Au fitted results, including pileup filter and correction, allows an estimate of the possible, remaining pileup contamination in the present data. We estimate this amount to be about $\pm 10\%$ of the full pileup effect. Therefore the remaining uncertainty in the $(y_t, y_t) \Delta\rho/\sqrt{\rho_{\text{soft}}}$ data due to pileup correction is ± 0.1 times the difference between the data with no-pileup-filter and the final data. That is again reasonably well represented with a 2D Gaussian as in the preceding section with parameters:

cent.(%) \pm amplitude	y_{t0}	σ
64-74	0.0007	2.0
55-64	0.0018	2.1
46-55	0.0034	2.2
38-46	0.0040	2.2
28-38	0.0030	2.3
18-28	0.0007	2.3

and zero elsewhere.

D. Z-vertex mixing bin width uncertainty

The issue here is that the data may be affected by the choice of bin width along the beam axis in the TPC (z-axis) used for event mixing. The final data for the 8 least central bins (centrality bin numbers 0-7) did not require z-vertex sub-binning to achieve stable results; the three more central bins (numbers 8-10) required 5 cm binning. Comparing the (y_t, y_t) data for bins 0-7 with no z-vertex sub-binning (“final” data) with results assuming 5 cm binning shows a statistically significant increase in the correlations in the higher p_T corner for bins 1-7. For bins 8-10 comparing the standard 5 cm binning results to that with reduced 2 cm bin widths did not produce any statistically significant differences. The ideal limit of $\Delta z\text{-vertex} \sim 0$ is only approached in this study. Decreasing $\Delta z\text{-vertex}$ produces a net increase in $\Delta\rho/\sqrt{\rho_{\text{soft}}}$ at higher p_T . This suggests that the true values are slightly higher than the nominal data at larger y_t . A net offset and \pm uncertainty is therefore assigned to the data. An offset equal to half the difference between the reduced bin width results and the nominal width results was assumed where the uncertainty was set equal to the magnitude of the offset. The net shift in the $\Delta\rho/\sqrt{\rho_{\text{soft}}}$ data is approximated by an exponential, where

$$\begin{aligned}\text{Offset in data} &= 0.02e^{-|y_{\Sigma} - 8.5|/0.2}, \text{ if } y_{\Sigma} < 8.5 \\ &= 0.02, \text{ if } y_{\Sigma} \geq 8.5\end{aligned}$$

where $y_{\Sigma} \equiv y_{t_1} + y_{t_2}$

The uncertainty is \pm the above offset. These apply to bins 1-7 and are zero elsewhere.

E. Conversion electron backgrounds

Photon conversion to e^+e^- pairs in the detector material produce secondary particle background at the $\sim 1\%$ level and are subsumed in the above secondary particle contamination systematic estimates. However, the e^+e^- pairs from each photon conversion are correlated via the γ conversion dynamics in the detector material, and not by the A+A collision processes. Electron PID cuts remove some, but not all of these produced electrons. The remaining false correlations must be removed, or included as a systematic uncertainty. The latter is done in this analysis using a combination of Monte-Carlo and fits to unlike-sign 2D angular correlation data.

Simulations were carried out and reported in E. Oldag's Ph.D thesis [6] in which photons, from π^0 decays produced in the collision, underwent pair production according to the Bethe-Heitler equation [13]. Realistic π^0 momentum distributions were assumed and randomly oriented π^0 to $\gamma+\gamma$ decays were boosted to lab coordinates. The 1150 generated e^+e^- pairs were binned on (y_{t1}, y_{t2}) and symmetrized, generating a 2D distribution, $\rho_{\gamma \rightarrow e^+e^-}(y_{t1}, y_{t2})$.

The opening angle for the e^+e^- pairs is of order 1 degree which produces a visible, sharp spike in the 2D angular correlations for unlike-sign pairs, modeled with a 2D exponential [3], thus allowing estimates to be made of the average number of γ conversions per event. Electron pairs formed from daughters from different γ -conversions in the same event, and reference electron pairs from mixed-events are spread across the acceptance and contribute to the approximately uniform reference distribution. Neither contribute to the sharp, 2D exponential. Measurement of the volume of this sharp peak is therefore related to the average number of photon conversions per event which survive the DCA and dE/dx cuts. Monte-Carlo simulations of photon conversion using the Bethe-Heitler equation were used to simulate the transverse and angular momentum distribution of the electron pairs.

The average number of photon conversions per event was estimated from the sharp angular correlation (2D exponential) for unlike-sign particle pairs, where the per-particle correlation quantity for this specific structure is related to the number and distribution of photon conversion electron pairs as

$$\frac{\Delta\rho_{US,2D-\text{exp}}}{\sqrt{\rho_{ref,US}}}(\eta_\Delta, \phi_\Delta) = \frac{1}{\sqrt{2}} \frac{\bar{N}_{ch}}{2\pi\Delta\eta} \frac{2\bar{N}_\gamma \hat{\rho}_{\gamma \rightarrow e^+e^-}(\eta_\Delta, \phi_\Delta)}{\frac{1}{2}\bar{N}_{ch}^2 \hat{\rho}_{ref,US}(\eta_\Delta, \phi_\Delta)} = A_2 F_{2D-\text{exp}}(\eta_\Delta, \phi_\Delta)$$

where \bar{N}_{ch} is the average multiplicity in the acceptance, $\Delta\eta = 2$ is the pseudorapidity acceptance, \bar{N}_γ is the average number of photon conversions occurring within the acceptance, $\hat{\rho}_{\gamma \rightarrow e^+e^-}(\eta_\Delta, \phi_\Delta)$ is the simulated angular distribution of daughter e^+e^- pairs on difference variables $\eta_\Delta = \eta_1 - \eta_2$ and $\phi_\Delta = \phi_1 - \phi_2$. Both $\hat{\rho}$ distributions are normalized to unity over the entire 2D angular space, and $F_{2D-\text{exp}}$ is a 2D exponential used in fitting the angular correlations, given by [3]

$$F_{2D-\text{exp}}(\eta_\Delta, \phi_\Delta) = \exp \left\{ -[(\eta_\Delta / w_\eta)^2 + (\phi_\Delta / w_\phi)^2]^{1/2} \right\}$$

which for US pairs, is assumed to be dominated by conversion electron pairs. The factor of 2 in the numerator is included to count both permutations of particles 1 and 2; the factor $\frac{1}{2}$ in the denominator counts only US pairs; the factor of $\frac{1}{\sqrt{2}}$ in the pre-factor is for US pairs at all azimuth angles. The normalized, US pair acceptance "triangle" function is given by

$$\hat{\rho}_{ref,US}(\eta_\Delta, \phi_\Delta) = (1 - |\eta_\Delta| / \Delta\eta) / (2\pi\Delta\eta)$$

Solving for \bar{N}_γ yields

$$\bar{N}_\gamma = \sqrt{2} \bar{N}_{ch} A_2 \int_0^{\Delta\eta} d\eta_\Delta \int_0^\pi d\phi_\Delta F_{2D-\text{exp}}(\eta_\Delta, \phi_\Delta) (1 - |\eta_\Delta| / \Delta\eta)$$

Fits to the 18-28% Au + Au 200 GeV unlike-sign angular correlation data result in parameters: $A_2 = 0.27$, $w_\eta = 0.118$, and $w_\phi = 0.130$ [6]. With these parameters we estimate the efficiency corrected $\bar{N}_\gamma \approx 5$ which pass the DCA and dE/dx cuts. For the other centrality bins we assume that the average number of photon conversions is proportional to \bar{N}_{ch} .

The correlation estimate can be simplified by assuming each event has a fixed number of hadrons and γ conversions. In this case the single - particle distribution is

$$\bar{\rho}_{ch}(1) = \bar{N}_h \hat{\rho}_h(1) + \bar{N}_\gamma (\hat{\rho}_{e^+}(1) + \hat{\rho}_{e^-}(1)),$$

where $\hat{\rho}_h$ and $\hat{\rho}_{e^\pm}$ are unit normalized hadron and electron distributions on arbitrary coordinates 1 and 2. The same - event, pair distribution is

$$\begin{aligned} \bar{\rho}_{se}(1,2) &= \bar{N}_h (\bar{N}_h - 1) \hat{\rho}_{h,h}(1,2) + \bar{N}_h \bar{N}_\gamma (\hat{\rho}_{h,e^+}(1,2) + \hat{\rho}_{h,e^+}(2,1) + \hat{\rho}_{h,e^-}(1,2) + \hat{\rho}_{h,e^-}(2,1)) \\ &\quad + \bar{N}_\gamma (\bar{N}_\gamma - 1) (\hat{\rho}_{e^+,e^+}(1,2) + \hat{\rho}_{e^-,e^-}(1,2) + \hat{\rho}_{e^+,e^-}(1,2) + \hat{\rho}_{e^-,e^+}(1,2))_{\gamma \neq \gamma'} \\ &\quad + \bar{N}_\gamma (\hat{\rho}_{\gamma \rightarrow e^+ e^-}(1,2) + \hat{\rho}_{\gamma \rightarrow e^- e^+}(1,2))_{\text{same } \gamma} \end{aligned}$$

and the mixed - event pair distribution, normalized to $\bar{N}_{ch} (\bar{N}_{ch} - 1)$ pairs, is

$$\begin{aligned} \bar{\rho}_{me}(1,2) &= \bar{N}_h (\bar{N}_h - 1) \hat{\rho}_h(1) \hat{\rho}_h(2) + \bar{N}_h \bar{N}_\gamma (\hat{\rho}_h(1) \hat{\rho}_{e^+}(2) + \hat{\rho}_h(2) \hat{\rho}_{e^+}(1) + \hat{\rho}_h(1) \hat{\rho}_{e^-}(2) + \hat{\rho}_h(2) \hat{\rho}_{e^-}(1)) \\ &\quad + \bar{N}_\gamma (\bar{N}_\gamma - 1) (\hat{\rho}_{e^+}(1) \hat{\rho}_{e^+}(2) + \hat{\rho}_{e^-}(1) \hat{\rho}_{e^-}(2) + \hat{\rho}_{e^+}(1) \hat{\rho}_{e^-}(2) + \hat{\rho}_{e^-}(1) \hat{\rho}_{e^+}(2)) \\ &\quad + \bar{N}_\gamma (\hat{\rho}_{e^+}(1) \hat{\rho}_{e^-}(2) + \hat{\rho}_{e^-}(1) \hat{\rho}_{e^+}(2)) \end{aligned}$$

Quantity $\Delta \bar{\rho} = \bar{\rho}_{se}(1,2) - \bar{\rho}_{me}(1,2)$ contains true hadron - hadron correlations, secondary background correlations among hadrons and electrons, secondary background correlations of electrons from different photon conversions, and the correlations from the photon conversion electron daughters, given by

$$\Delta \rho_{\gamma \rightarrow e^+ e^-}(1,2) = 2 \bar{N}_\gamma (\hat{\rho}_{\gamma \rightarrow e^+ e^-}(1,2) - \hat{\rho}_{e^+}(1) \hat{\rho}_{e^-}(2))_{\text{same } \gamma}$$

The $\gamma + A \rightarrow e^+ + e^- + A'$ pair production process contribution to the measured correlations for the CI, all - azimuth in (y_{t1}, y_{t2}) space is

$$\frac{\Delta \rho}{\sqrt{\rho_{\text{soft}}}_{\gamma \rightarrow e^+ e^-}}^{\text{CI, all } \phi} = P^{\text{CI, all } \phi} \frac{\Delta \rho_{\gamma \rightarrow e^+ e^-}(y_{t1}, y_{t2})}{\bar{N}_{ch} (\bar{N}_{ch} - 1) \hat{\rho}_{ref}(y_{t1}, y_{t2})}$$

where $P^{\text{CI, all } \phi}$ is the pre - factor and $\hat{\rho}_{ref}$ is the unit normalized product $\bar{\rho}_{ch}(y_{t1}) \bar{\rho}_{ch}(y_{t2})$.

This contribution was subtracted from the measured correlations as a systematic offset and half the magnitude was assumed as a systematic uncertainty.

F. Correlation measure bias

Correlation measure bias due to multiplicity dependent p_t distribution slope was estimated. In Ref. [1] it was shown that multiplicity dependence in the overall slope of the single-particle p_t distribution biases the correlation measurement constructed within finite multiplicity bins. The

magnitudes for 200 GeV Au+Au peripheral and mid-central collisions were estimated using Monte Carlo simulations for like-sign, unlike-sign and CI correlations and are shown in Fig. 5 of Ref. [1]. Those results were smoothed and interpolated for all multiplicity sub-bins used in this analysis where the mid-central results were assumed for the remaining mid- to most-central bins. A systematic offset equal to minus one-half the systematic contribution estimate from Ref. [1] and a systematic uncertainty equal to one-half the magnitude of the simulated bias was taken and the systematic uncertainty contribution for the present data.

G. Tracking efficiency dependence - RefMultCorr

Tracking efficiency variation with z-vertex position and beam luminosity as estimated in RefMultCorr was studied for these data. The issue is that these additional inefficiencies reduce the apparent event multiplicities, systematically shifting the events in centrality and mixing in a broader range of correlations into a given centrality bin than should be. This systematic was studied and reported at the STAR meeting at BNL in May 2017 [14]. The relevant slides from that presentation are copied into Appendix A. The systematic effects are very small but are included in the total systematic uncertainties.

H. Pre-factor errors

Systematic uncertainties, deriving from those in the single particle spectra, contribute to the pre-factor and the total systematic uncertainties in the final correlations. These errors are discussed and estimated in Appendix B.

I. Combined errors

All systematic offsets were summed linearly and all systematic uncertainties were combined in quadrature, yielding asymmetric systematic uncertainty ranges in each (y_{t1}, y_{t2}) bin. The uncertainty ranges were extended in each bin, as necessary, to encompass the measured correlation value. In general the total systematic uncertainties vary from of order 10% of the overall scale of the correlation structures in the more-peripheral bins to about 5% in the more-central. Systematic uncertainties exceed the statistical errors at lower transverse rapidity up to about $y_t \approx 3$; statistical errors dominate at larger y_t .

J. Plots of errors and offsets

The CI, all-azimuth correlation data, statistical errors, systematic uncertainty, systematic offset and average total systematic uncertainty are shown on the following pages in Figs. 1-11 for all eleven centrality bins numbered 0-10 from peripheral to central, respectively. The correlations and errors shown in these plots include the charged-particle pre-factor and the systematic uncertainties in the charged pre-factor.

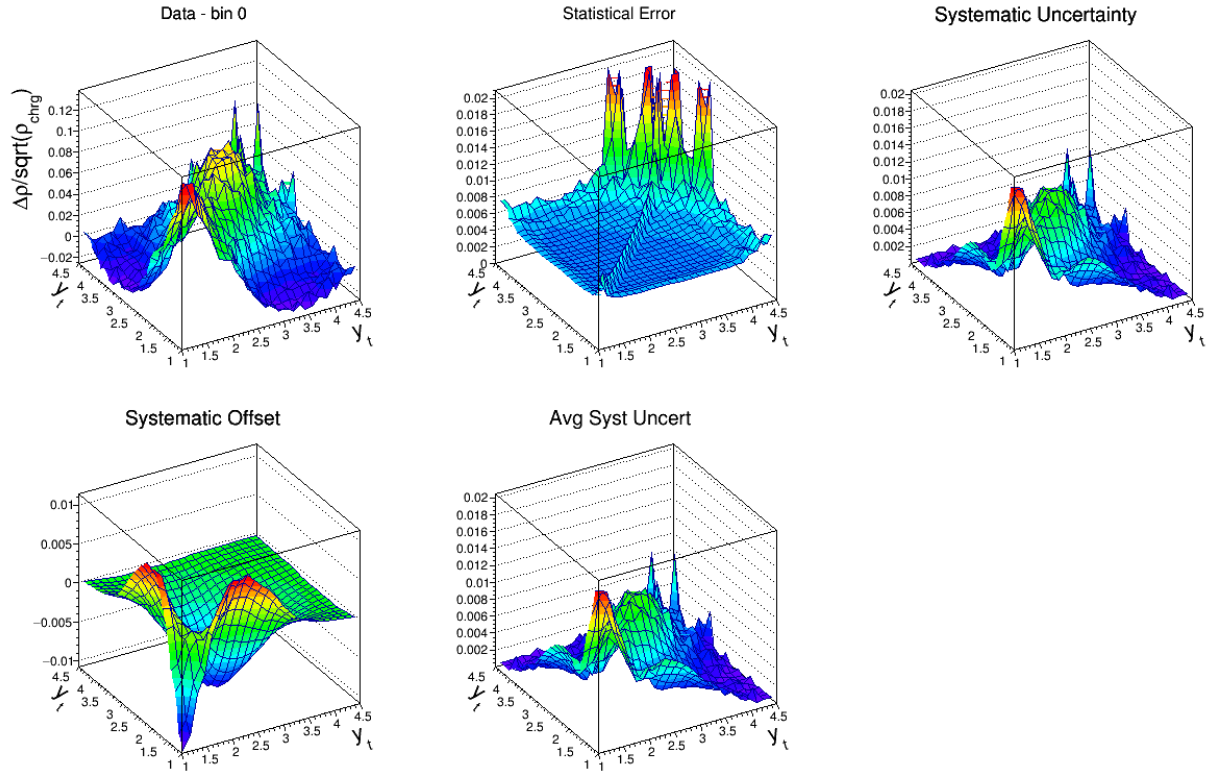


Fig. 1: Charge-independent, all-azimuth angle correlation data, statistical errors, \pm systematic uncertainty, systematic uncertainty offset, and average systematic uncertainty for the 84-93% centrality bin. The average systematic uncertainty includes the offset, and is approximately equal to the \pm systematic uncertainty in the third panel.

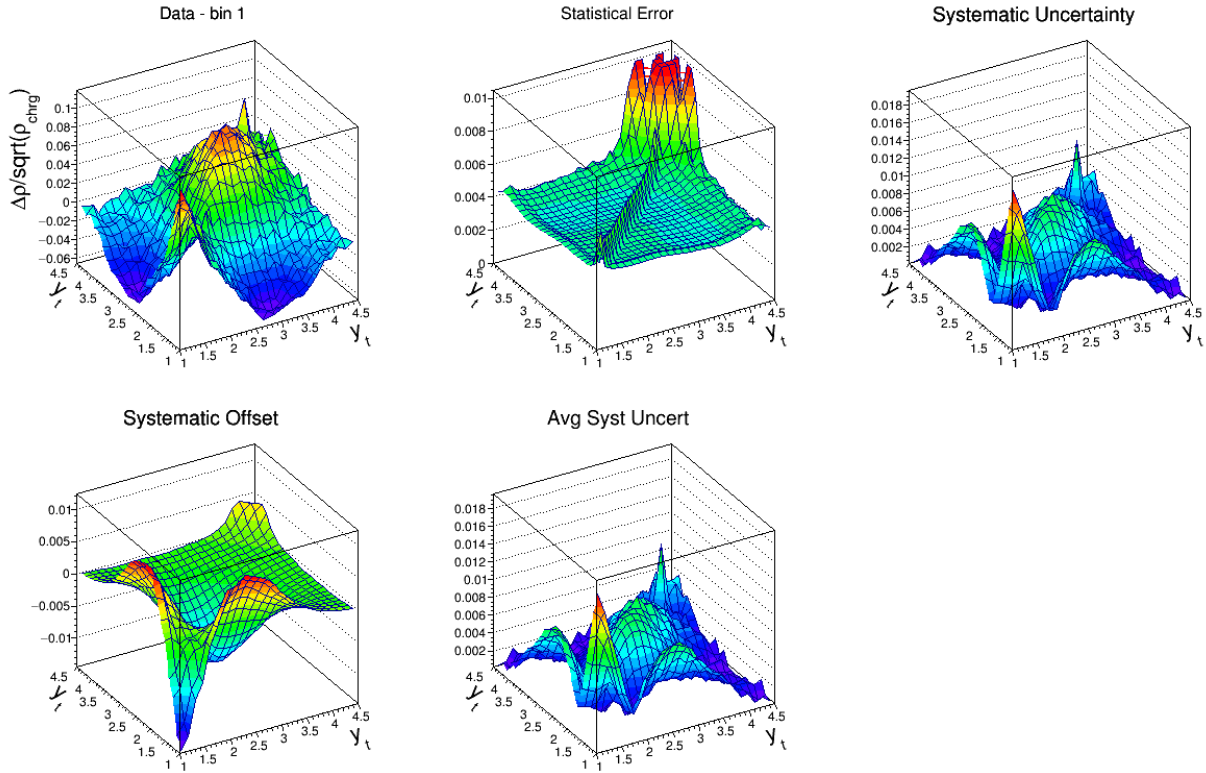


Fig. 2: Same as Fig. 1 except for the 74-84% centrality bin.

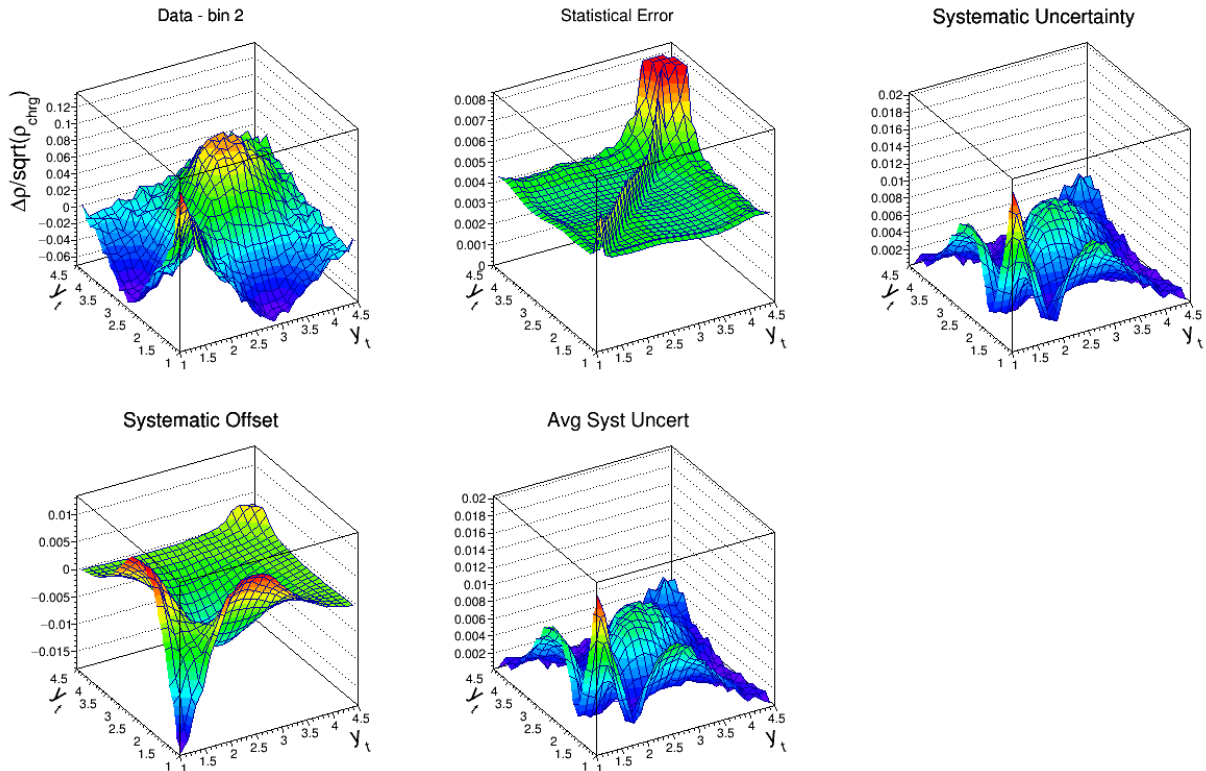


Fig. 3: Same as Fig. 1 except for the 64-74% centrality bin.

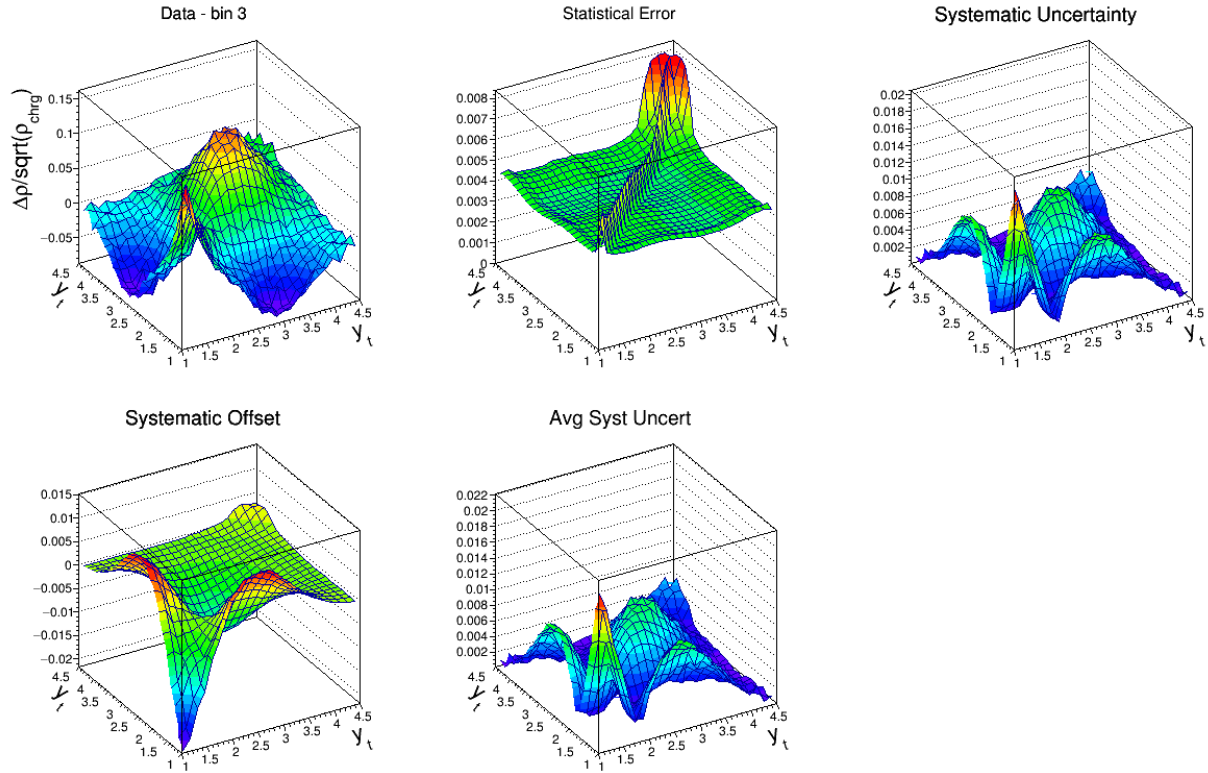


Fig. 4: Same as Fig. 1 except for the 55-64% centrality bin.

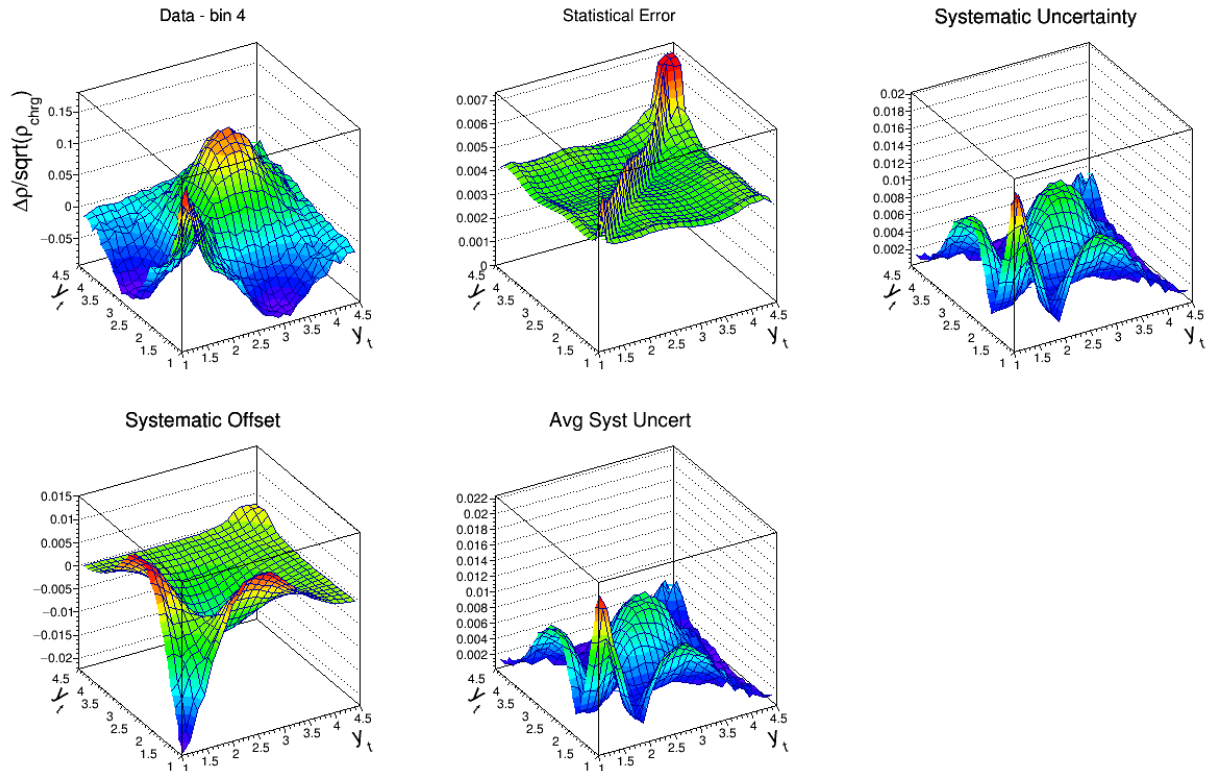


Fig. 5: Same as Fig. 1 except for the 46-55% centrality bin.

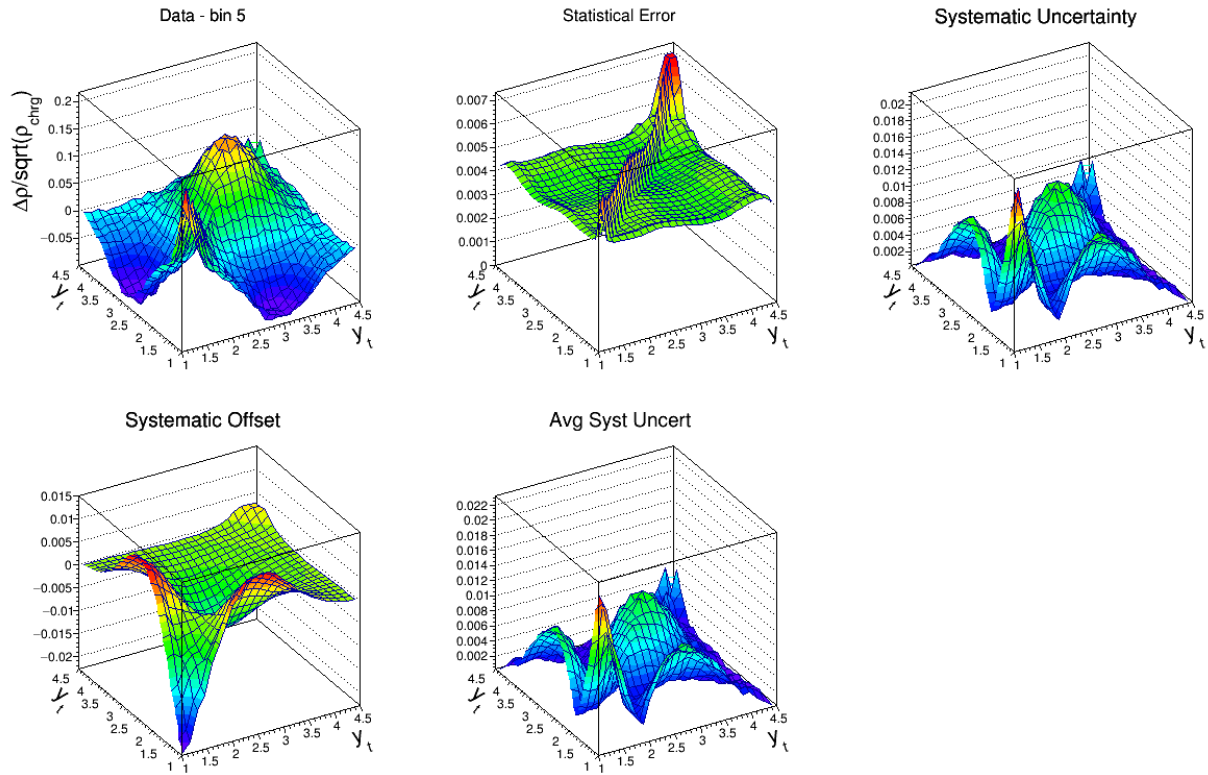


Fig. 6: Same as Fig. 1 except for the 38-46% centrality bin.

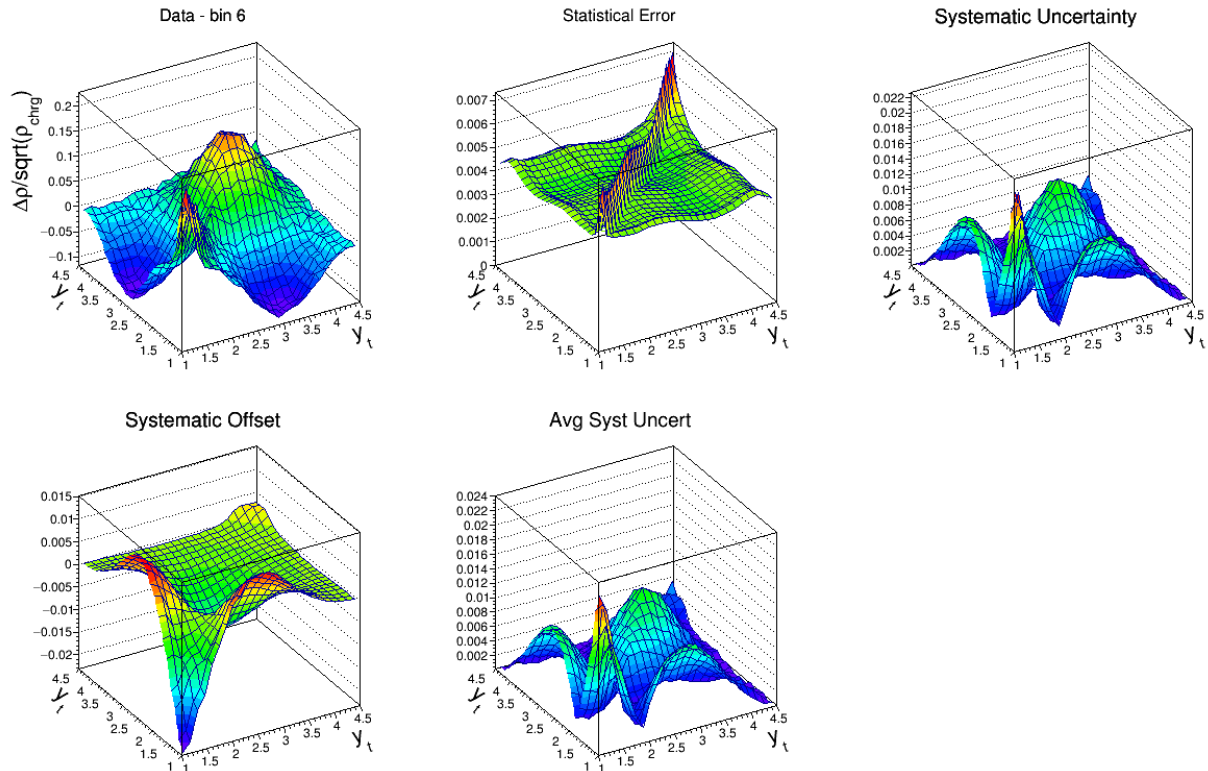


Fig. 7: Same as Fig. 1 except for the 28-38% centrality bin.

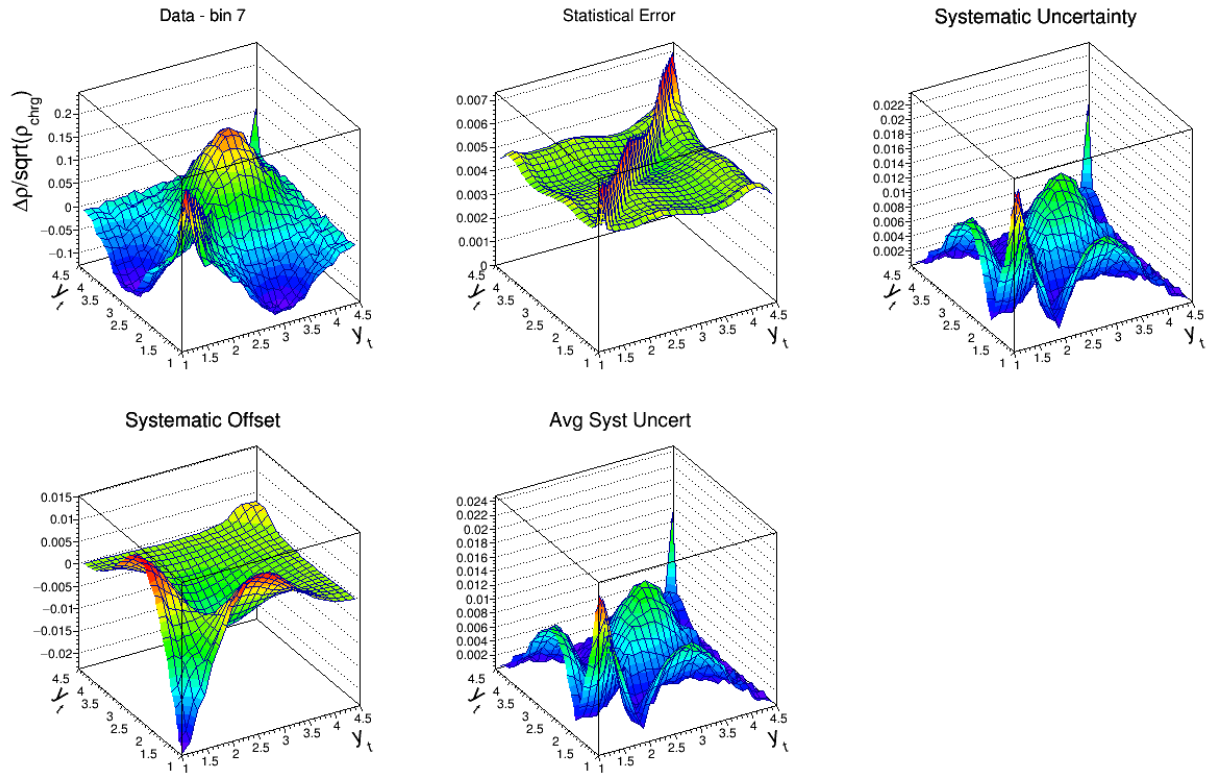


Fig. 8: Same as Fig. 1 except for the 18-28% centrality bin.

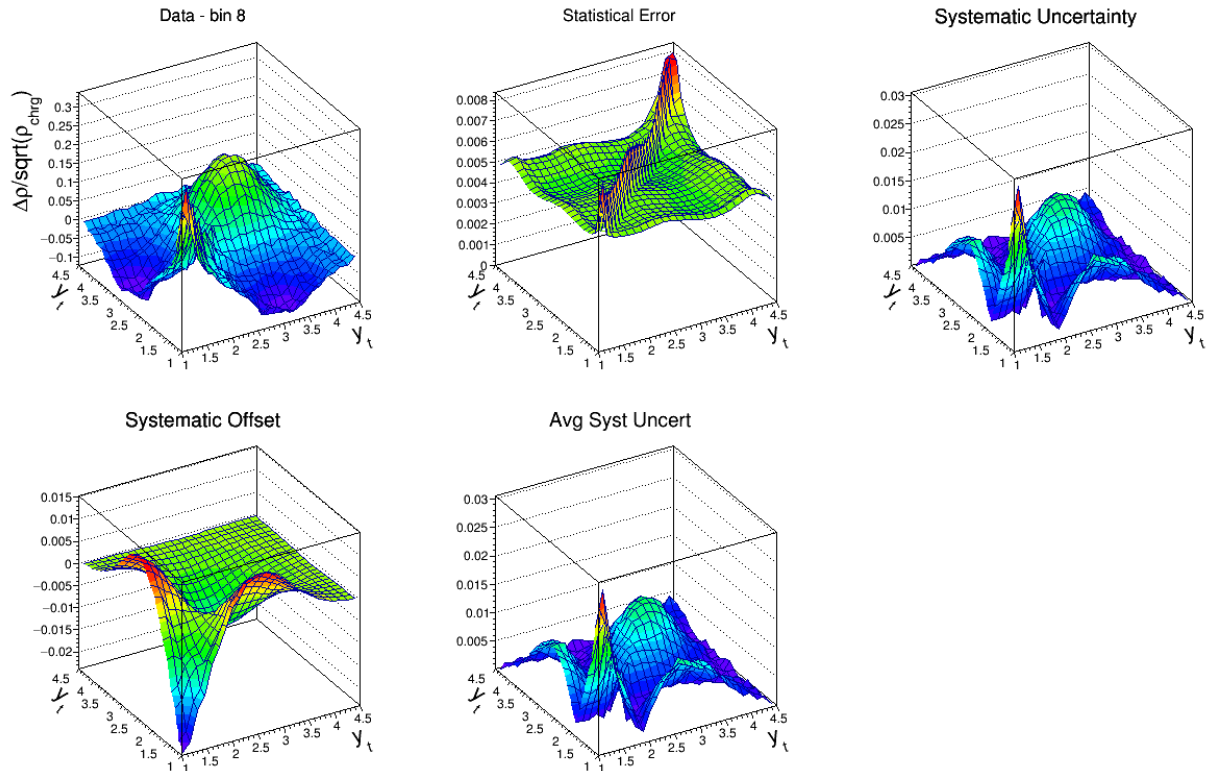


Fig. 9: Same as Fig. 1 except for the 9-18% centrality bin

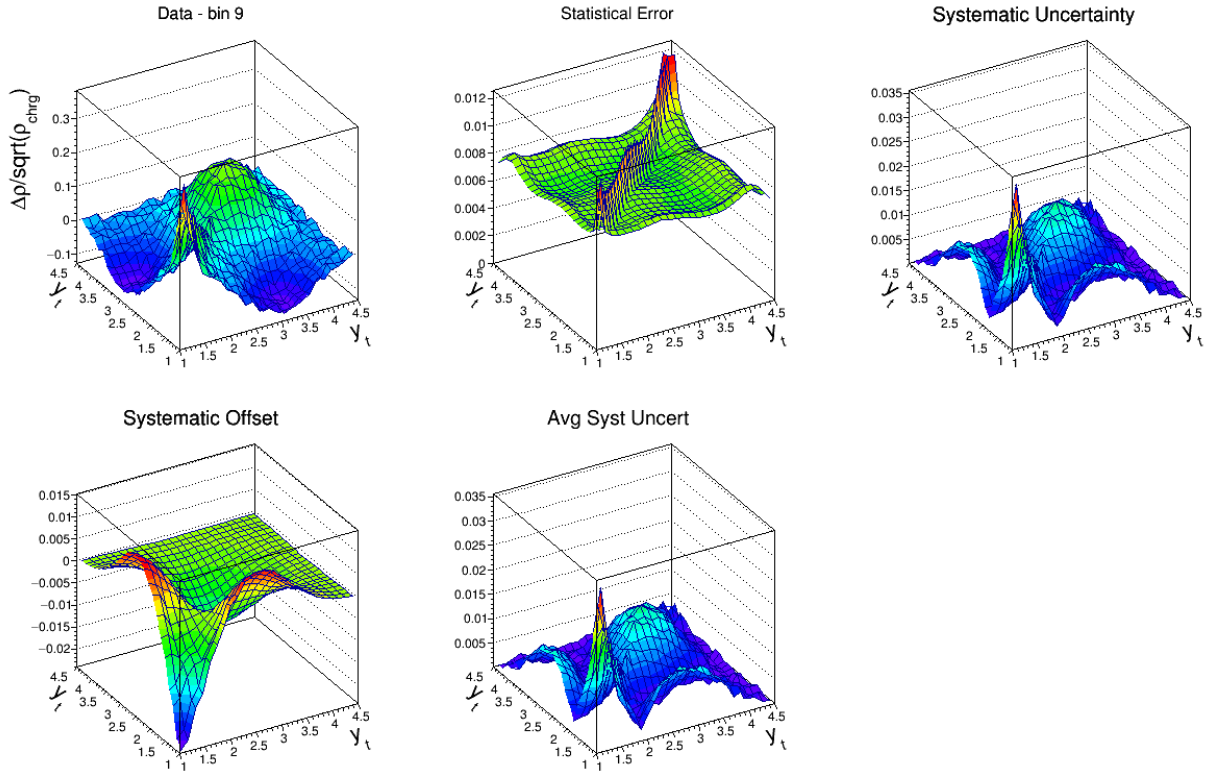


Fig. 10: Same as Fig. 1 except for the 5-9% centrality bin.

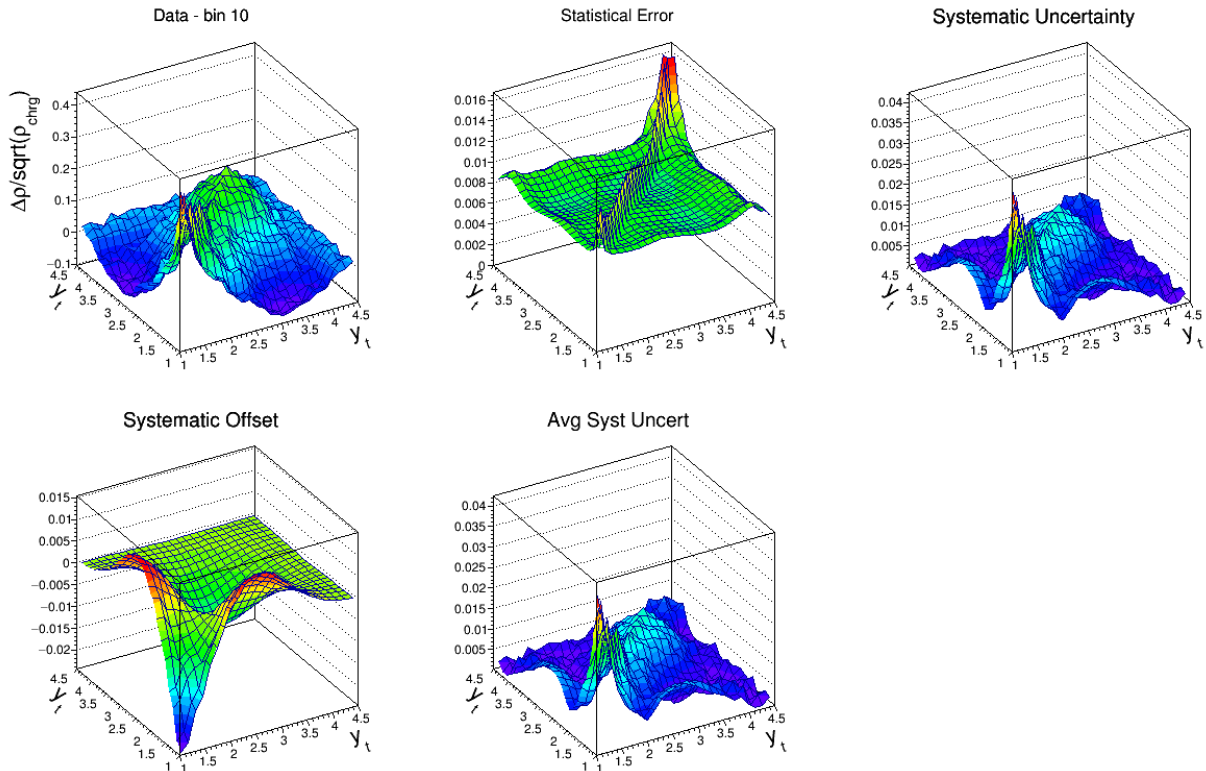


Fig. 11: Same as Fig. 1 except for the 0-5% centrality bin.

K. Plots of individual error sources

The individual contributions to the systematic uncertainties for the CI, all-azimuth correlations are shown in Figs. 12-22 in the following pages. The systematic errors shown in these plots include those for the charged-particle pre-factor. The systematic uncertainties in the charged pre-factor are discussed in Appendix B. Empty plots indicate that the estimated error contribution is negligible.

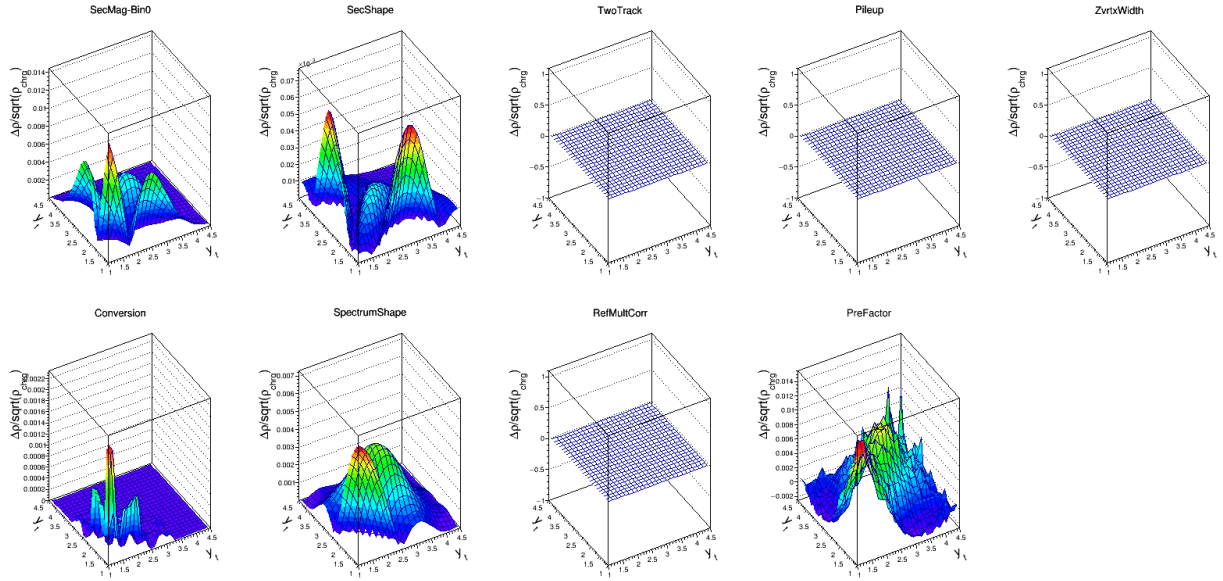


Fig. 12: Contributions to systematic uncertainty in the CI, all-azimuth correlations with charge-particle pre-factor for the 84-93% centrality bin. Panels from left-to-right in the upper and lower rows, respectively, show the contributions from magnitude fluctuations in the secondary particle yield, fluctuating shape of the secondary particle distributions, uncertainties in the two-track inefficiency corrections, uncertainty in the pile-up correction, primary vertex position event-mixing bin widths, conversion electrons, multiplicity dependence in the single-particle p_T distribution, PV position and luminosity dependent efficiencies discussed in Appendix A, and charge-particle pre-factor uncertainties discussed in Appendix B.

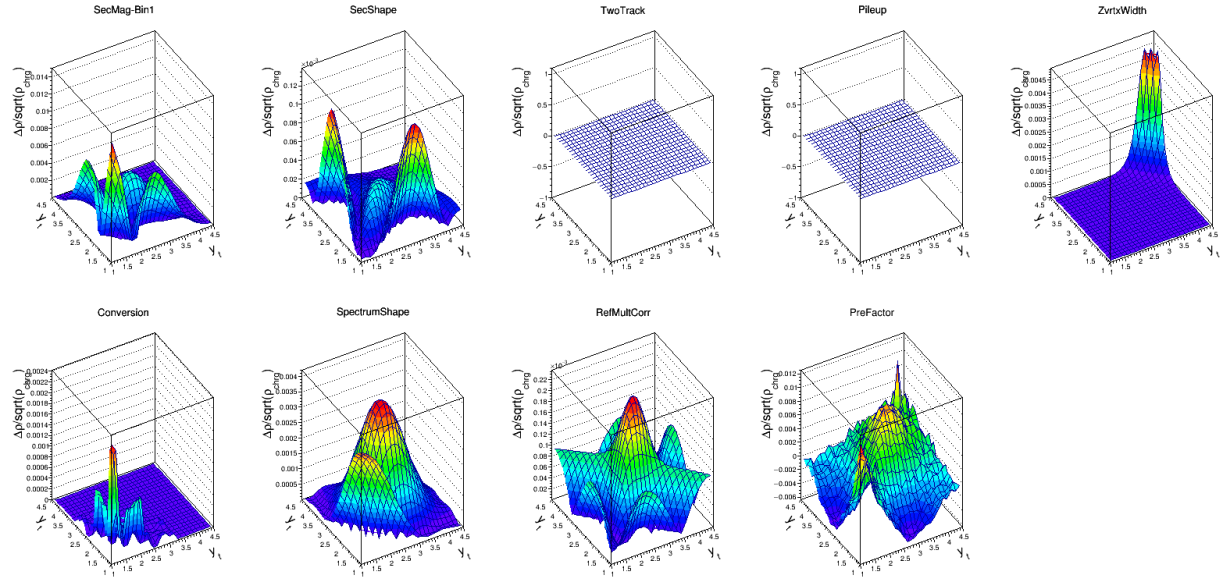


Fig. 13: Same as Fig. 12 except for the 74-84% centrality bin.

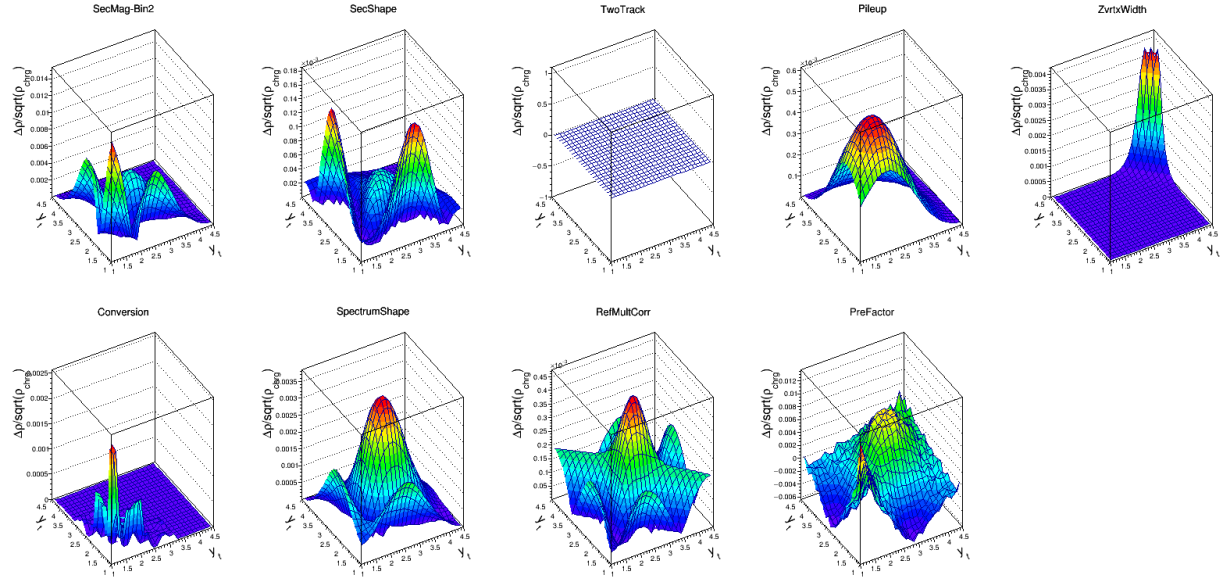


Fig. 14: Same as Fig. 12 except for the 64-74% centrality bin.

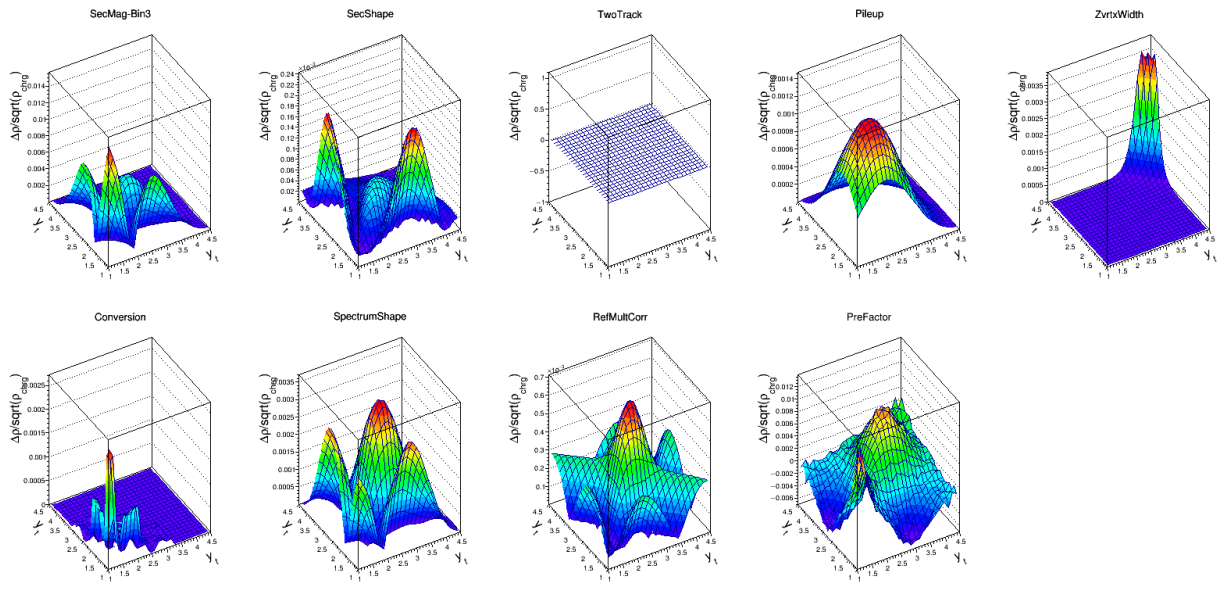


Fig. 15: Same as Fig. 12 except for the 55-64% centrality bin.

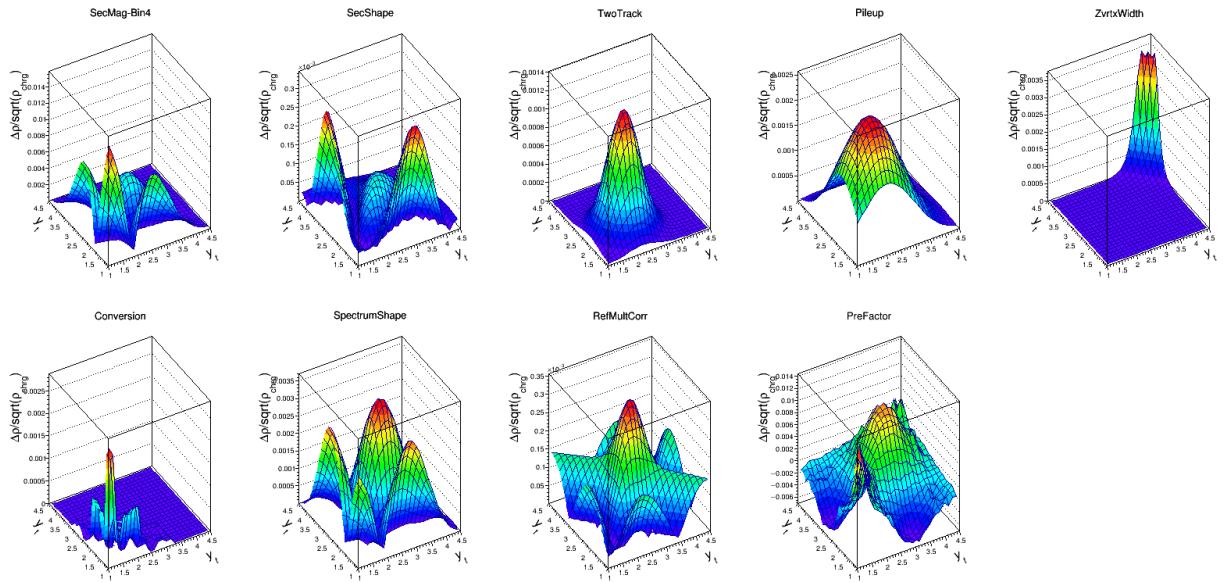


Fig. 16: Same as Fig. 12 except for the 46-55% centrality bin.

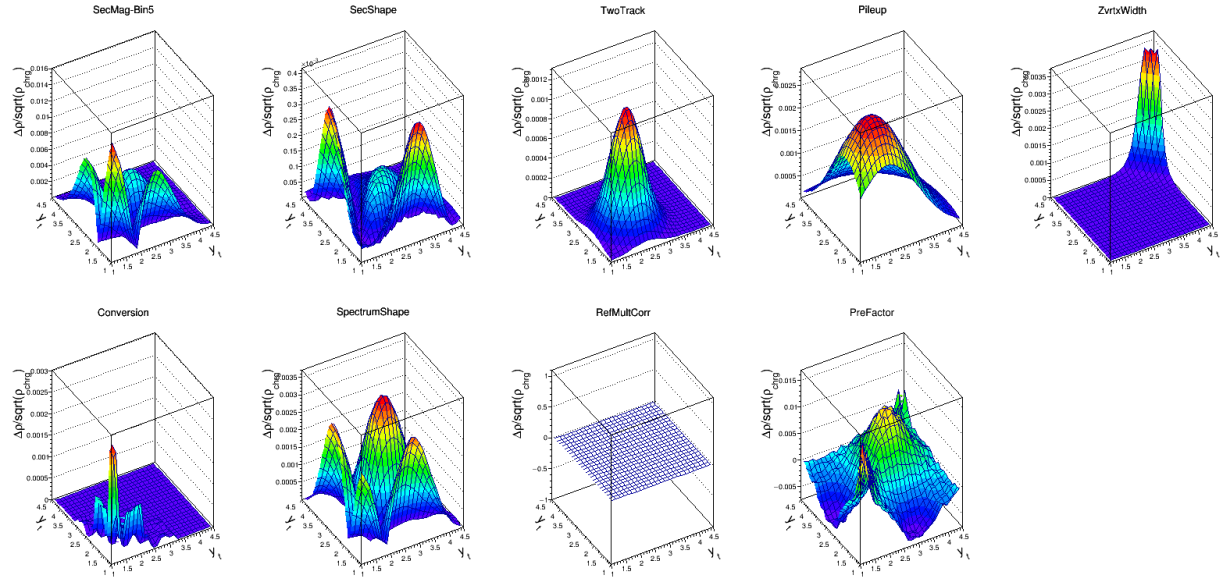


Fig. 17: Same as Fig. 12 except for the 38-46% centrality bin.

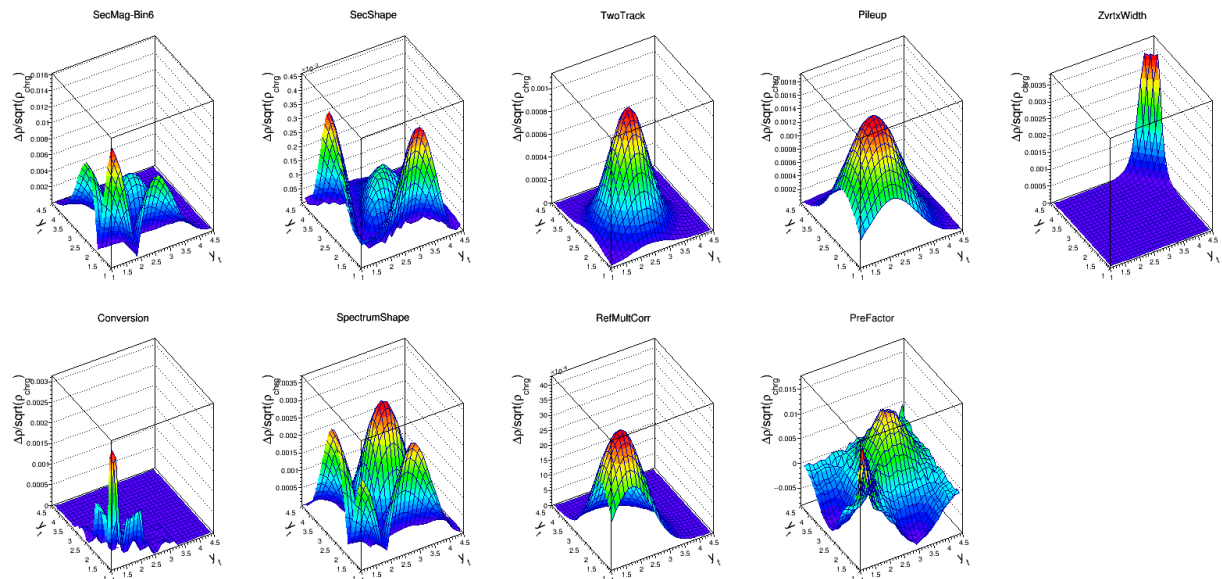


Fig. 18: Same as Fig. 12 except for the 28-38% centrality bin.

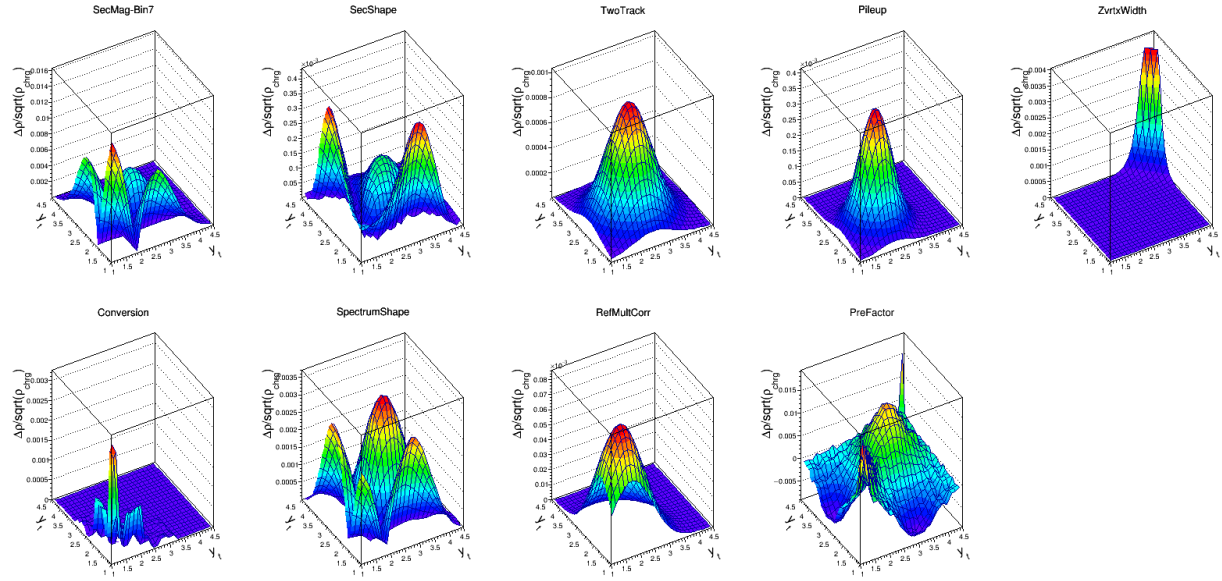


Fig. 19: Same as Fig. 12 except for the 18-28% centrality bin.

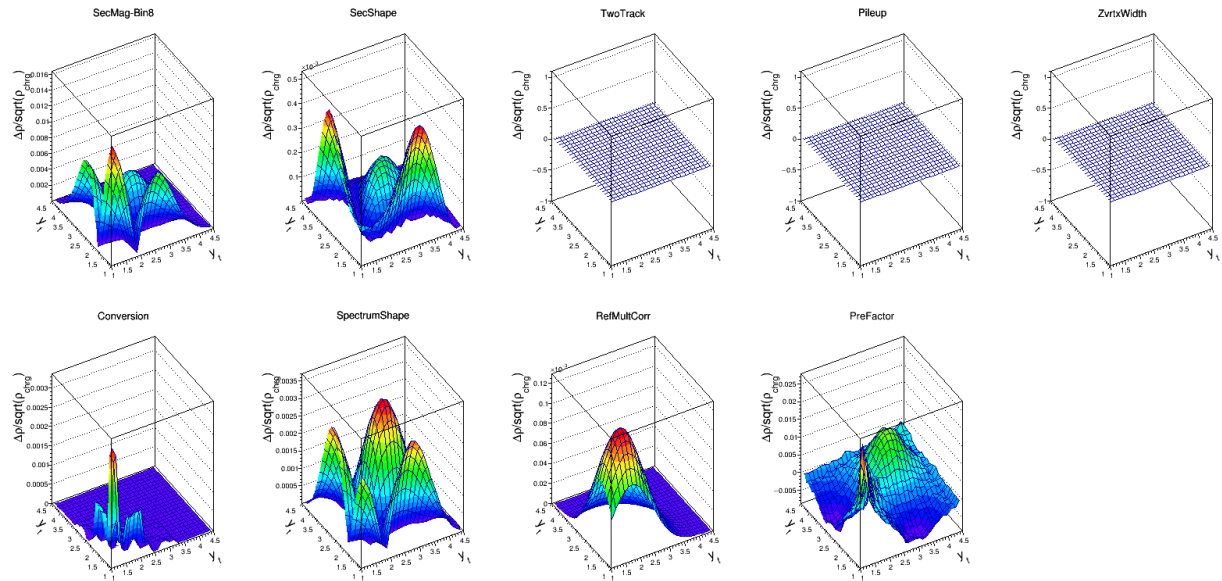


Fig. 20: Same as Fig. 12 except for the 9-18% centrality bin.

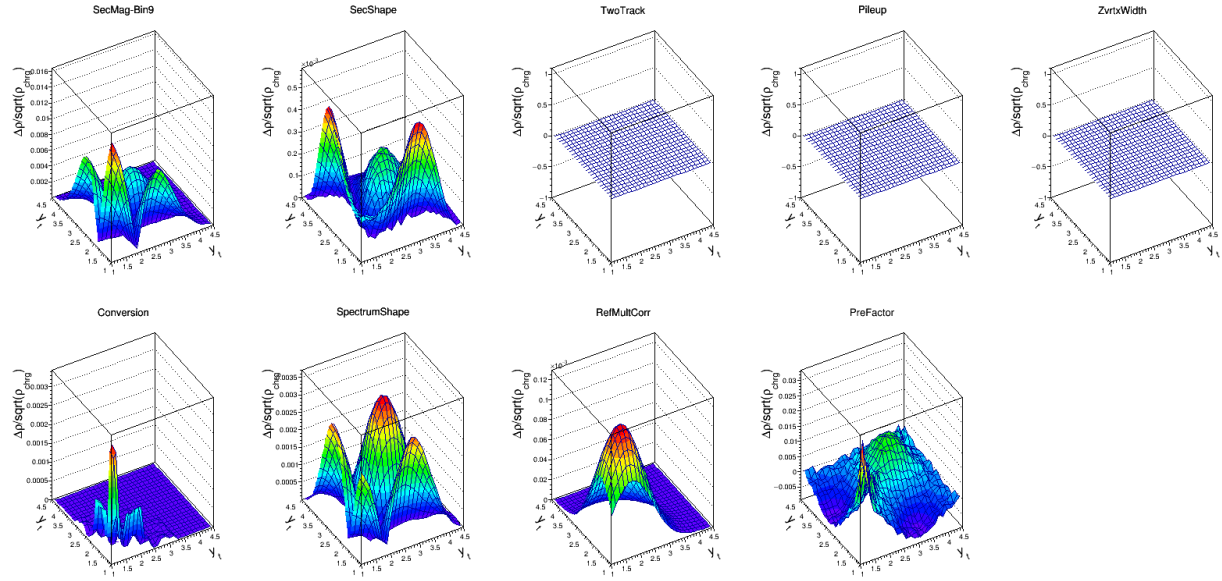


Fig. 21: Same as Fig. 12 except for the 5-9% centrality bin.

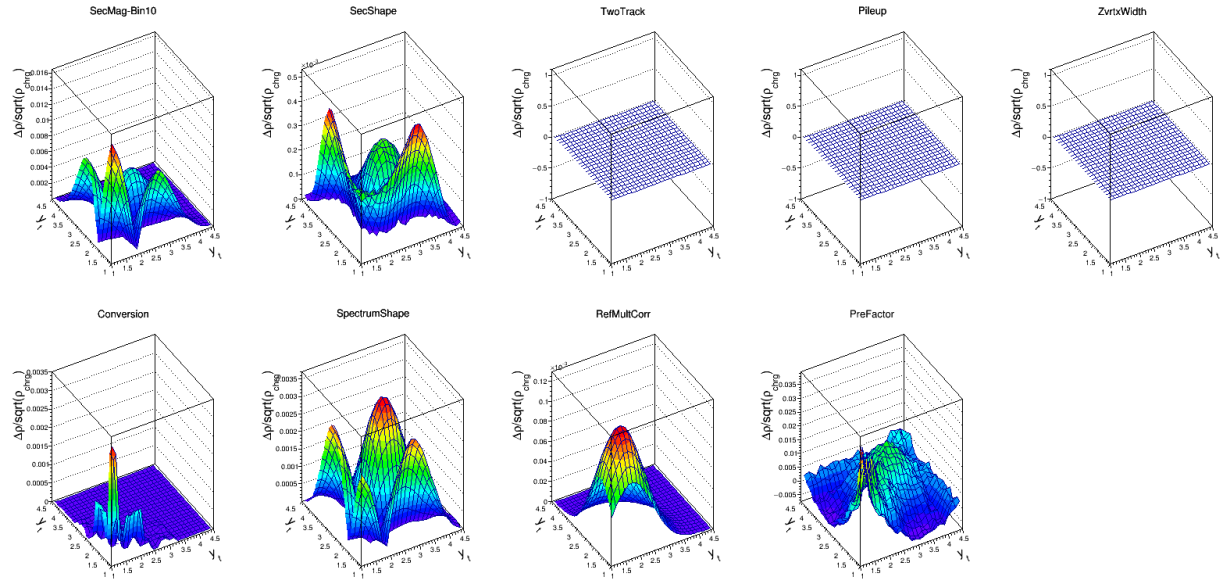


Fig. 22: Same as Fig. 12 except for the 0-5% centrality bin.

IV. Pre-Factor Charge and Azimuth-Dependent Scale Factors

Each systematic uncertainty may depend on the charge-pair combination and the relative, azimuthal angle. For example, the photon conversion contamination only contributes to unlike-sign, near-side correlations while the two-track resolution affects all charge pairs but only on the near-side. In addition, the amplitudes of the pre-factors for the correlation quantities depend on the charge-pair combination and relative azimuth angle. The above discussion applies to the CI, all-azimuth correlations. To convert the above to each of the other charge and azimuth projections we consider how the quantity $\Delta\rho/\sqrt{\rho_{\text{chrg}}}$ changes for LS, US and charge-dependent (CD), and for near-side or away-side azimuthal projections, relative to the CI, all-azimuth case. The pre-factor scaling factors are listed in the following table.

Pre-factor scaling			
Charge	All ϕ	Near-side	Away-side
CI	1.0	$1/\sqrt{2}$	$1/\sqrt{2}$
CD	$1/\sqrt{2}$	$1/\sqrt{2}$	$1/\sqrt{2}$
LS	$1/\sqrt{2}$	$1/2$	$1/2$
US	$1/\sqrt{2}$	$1/2$	$1/2$

Table II: Pre-factor scales for NS, AS, LS and US combinations relative to the CI, all azimuth.

The six, systematic uncertainty sources, (1 & 2) secondary contamination magnitude and shape, (3) pileup, (4) z-vertex binning, (5) p_t slope dependence on N_{ch} , and (6) RefMultCorr-type, have the same scale-factors for a specific charge-pair, azimuthal projection. These scale factors are listed in the following table. The scale factors for two-track resolution and conversion electron contamination are also listed in the following table. In most cases the scale factors are the same for the offset and uncertainty, but are listed separately. The systematic uncertainties for the pre-factors in Appendix B are given as a relative fraction (percent) at each (y_t, p_t) bin. Those estimates therefore apply the same percentage error to each charge and/or azimuthal projection.

Scale factors for $\Delta\rho / \sqrt{\rho_{chrg}}$ relative to all - azimuth, CI						
Case	Offset			Uncertainty		
	(1)-(6)	2-track	e+e-	(1)-(6)	2-track	e+e-
CI-all	1	1	1	1	1	1
CD-all	0	0	-1	1	1	1
LS-all	$1/\sqrt{2}$	$1/\sqrt{2}$	0	$1/\sqrt{2}$	$1/\sqrt{2}$	0
US-all	$1/\sqrt{2}$	$1/\sqrt{2}$	$\sqrt{2}$	$1/\sqrt{2}$	$1/\sqrt{2}$	$\sqrt{2}$
CI-NS	$1/\sqrt{2}$	$\sqrt{2}$	$\sqrt{2}$	$1/\sqrt{2}$	$\sqrt{2}$	$\sqrt{2}$
CD-NS	0	0	$-\sqrt{2}$	$1/\sqrt{2}$	$\sqrt{2}$	$\sqrt{2}$
LS-NS	$1/2$	1	0	$1/2$	1	0
US-NS	$1/2$	1	2	$1/2$	1	2
CI-AS	$1/\sqrt{2}$	0	0	$1/\sqrt{2}$	0	0
CD-AS	0	0	0	$1/\sqrt{2}$	0	0
LS-AS	$1/2$	0	0	$1/2$	0	0
US-AS	$1/2$	0	0	$1/2$	0	0

Table III: Scale factors for all systematic error sources (except those for the pre-factor) for systematic offsets and uncertainties, for the NS, AS, LS and US combinations relative to the corresponding offsets and errors for the all-azimuth, CI projection.

Finally, systematic uncertainties in the BW and TCF phenomenological model parameters were estimated by fitting the CI, all-azimuth nominal correlation data, the nominal data increased by the total systematic uncertainty, and the nominal data decreased by the total systematic uncertainty. The asymmetric errors are shown in Table III in the paper draft for the BW fits. For the TCF model stable fits were only obtained for the nominal data and the data – systematic uncertainty, resulting in the assumed, symmetric systematic uncertainties listed in Table IV of the paper.

V. Resonance Contributions

The contribution of resonance decays (mainly ρ, ω) to the unlike-sign correlations were estimated using a Monte Carlo simulation. The yields and p_t spectra distributions were taken from the $\pi^+\pi^-$ invariant mass yield measurements from STAR [Adams, et al. Phys. Rev. Lett. **92**, 092301 (2004)] for ρ decays, and from PHENIX [Adare et al. Phys. Rev. C **84**, 044902 (2011)] for ω

decays to π^+, π^-, π^0 (BR = 90%). The unit normalized distribution of $\pi^+\pi^-$ pairs from ρ and ω decays and the resulting contributions to the All-CI (y_t, y_{t2}) correlations with charge-particle pre-factor are shown in Fig. 23. The correlation contributions are of order 0.01 which are much smaller than the full, observed correlations.

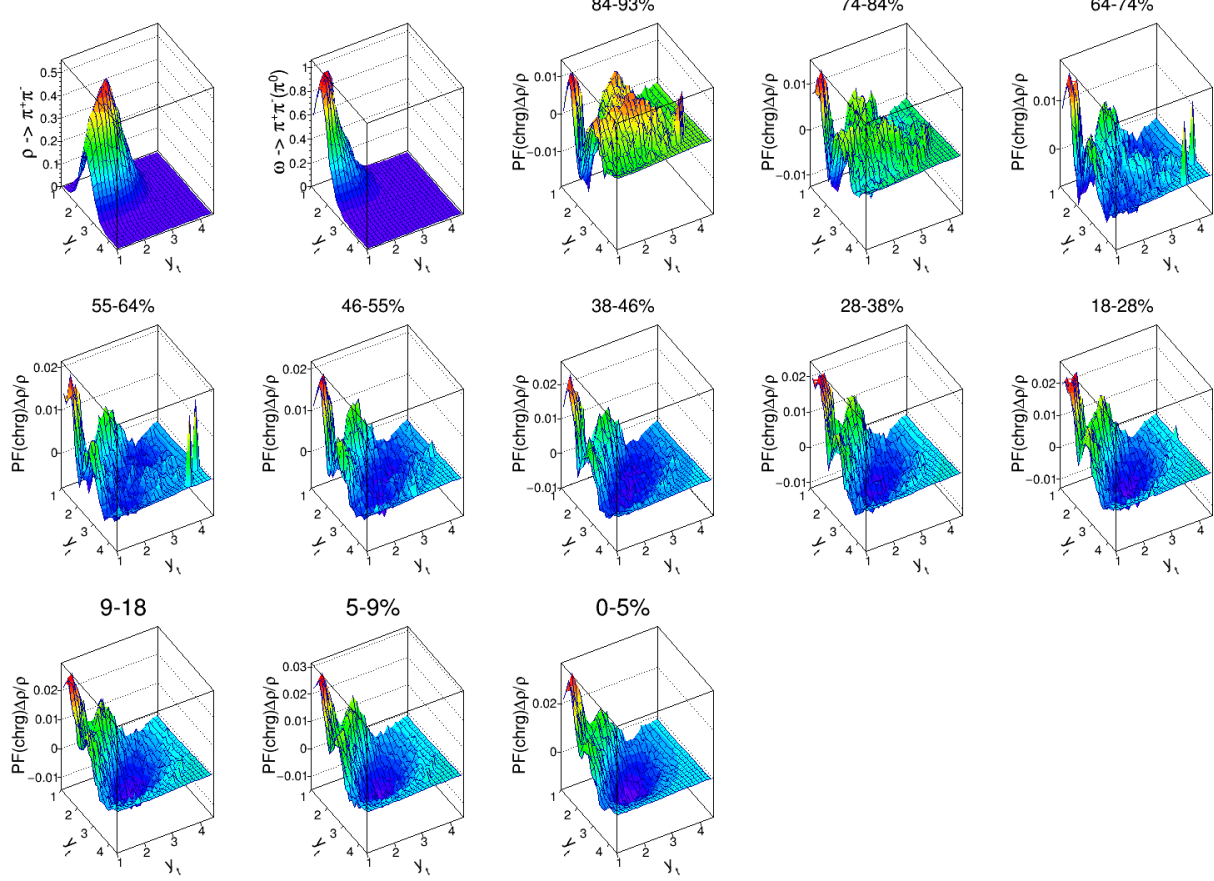


Fig 23: Charged pion pair distributions and correlation contributions from ρ, ω decays to $\pi^+\pi^-$. The first two panels in the upper row show the unit normalized distributions on (y_t, y_{t2}) for ρ and ω decay, respectively. The remaining panels show the contribution of the $\pi^+\pi^-$ decay daughters to the All-CI (y_t, y_{t2}) correlations for all eleven centralties as labelled. The charge-particle pre-factor was used.

VI. Additional Analysis

To better compare the all, CI correlation data with the predictions of HIJING and EPOS the amplitudes and positions of the peaks near $(y_t, y_{t2}) = (3, 3)$ and the minima in the saddle-shape near $(y_t, y_{t2}) = (3, 1)$ were extracted and compared for both the data and theoretical models. The amplitudes and positions were estimated by fitting the extrema in the data including two bins on either side of the bin containing the maximum or minimum. In a few cases the fitting ranges were reduced to allow more stable fits. The data near the extrema were fit with a two models: a two-dimensional, second-order polynomial and a 2D Gaussian. For maxima, located along the $y_{t1} = y_{t2}$ diagonal, the 2D functions were oriented along the sum ($y_{t1} + y_{t2}$) and difference ($y_{t1} - y_{t2}$) directions; for minima the orientation was along y_{t1} and y_{t2} . The fitted amplitudes, width

parameters and positions were extracted by chi-square minimization and the statistical fitting errors were extracted by standard covariance matrix inversion. Systematic uncertainties in the fits to the data were included using those variations in fit parameters resulting from including the bin-wise systematic error increases/decreases in the data, plus the model dependence difference from the polynomial versus Gaussian fits. The width parameters are the least well determined and depend on the fitting range. The fitting models are only intended to capture the amplitude and peak/mimima positions, not the widths of the correlations structures. Therefore, only the amplitudes and positions are plotted and compared. The results are shown in new figures 6 and 7 in the paper.

VII. Figures for the paper

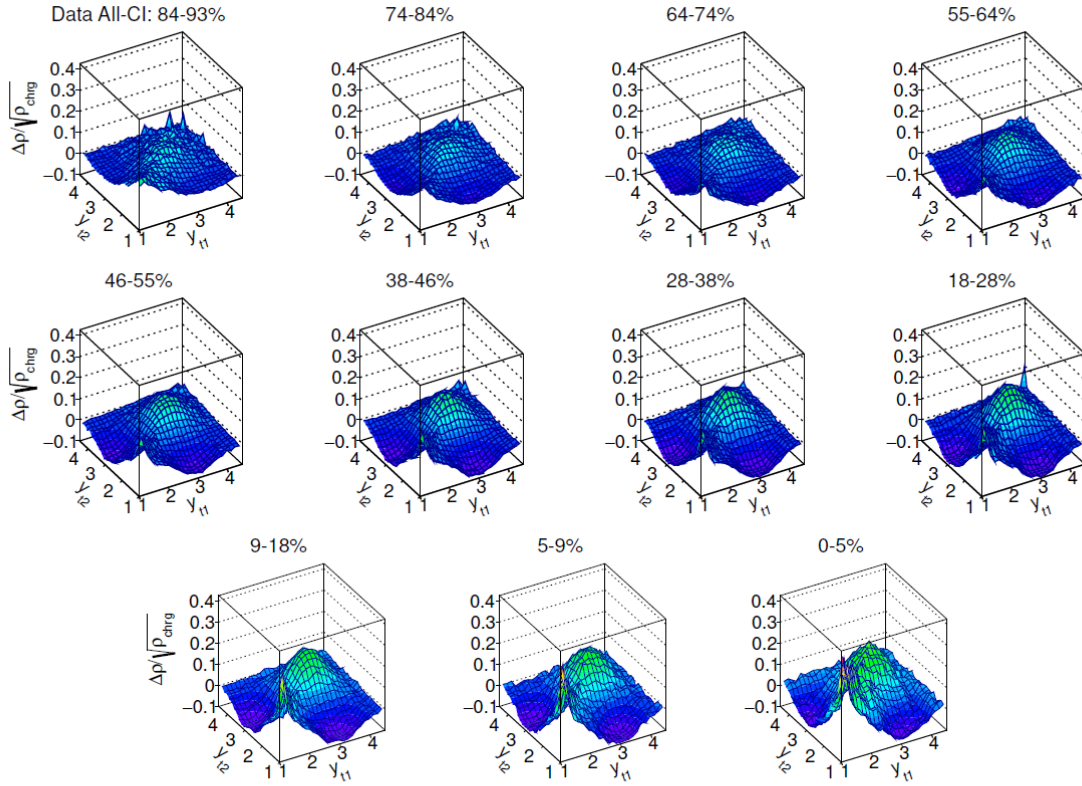


FIG. 1: Perspective views of two-dimensional correlations $\Delta\rho/\sqrt{\rho_{\text{chrg}}}$ on coordinates (y_{T1}, y_{T2}) for minimum-bias Au+Au collisions at $\sqrt{s_{\text{NN}}} = 200$ GeV using all charged particle pairs and including all relative azimuthal angles $\Delta\phi$ from $-\pi$ to π , as discussed in the text. Centrality ranges are indicated for each panel in percent of total reaction cross section.

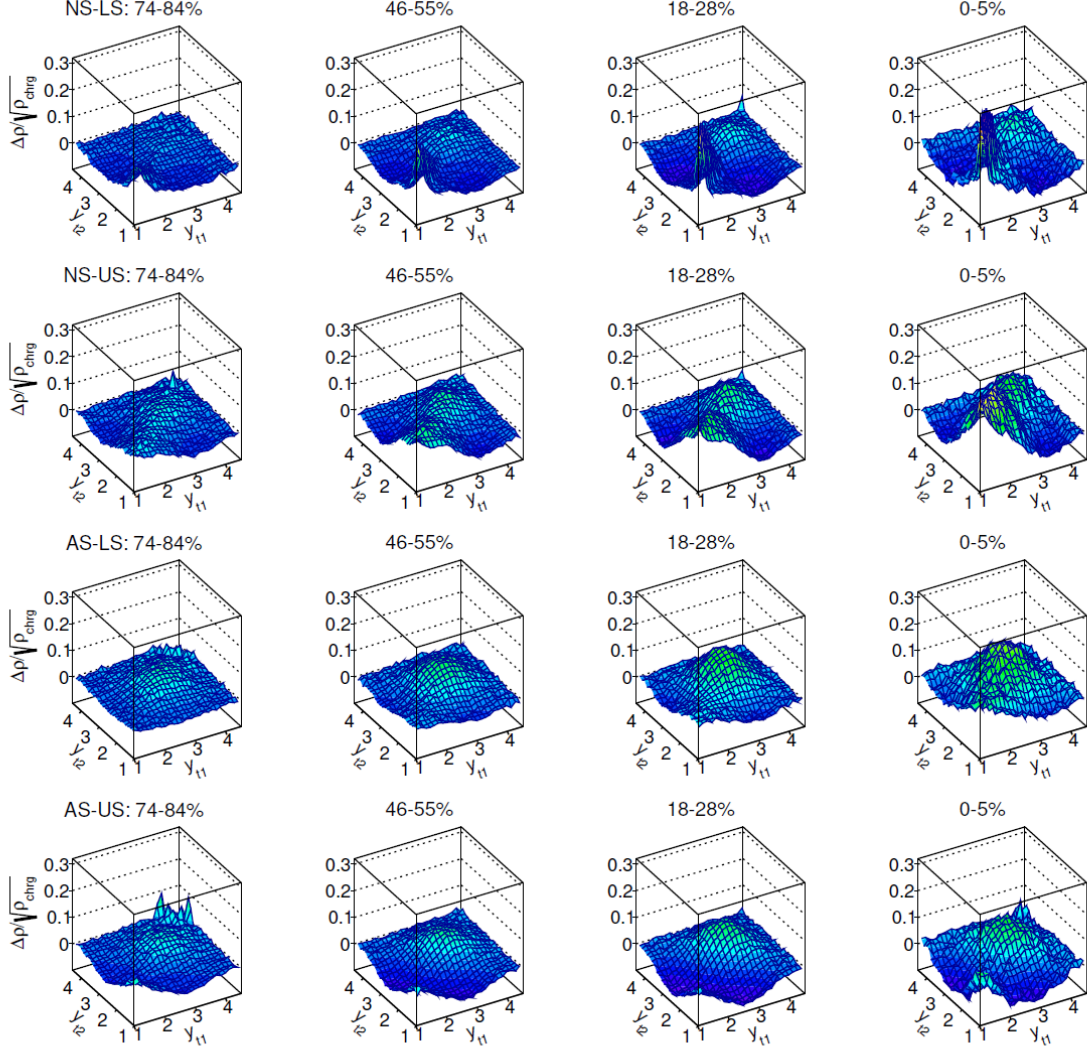


FIG. 2: Perspective views of two-dimensional correlations $\Delta\rho/\sqrt{\rho_{\text{chrg}}}$ on coordinates (y_{T1}, y_{T2}) for Au+Au collisions at $\sqrt{s_{\text{NN}}} = 200$ GeV as discussed in the text. The first two rows correspond to charged particle pairs with relative azimuth $|\Delta\phi| \leq \pi/2$ (near-side). The bottom two rows correspond to charged particle pairs with relative azimuth $\pi \geq |\Delta\phi| > \pi/2$ (away-side). The first and third rows are for like-sign pairs and the second and fourth rows are for unlike-sign pairs. Centrality increases in each row of panels from left-to-right from most-peripheral to most-central corresponding to total cross-section fractions 74-84%, 46-55%, 18-28%, and 0-5%, respectively.

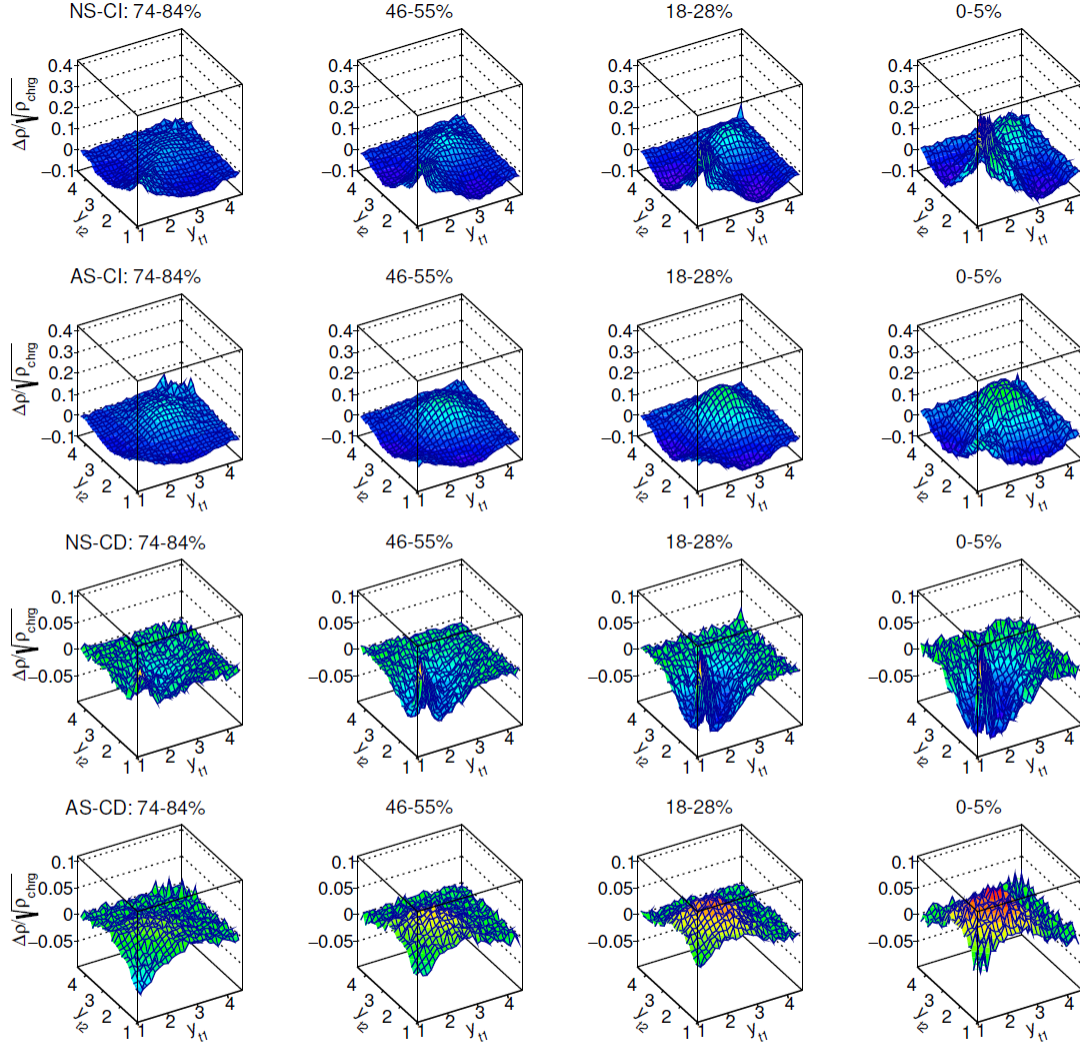


FIG. 3: Same as Fig. 2 except for the sum (CI) (upper two rows) and differences (lower two rows) between like-sign and unlike-sign charged-pairs (CD) for relative azimuth on the near-side (first and third rows) and away-side (second and fourth rows) as discussed in the text. Centrality increases in each row of panels from left-to-right for total cross-section fractions 74-84%, 46-55%, 18-28%, and 0-5%, respectively.

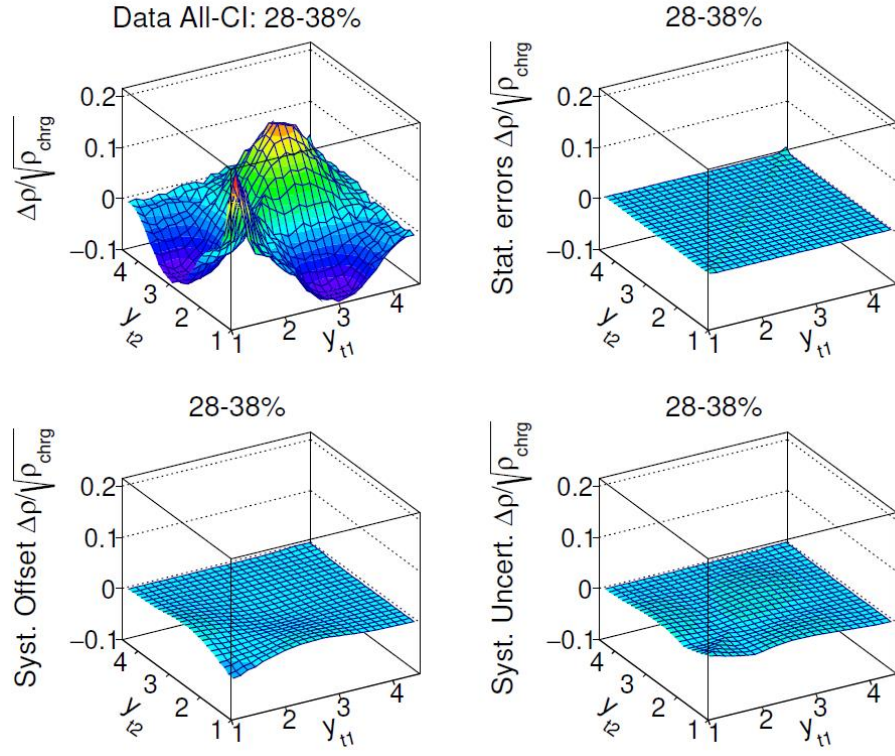


FIG. 4: Statistical errors, systematic offsets, and systematic uncertainties in comparison with the data for each 2D (y_{T1}, y_{T2}) bin for the CI, all-azimuth correlations for the 28-38% centrality bin. A common scale is used to emphasize the relative magnitudes of the correlations and the errors.

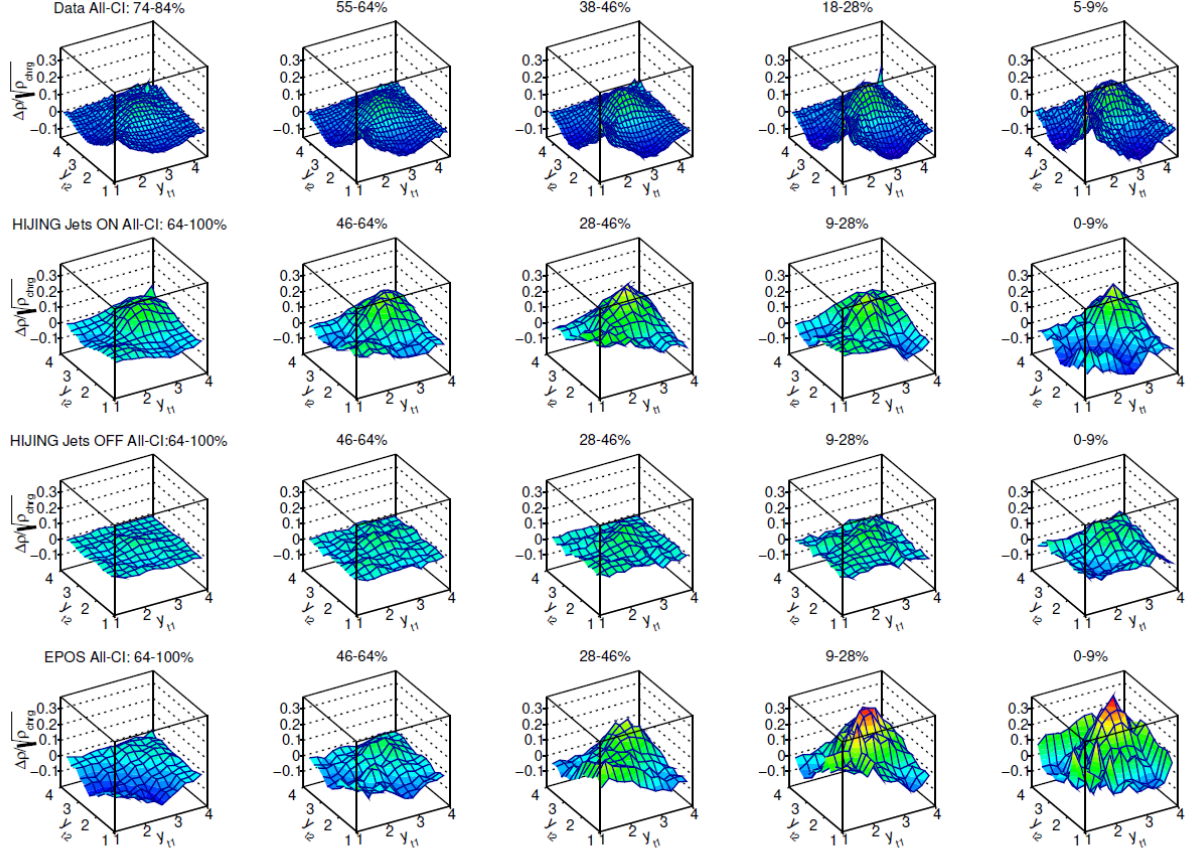


FIG. 5: Comparisons between theoretical model predictions and measured two-dimensional correlations $\Delta\rho/\sqrt{\rho_{\text{chrg}}}$ on coordinates (y_{T1}, y_{T2}) for Au+Au collisions at $\sqrt{s_{\text{NN}}} = 200$ GeV for all charged particle pairs and all relative azimuthal angles. Data are shown in the upper row of panels for centrality cross section fractions 74-84%, 55-64%, 38-46%, 18-28% and 5-9% from left-to-right, respectively. The next three rows show, respectively, HIJING model predictions for 200 GeV Au+Au collisions with jets-on, HIJING with jets-off, and EPOS predictions. Centralities for the HIJING and EPOS predictions are shown in each row from left-to-right for the broader cross section fractions 64-100%, 46-64%, 28-46%, 9-28% and 0-9%, respectively, as required by the available statistics in these simulations.

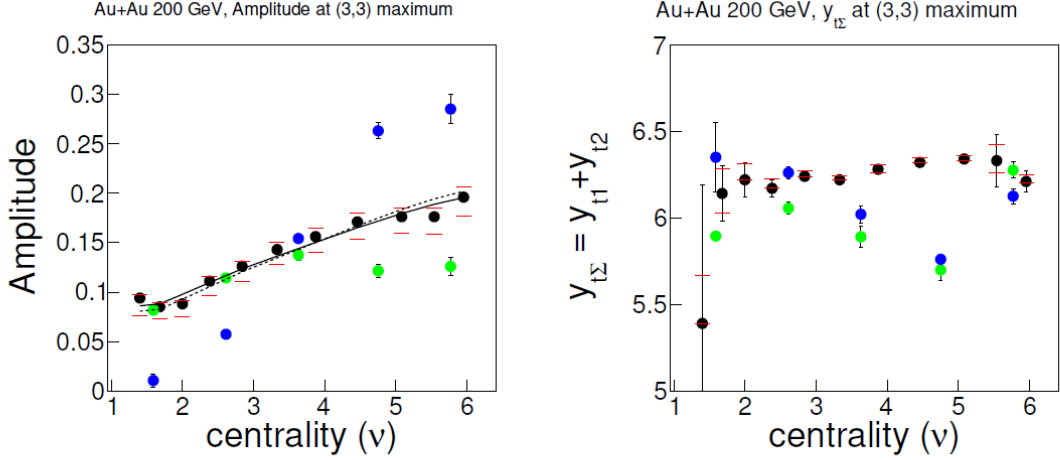


FIG. 6: Fit results for the amplitudes and positions of the measured and predicted correlation peak near $(y_{t1}, y_{t2}) = (3,3)$ as a function of centrality. Centrality is denoted by parameter v described in the text and increases from peripheral to most-central from left to right. Black, green and blue data points indicate results for data, HIJING jets-on and EPOS, respectively. Statistical errors are indicated by black error bars while systematic uncertainties are shown as red cross-bars for the data results. A binary scaling function fit (see text) to the measured correlation peak amplitudes is shown by the solid black curve. The fit requiring exact binary scaling ($\gamma = 1$) is shown by the dotted black curve.

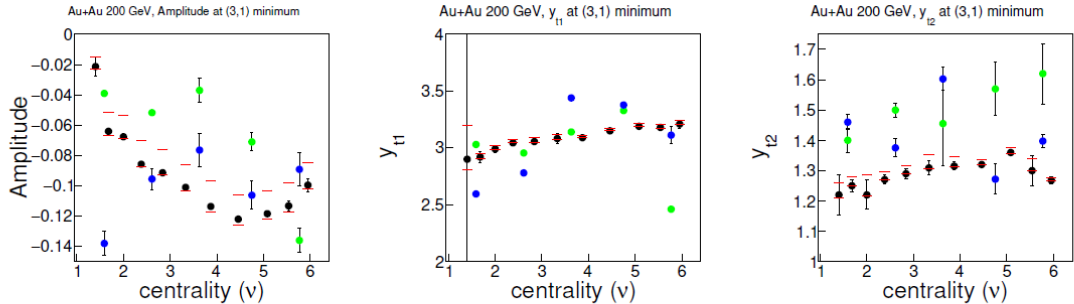


FIG. 7: Same as Fig. 6 except for the amplitudes and 2D positions of the saddle-shape minima.

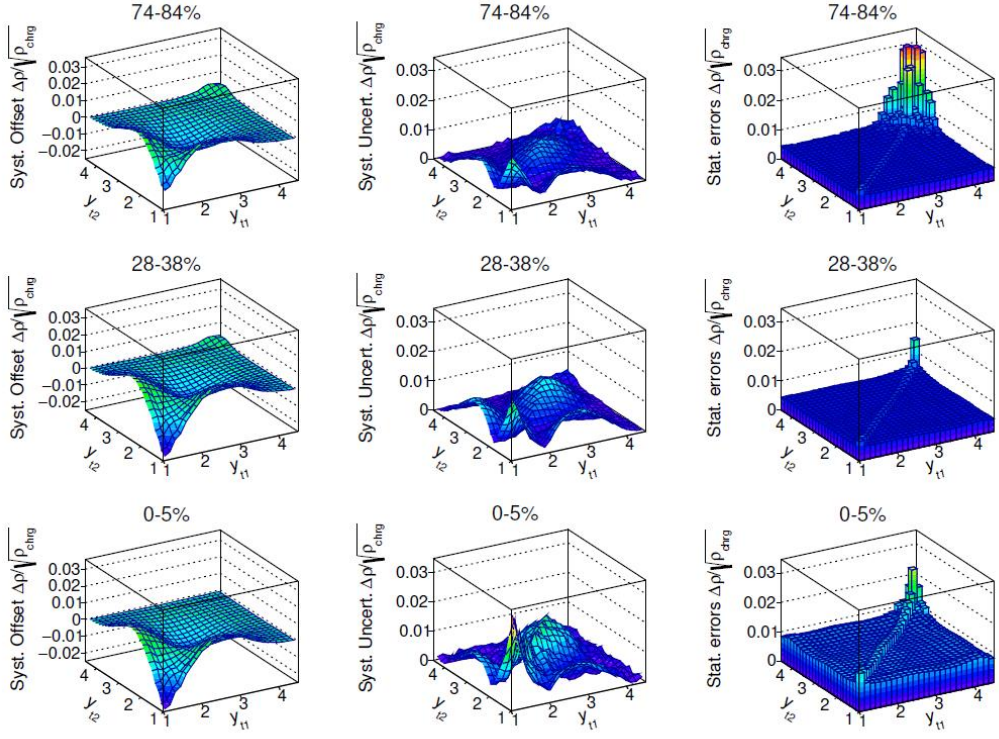


FIG. 8: Systematic offsets, systematic uncertainties and statistical errors in the CI, all-azimuth correlations in columns of panels from left-to-right, respectively. Representative results for centralities 74-84%, 28-38% and 0-5% are shown in rows of panels from upper to lower, respectively.

References

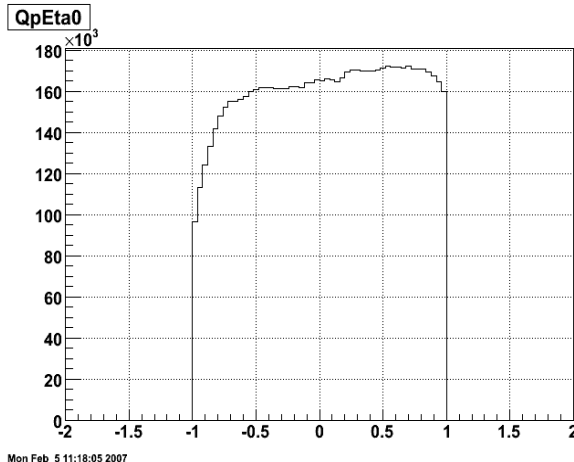
1. R. L. Ray and P. Bhattacharai, Phys. Rev. C **94**, 064902 (2016).
2. R. L. Ray and P. Bhattacharai, Nucl. Instrum. Meth. Phys. Res. A **821**, 142 (2016).
3. G. Agakishiev et al. (STAR Collaboration), Phys. Rev. C **86**, 064902 (2012).
4. Michael Daugherty Ph.D. Thesis, The University of Texas at Austin (2008);
https://drupal.star.bnl.gov/STAR/files/daugherty_dissertation.pdf
5.
https://www.star.bnl.gov/protected/jetcorr/eststruct/ray/papers/Liz_AuAu200Run4_ytyt/cent.html
6. Elizabeth Oldag Ph.D. Thesis, The University of Texas at Austin (2013);
https://drupal.star.bnl.gov/STAR/files/oldag_dissertation_20132.pdf
7. Michael Daugherty centrality analysis:
<https://www.star.bnl.gov/protected/jetcorr/eststruct/msd/data/200/centrality/index.html>
8. R. L. Ray and M. S. Daugherty, J. Phys. G: Nucl. Part. Phys. **35**, 125106 (2008).
9. Elizabeth Oldag systematic error study;
<http://www.rhip.utexas.edu/public/eoldag/private/AuAu200/YtYt/paperFigures.html>
10. B. I. Abelev et al. (STAR Collaboration), Phys. Rev. C **79**, 034909 (2009).
11. J. Adams et al. (STAR Collaboration), J. Phys. G: Nucl. Part. Phys. **34**, 799 (2007).
12. R. L. Ray and A. Jentsch, Phys. Rev. C **99**, 024911 (2019).
13. Particle Data Group, J. Phys. G: Nucl. Part. Phys. **33**, 1 (2006).
14. L. Ray presentation at STAR Collaboration Meeting, May 15-19, 2017, BNL, slides are at
[STAR_BNL_May_2017_ytyt.ppt](https://star.bnl.gov/meetings/2017/STAR_BNL_May_2017_ytyt.ppt)

Appendix A

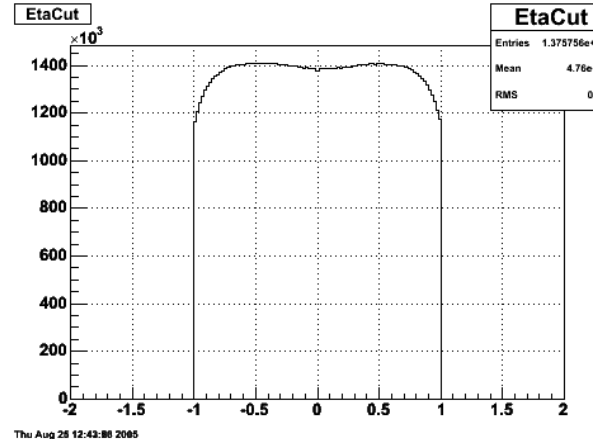
Z-vertex and ZDC-rate Uncertainties

Run 4, Au+Au minbias, no pileup protection

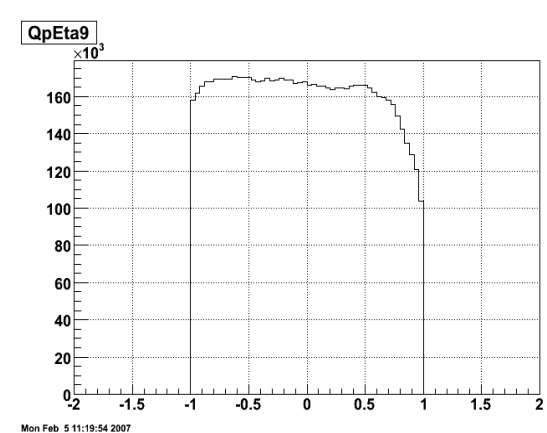
Tracking efficiency dependence on z-vertex position studied in M.
Daugherity's thesis:



Z-vertex = [-25, -20]cm



Z-vertex \sim 0 cm



Z-vertex = [20,25]cm

Relative tracking efficiency dependence on Z-vertex position

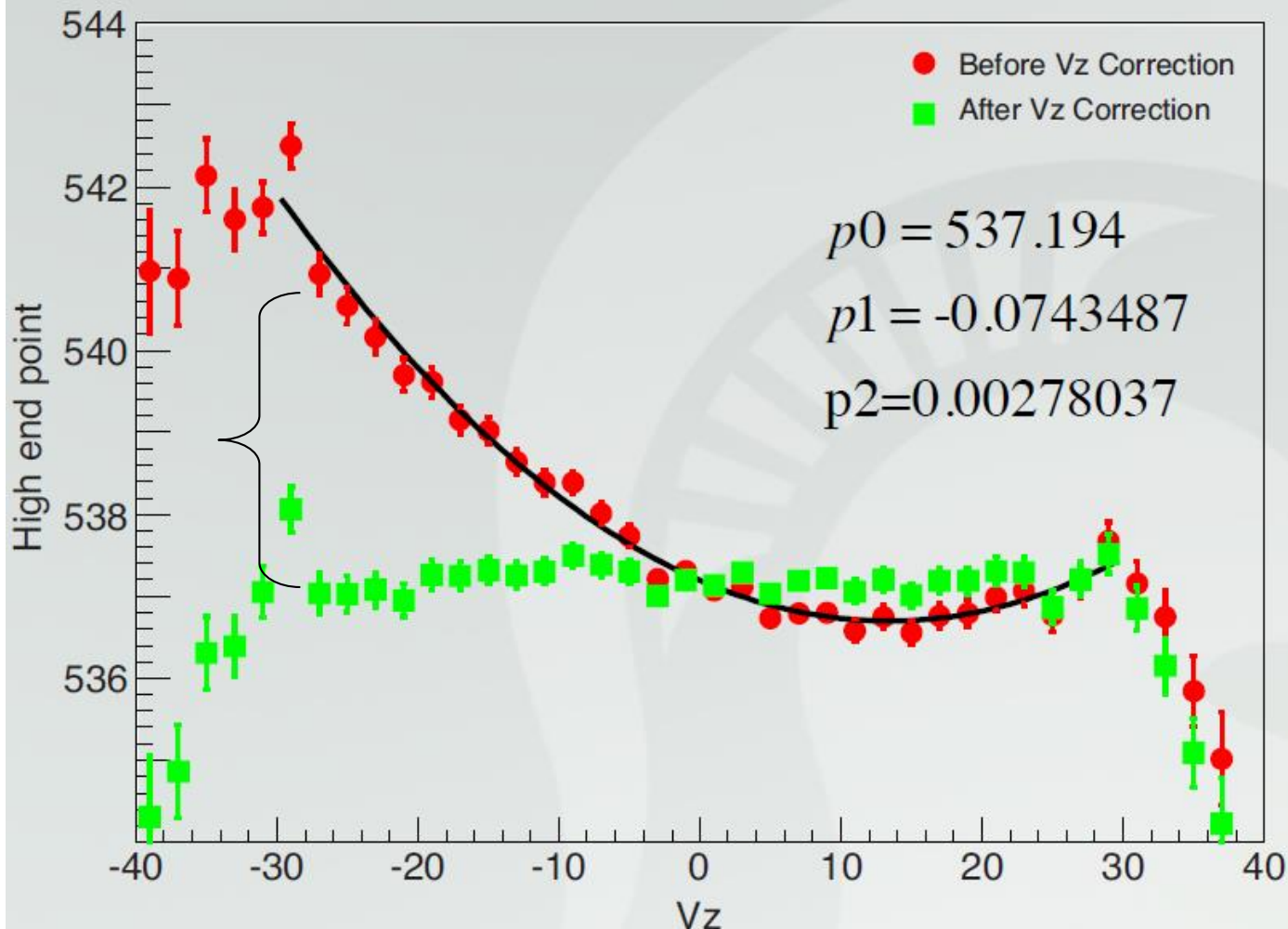
$$\text{RelEff} = 1.0 - 0.0000724z^2, z \text{ in cm}$$

At 25 cm this gives a reduction in efficiency of about 4.5% for
2 units in η ; larger than that found by Hui Wang and Hiroshi Masui's
analysis of Run 11 minbias data (about 1% for refmult)

Z-vertex and ZDC-rate Uncertainties

Vz dependence - period 5

About a 1% effect



- Fit to $f(x) = p_0 + p_1 \cdot x + p_2 \cdot x^2$

Z-vertex and ZDC-rate Uncertainties

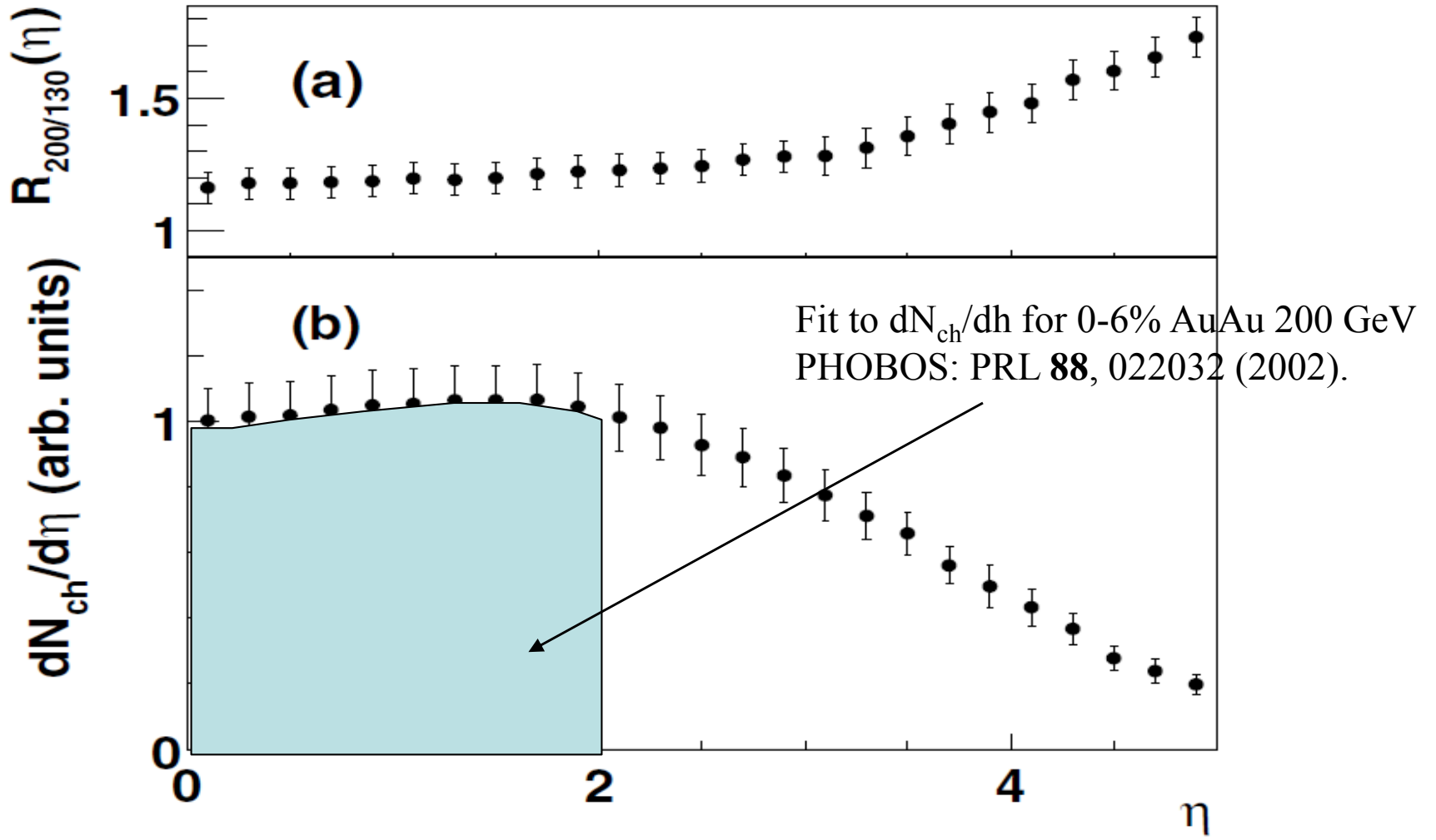
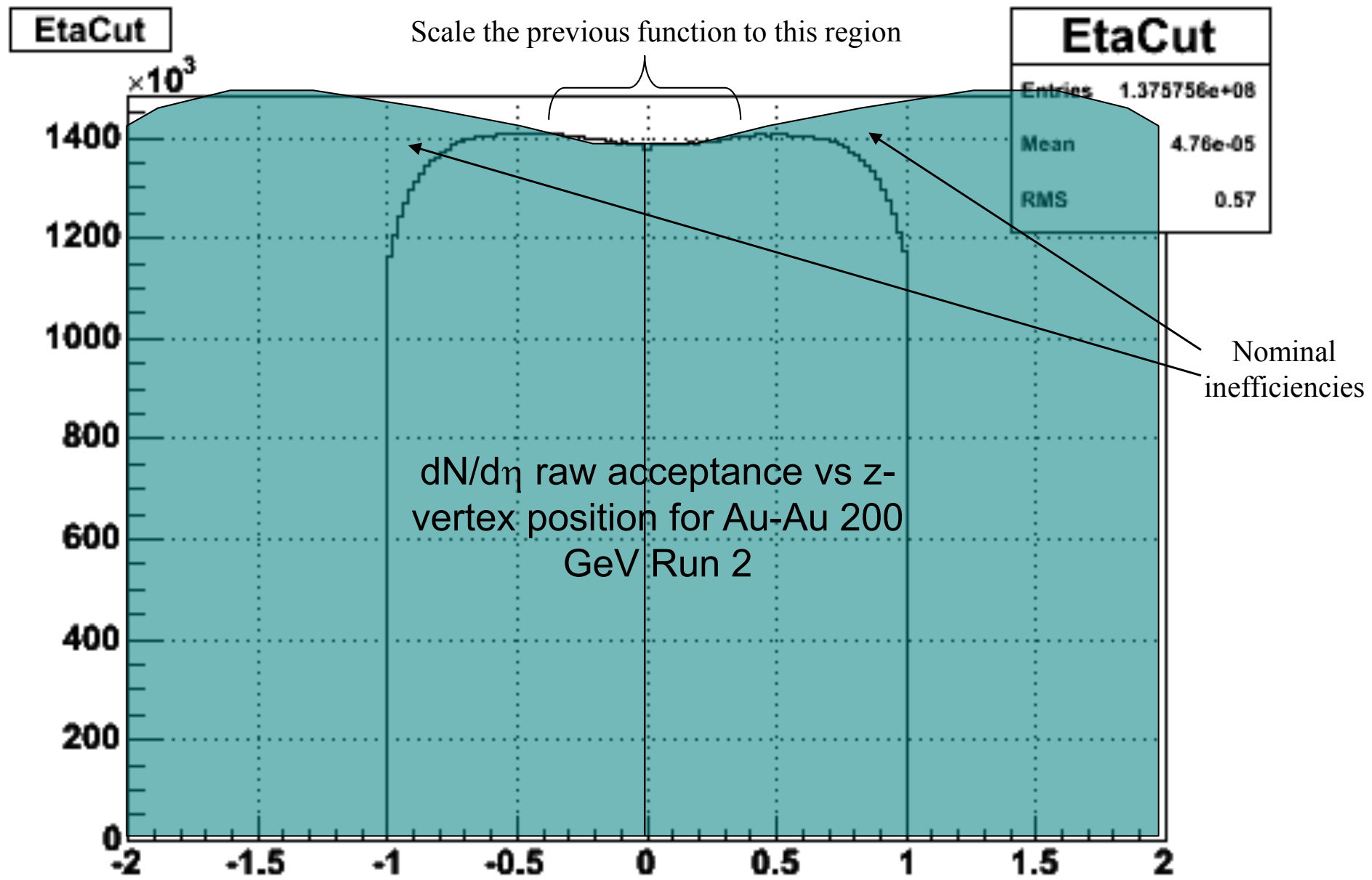
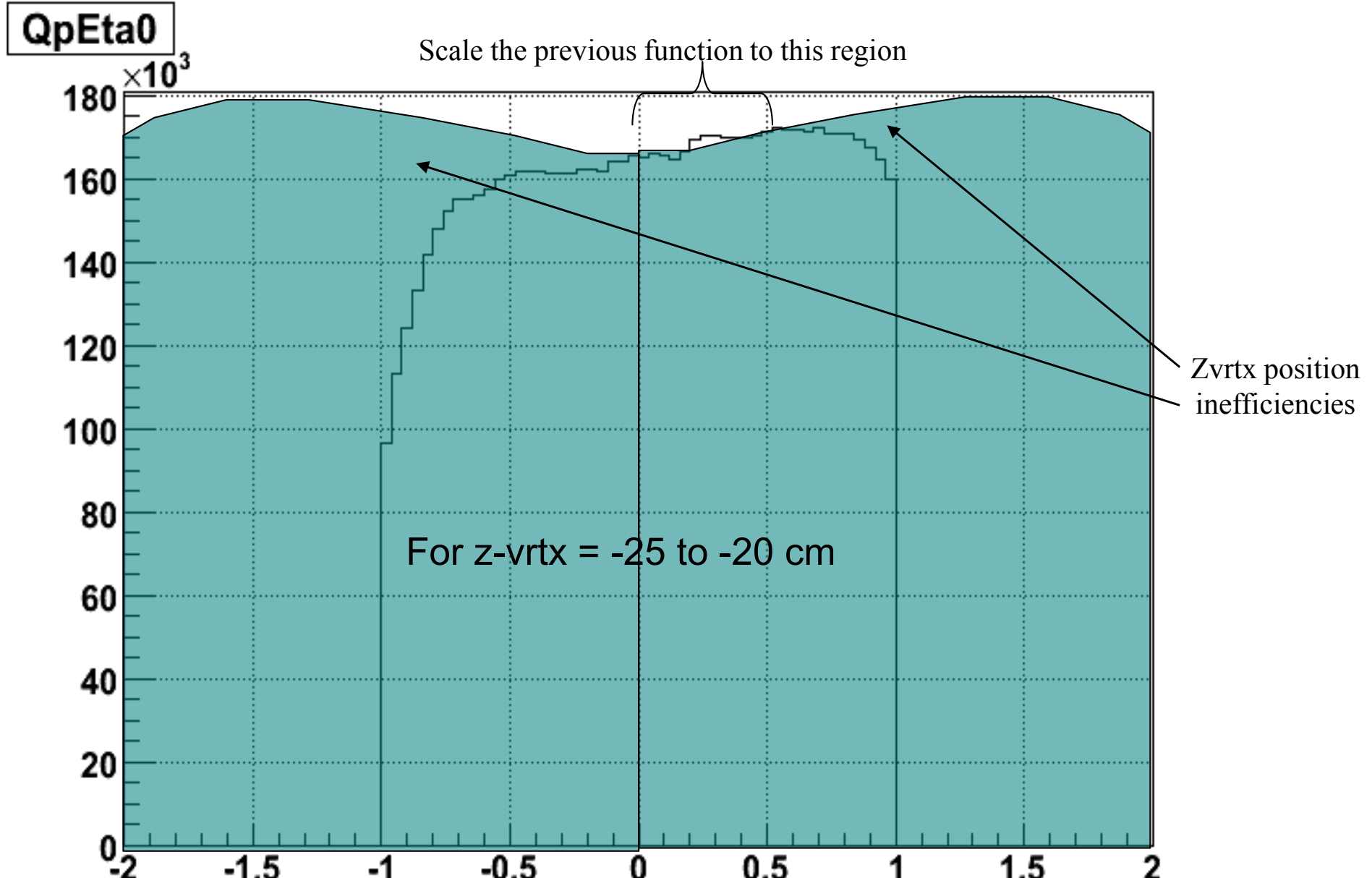


FIG. 5. The lower plot shows the shape of $dN_{ch}/d\eta$ at $\sqrt{s_{NN}} = 200$ GeV, obtained from the analog method. On top we show the pseudorapidity dependence of $R_{200/130}$ using the result of the analog method at both energies. In both plots, the error bars indicate the systematic uncertainty (90% confidence level).

Z-vertex and ZDC-rate Uncertainties



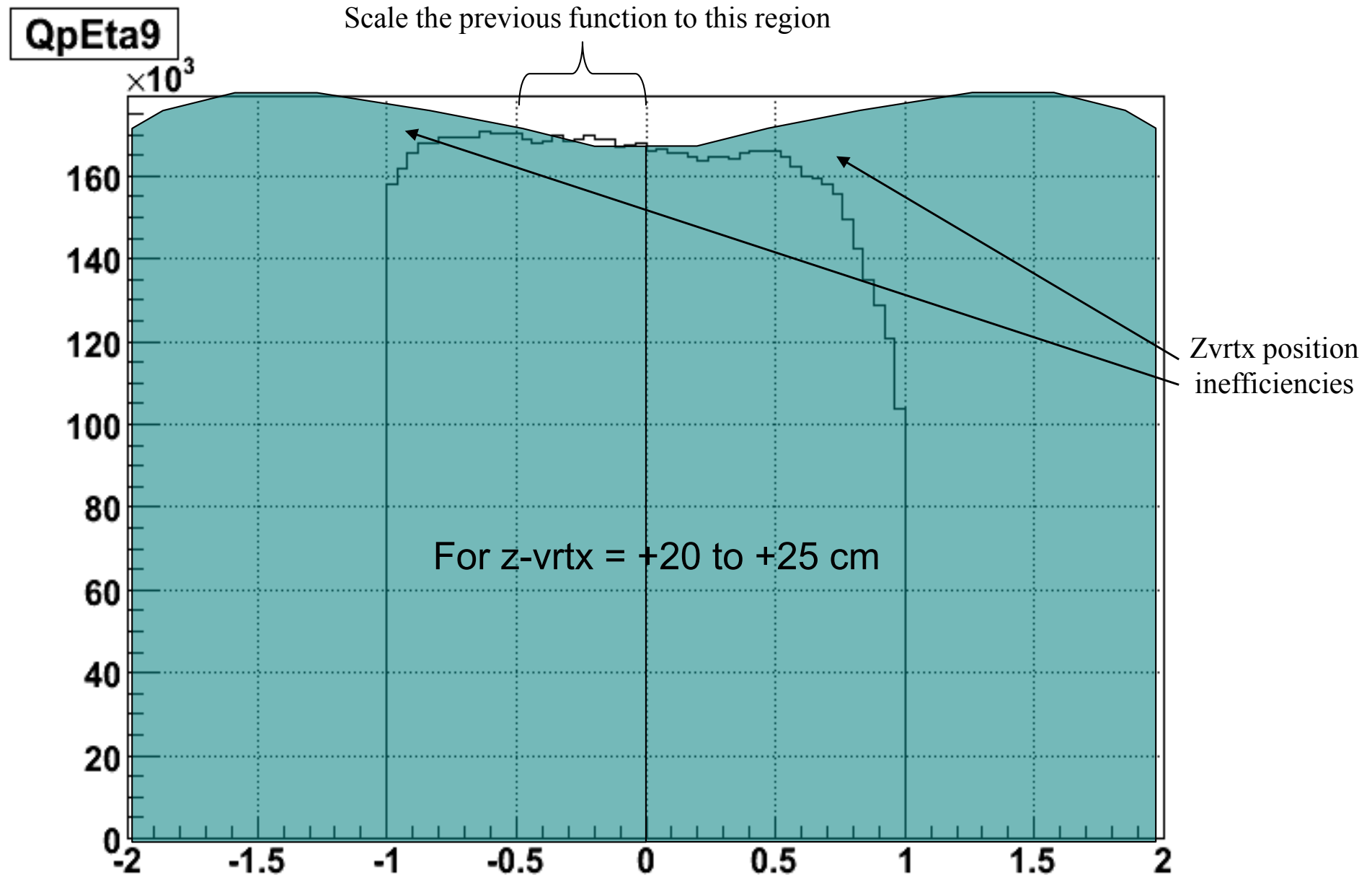
Z-vertex and ZDC-rate Uncertainties



Mon Feb 5 11:18:05 2007

From Fig.5.2, p.104, M.S. Daugherity's Thesis

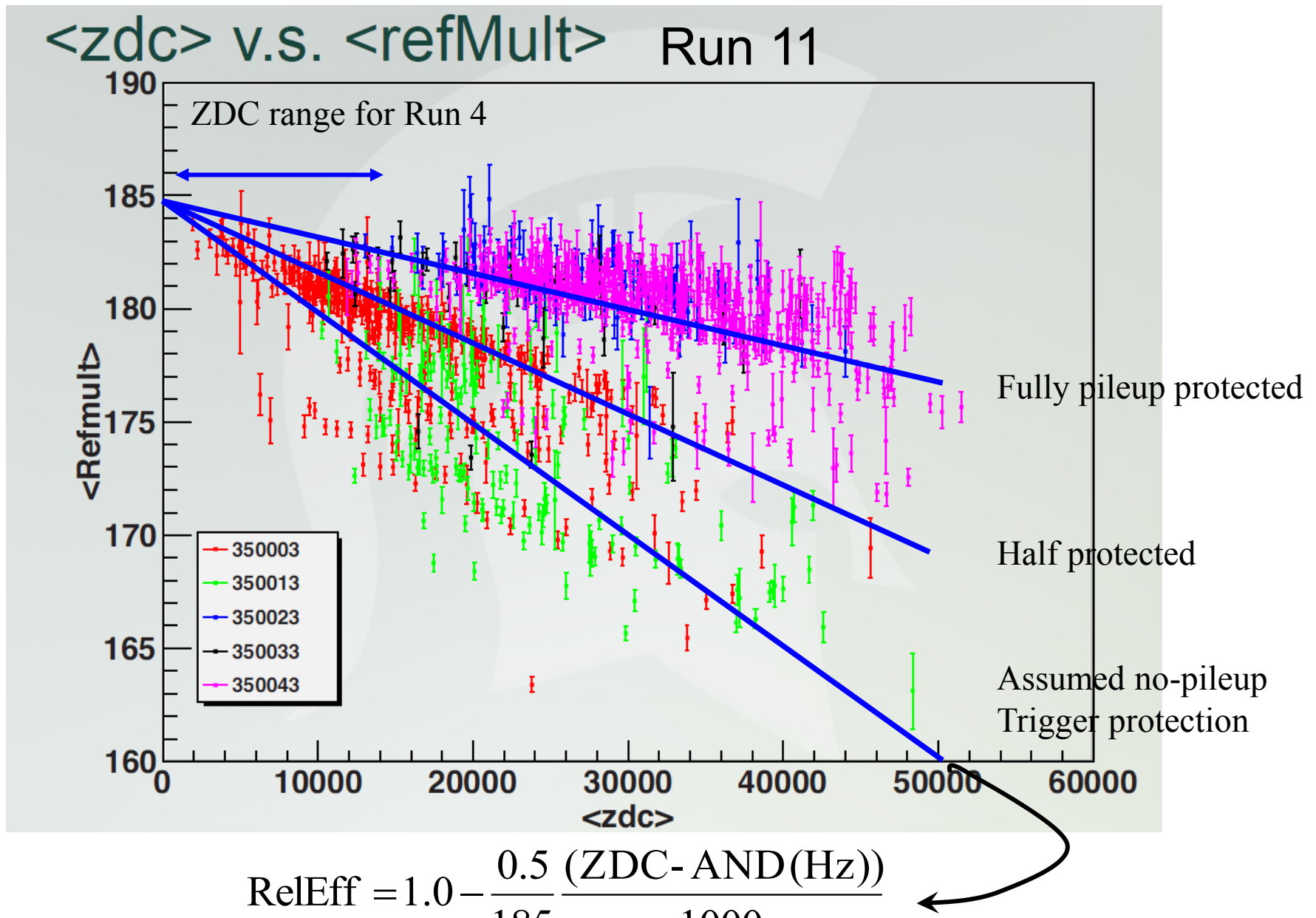
Z-vertex and ZDC-rate Uncertainties



Mon Feb 5 11:19:54 2007

From Fig.5.2, p.104, M.S. Daugherty's Thesis

Z-vertex and ZDC-rate Uncertainties

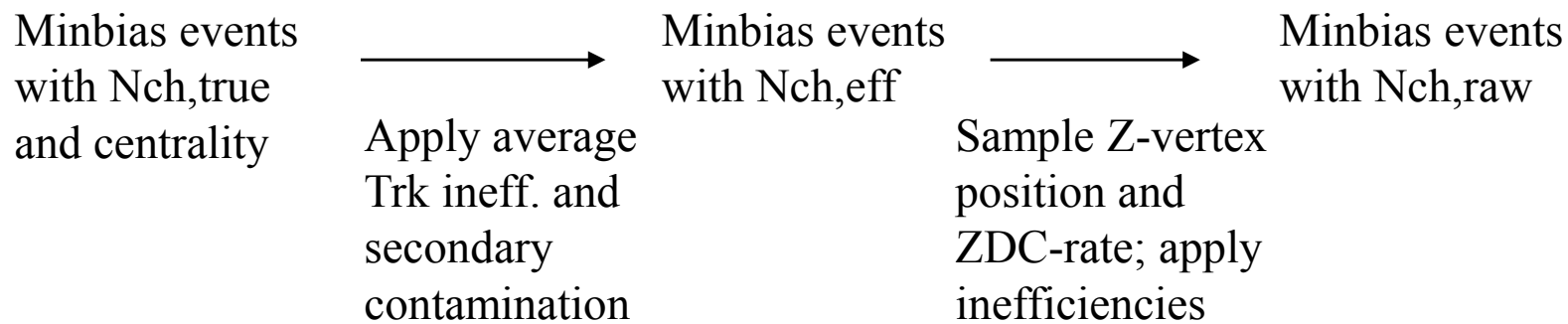


From Wang and Masui

A-7

Z-vertex and ZDC-rate Uncertainties

- I studied this effect with MC Glauber using the two-component Kharzeev & Nardi model for mean- N_{ch} plus an NBD event-wise multiplicity sampling. Pair weights were used to simulate the (y_t, y_t) correlations which were centrality dependent as in the data.



Z-vertex and ZDC-rate Uncertainties

- In our usual analysis the Nch,raw distribution is efficiency corrected by fitting the MC Glauber Nch,true distribution and assigning centrality bins to Nch,raw. This gives the “No RefMultCorr corrected” correlations.

$$N_{ch,true} = \frac{N_{ch,raw}(1 + \alpha' N_{ch,raw})}{\beta'}; \alpha' = \alpha = 0.000203, \beta = 0.797$$

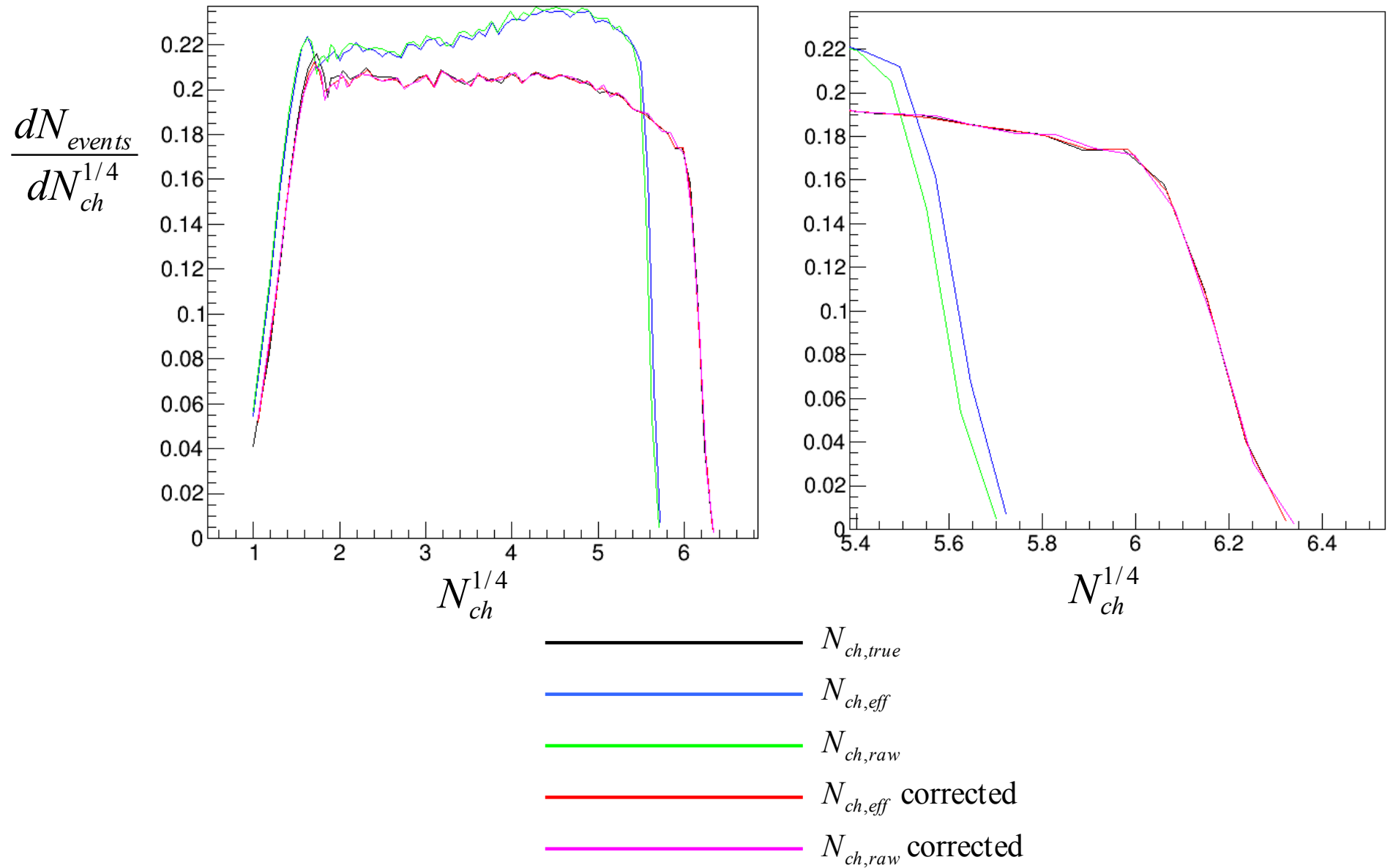
- In the RefMultCorr-type analysis Nch,raw is corrected for z-vertex position and ZDC-rate, then the resulting distribution is efficiency corrected to fit the MC Glauber Nch,true distribution, using the relation below. In this simulation this is just the ideal, or true-correlations.

$$N_{ch,true} = \frac{N_{ch,eff}(1 + \alpha N_{ch,eff})}{\beta}; \alpha = 0.000203, \beta = 0.819$$

- The difference between the true-correlations and the “no RefMultCorr corrected” correlations is the estimated, systematic effect of not including the z-vertex, ZDC-rate corrections, which I am treating as a systematic error.

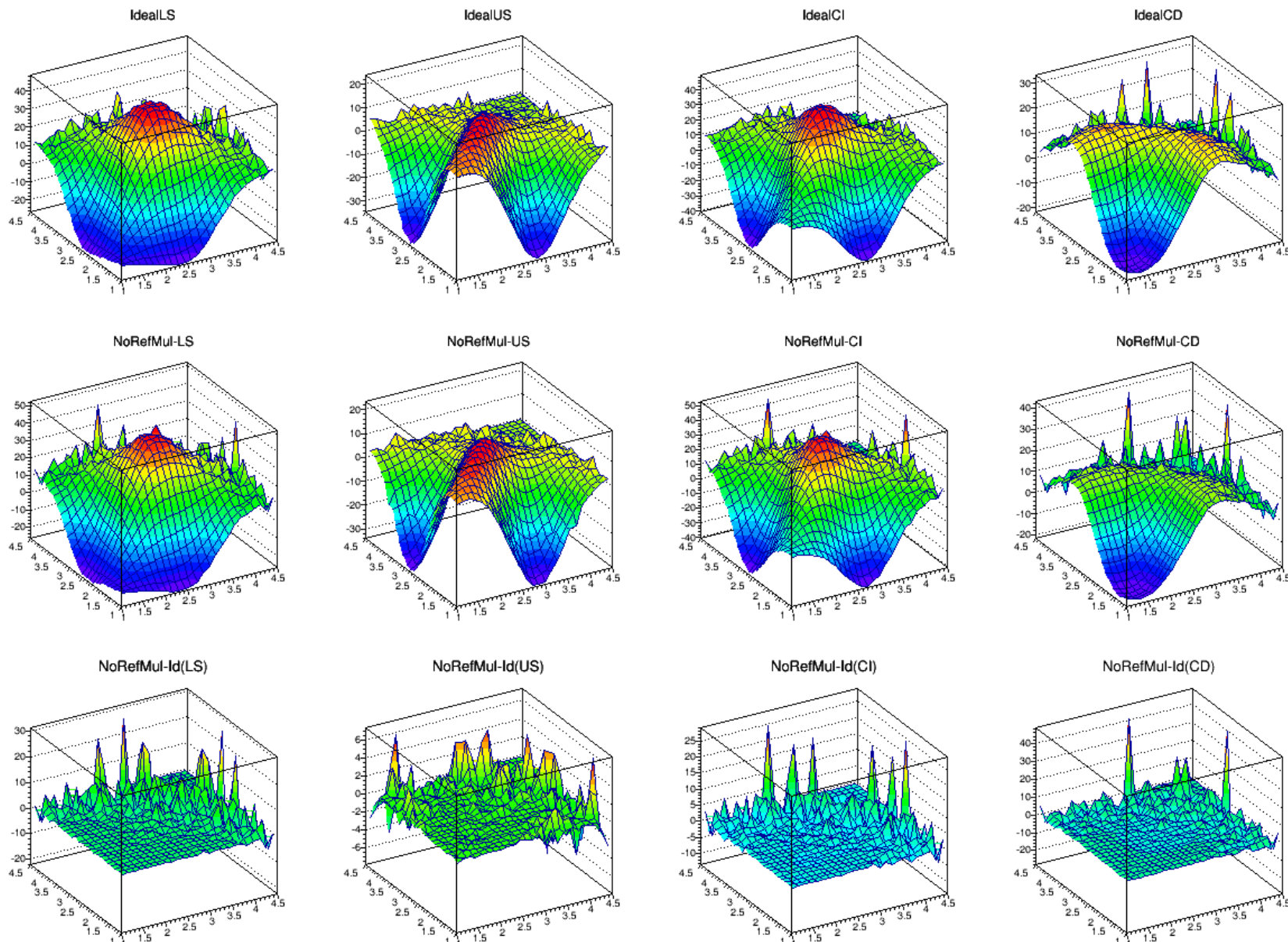
Z-vertex and ZDC-rate Uncertainties

MC Glauber – Kharzeev-Nardi – NBD simulation



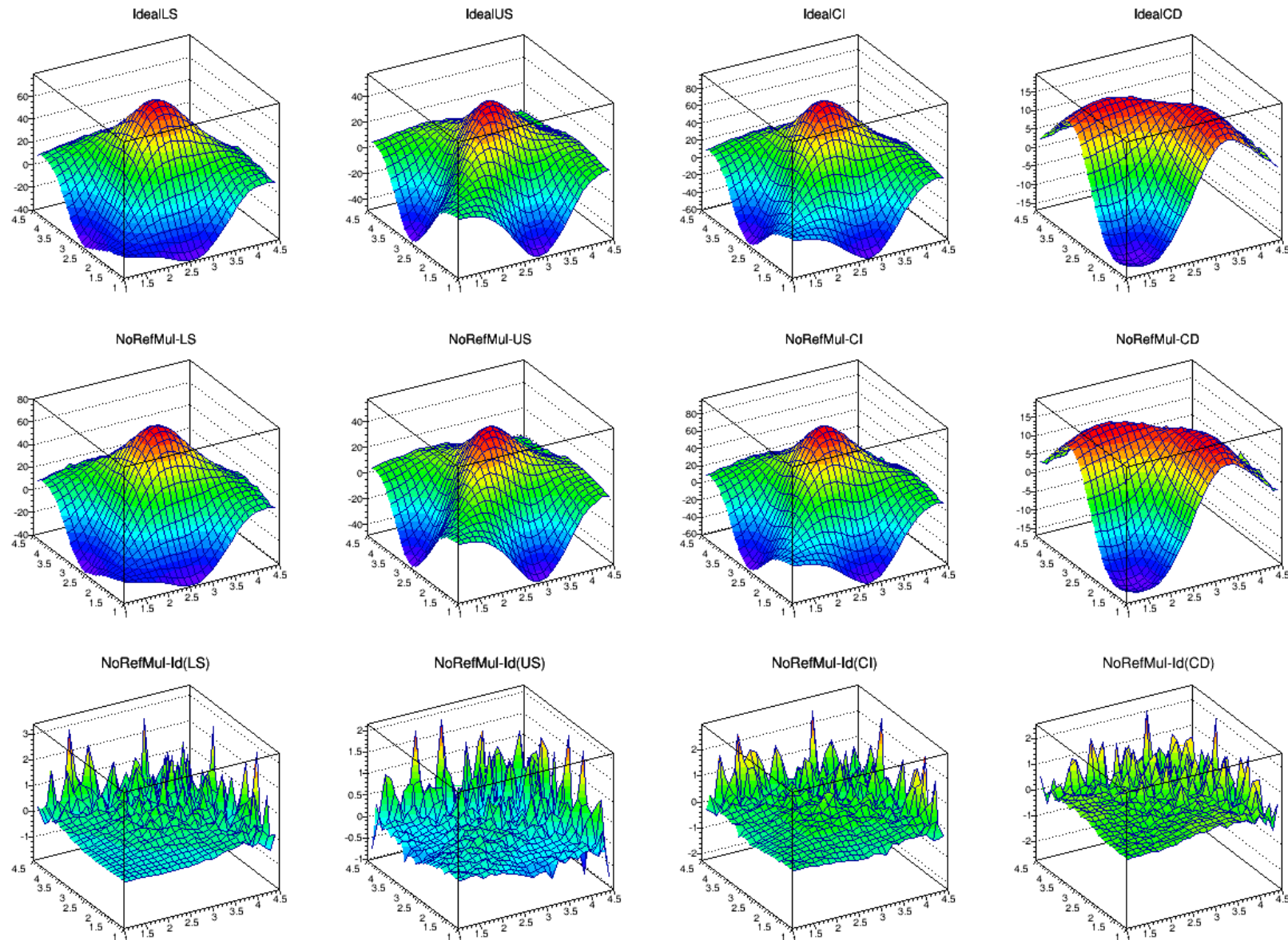
Z-vertex and ZDC-rate Uncertainties

Au+Au 200 GeV: 84-93%



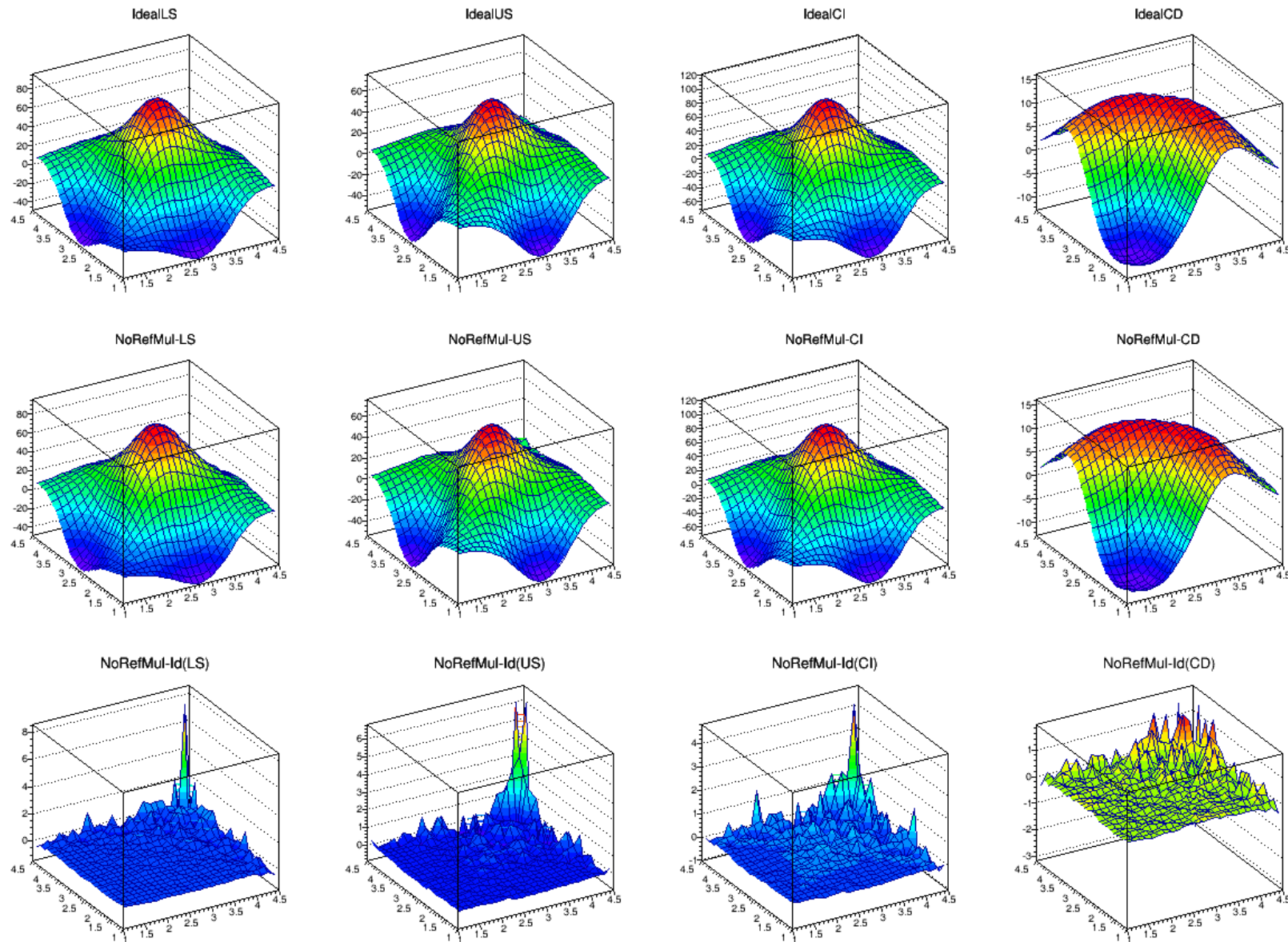
Z-vertex and ZDC-rate Uncertainties

Au+Au 200 GeV: 55-64%



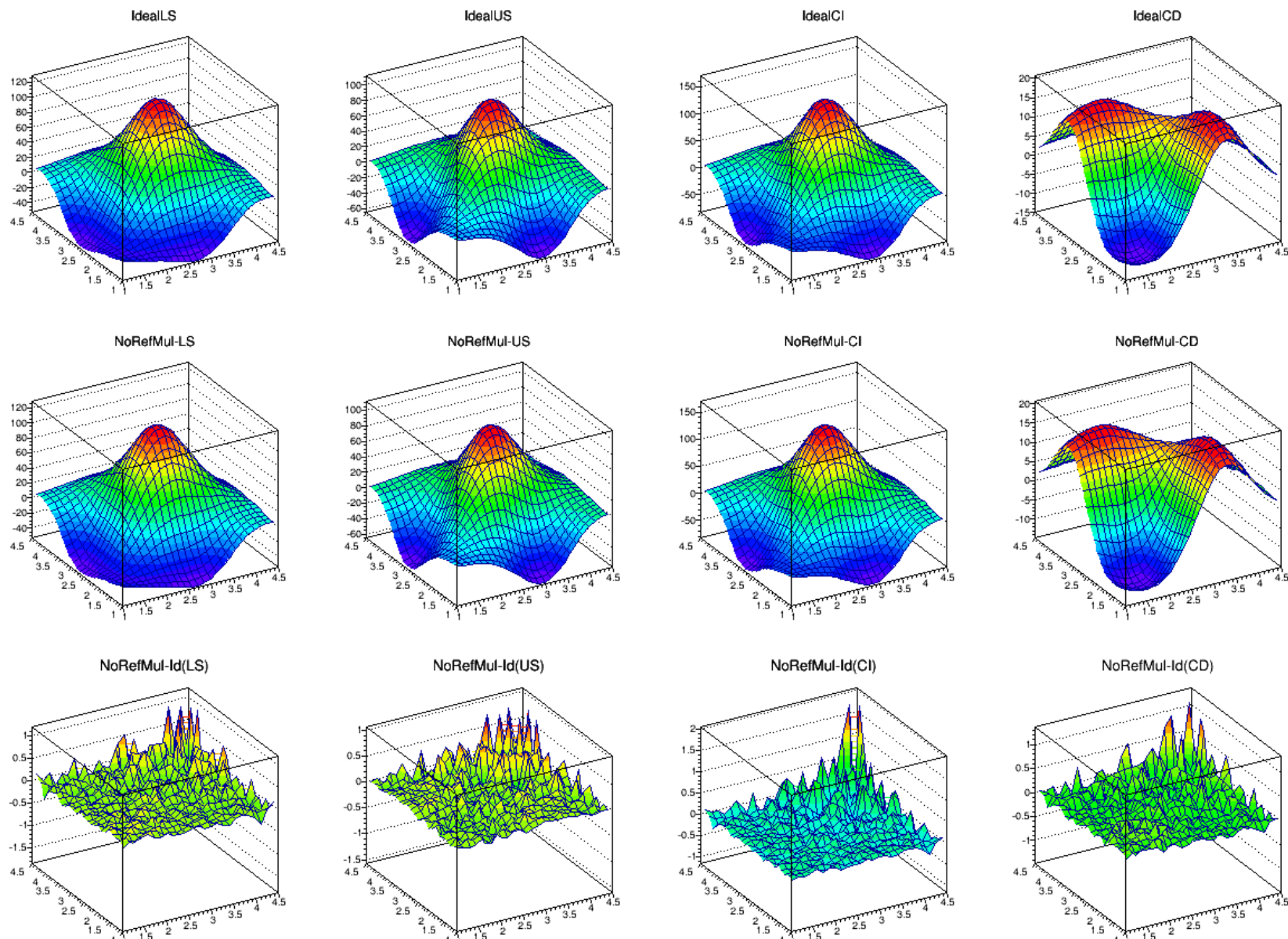
Z-vertex and ZDC-rate Uncertainties

Au+Au 200 GeV: 38-46%



Z-vertex and ZDC-rate Uncertainties

Au+Au 200 GeV: 9-18%



Z-vertex and ZDC-rate Uncertainties

- The effects are quite negligible because the additional tracking inefficiencies are only a few percent and the correlation dependence on multiplicity is smooth and approximately linear.
- For more extreme variations in tracking efficiency and strong, non-linear multiplicity dependence in the correlations we might see significant effects in correlation analysis.
- Nevertheless, these estimated effects are included as additional systematic uncertainty.

Appendix B

Pre-Factor Statistical and Systematic Errors

Part 1 – Calculation of statistical errors in
 $\Delta\rho/\sqrt{\{\rho_{\text{mix}}\}}$ including the pre-factor

Part 2 – Estimate of the systematic uncertainties
in the pre-factor

Part 1: Calculation of the Statistical Error for $\frac{\Delta\rho}{\sqrt{\rho_{mix}}}$

The quantity of interest for charge - independent correlations is

$$\frac{\Delta\rho}{\sqrt{\rho_{ref}}} = \sqrt{\rho_{ref}} \frac{\Delta\rho}{\rho_{ref}} = \sqrt{\alpha\rho_{me}} \frac{\rho_{se} - \alpha\rho_{me}}{\alpha\rho_{me}}$$

where

$$\alpha = \frac{\bar{N}_{ch} - 1}{\bar{N}_{ch}}, \bar{N}_{ch} \text{ is the mean, charged particle multiplicity.}$$

To simplify the notation we define for each (y_{t1}, y_{t2}) bin quantities

$$S \equiv \rho_{se}, M \equiv \alpha\rho_{me}$$

and calculate the error squared (i.e. variance) of $(S - M)/\sqrt{M}$.

$$Err^2 \left(\frac{S - M}{\sqrt{M}} \right) = \left\langle \left(\frac{\partial \left(\frac{(S - M)}{\sqrt{M}} \right)}{\partial S} (\delta S) + \frac{\partial \left(\frac{(S - M)}{\sqrt{M}} \right)}{\partial M} (\delta M) \right)^2 \right\rangle$$

where $\delta(S)$ and $\delta(M)$ denote the random fluctuations in the same - and mixed - event densities for a given set of data. The outer brackets indicate an average over many statistically independent, but otherwise identical data sets.

The partial derivatives are evaluated at the mean values of S, M given by \bar{S}, \bar{M} where

$$\frac{\partial \left(\frac{(S-M)}{\sqrt{M}} \right)}{\partial S} = \frac{1}{\sqrt{\bar{M}}} \quad \text{and} \quad \frac{\partial \left(\frac{(S-M)}{\sqrt{M}} \right)}{\partial M} = -\frac{1}{2\sqrt{\bar{M}}} \left(1 + \frac{\bar{S}}{\bar{M}} \right)$$

$$Err^2 \left(\frac{(S-M)}{\sqrt{M}} \right) = \left\langle \frac{(\delta S)^2}{\bar{M}} + \frac{(\delta M)^2}{4\bar{M}} \left(1 + \frac{\bar{S}}{\bar{M}} \right)^2 - \frac{1}{\bar{M}} \left(1 + \frac{\bar{S}}{\bar{M}} \right) (\delta S \delta M) \right\rangle$$

For the present application $\bar{S} \approx \bar{M}$ if the correlation amplitude is small relative to \bar{M} , which it is. The above simplifies to

$$Err^2 \left(\frac{(S-M)}{\sqrt{M}} \right) \approx \frac{1}{\bar{M}} \left[\langle (\delta S)^2 \rangle + \langle (\delta M)^2 \rangle - 2 \langle (\delta S \delta M) \rangle \right]$$

in terms of the variances of S, M and the covariance.

The errors calculated previously in the analysis were for the quantity $(S - M) / M$ which were then scaled by the pre-factor \sqrt{M} . The corresponding scaled variance is

$$\begin{aligned} \left(\sqrt{\bar{M}}\right)^2 Err^2 \left(\frac{S - M}{M} \right) &= \left(\sqrt{\bar{M}}\right)^2 \left\langle \left(\frac{\delta S}{\bar{M}} - \frac{\bar{S} \delta M}{\bar{M}^2} \right)^2 \right\rangle \\ &= \bar{M} \left\langle \frac{(\delta S)^2}{\bar{M}^2} + \frac{\bar{S}^2 (\delta M)^2}{\bar{M}^4} - \frac{2\bar{S}}{\bar{M}^3} (\delta S \delta M) \right\rangle \\ &\approx \frac{1}{\bar{M}} \left[\langle (\delta S)^2 \rangle + \langle (\delta M)^2 \rangle - 2 \langle (\delta S \delta M) \rangle \right] \end{aligned}$$

which is identical to the above variance which explicitly included the pre-factor. Below, we demonstrate the accuracy of this relation between errors using a simple MonteCarlo model.

The reported correlation quantity is given by

$$\begin{aligned}
PF \frac{\Delta\rho}{\rho_{ref}} &= PF \frac{\rho_{se} - \alpha\rho_{me}}{\alpha\rho_{me}} = \frac{PF}{\sqrt{\alpha\rho_{me}}} \left[\sqrt{\alpha\rho_{me}} \frac{\rho_{se} - \alpha\rho_{me}}{\alpha\rho_{me}} \right] \\
&= \frac{1}{\sqrt{\alpha}} \left[\frac{d^2 N_{ch} / dy_{t1} d\eta_1 \quad d^2 N_{ch} / dy_{t2} d\eta_2}{(\Delta\eta)^2 \quad d^2 N_{ch} / dy_{t1} d\eta_1 \quad d^2 N_{ch} / dy_{t2} d\eta_2} \right]^{1/2} \left[\sqrt{\alpha\rho_{me}} \frac{\rho_{se} - \alpha\rho_{me}}{\alpha\rho_{me}} \right] = \frac{1}{\Delta\eta\sqrt{\alpha}} \left[\sqrt{\alpha\rho_{me}} \frac{\rho_{se} - \alpha\rho_{me}}{\alpha\rho_{me}} \right] \\
&= \frac{1}{\Delta\eta\sqrt{\alpha}} \left[\sqrt{M} \frac{S - M}{M} \right] = \frac{1}{\Delta\eta\sqrt{\alpha}} \left[\frac{S - M}{\sqrt{M}} \right]
\end{aligned}$$

where definitions for S, M were substituted, PF is the charge pre-factor, $\Delta\eta = 2$ is the TPC acceptance and $\sqrt{\alpha} \approx 1$ for all centralities.

The variance of the final, reported correlation quantity can be expressed as

$$\begin{aligned}
Err^2 \left(PF \frac{\Delta\rho}{\rho_{ref}} \right) &= \left(\frac{1}{\Delta\eta\sqrt{\alpha}} \right)^2 Err^2 \left(\frac{S - M}{\sqrt{M}} \right) = \left(\frac{\sqrt{M}}{\Delta\eta\sqrt{\alpha}} \right)^2 Err^2 \left(\frac{S - M}{M} \right) \\
&= \left(\frac{\alpha\rho_{me}}{\Delta\eta^2\alpha} \right) Err^2 \left(\frac{S - M}{M} \right) = \frac{1}{\Delta\eta^2} \left[(\Delta\eta)^2 \frac{d^2 N_{ch} / dy_{t1} d\eta_1 \quad d^2 N_{ch} / dy_{t2} d\eta_2}{d^2 N_{ch} / dy_{t1} d\eta_1 \quad d^2 N_{ch} / dy_{t2} d\eta_2} \right] Err^2 \left(\frac{S - M}{M} \right) \\
Err \left(PF \frac{\Delta\rho}{\rho_{ref}} \right) &= \left[\frac{d^2 N_{ch} / dy_{t1} d\eta_1 \quad d^2 N_{ch} / dy_{t2} d\eta_2}{d^2 N_{ch} / dy_{t1} d\eta_1 \quad d^2 N_{ch} / dy_{t2} d\eta_2} \right]^{1/2} Err \left(\frac{S - M}{M} \right) \equiv (PF) Err \left(\frac{\Delta\rho}{\rho_{ref}} \right); QED
\end{aligned}$$

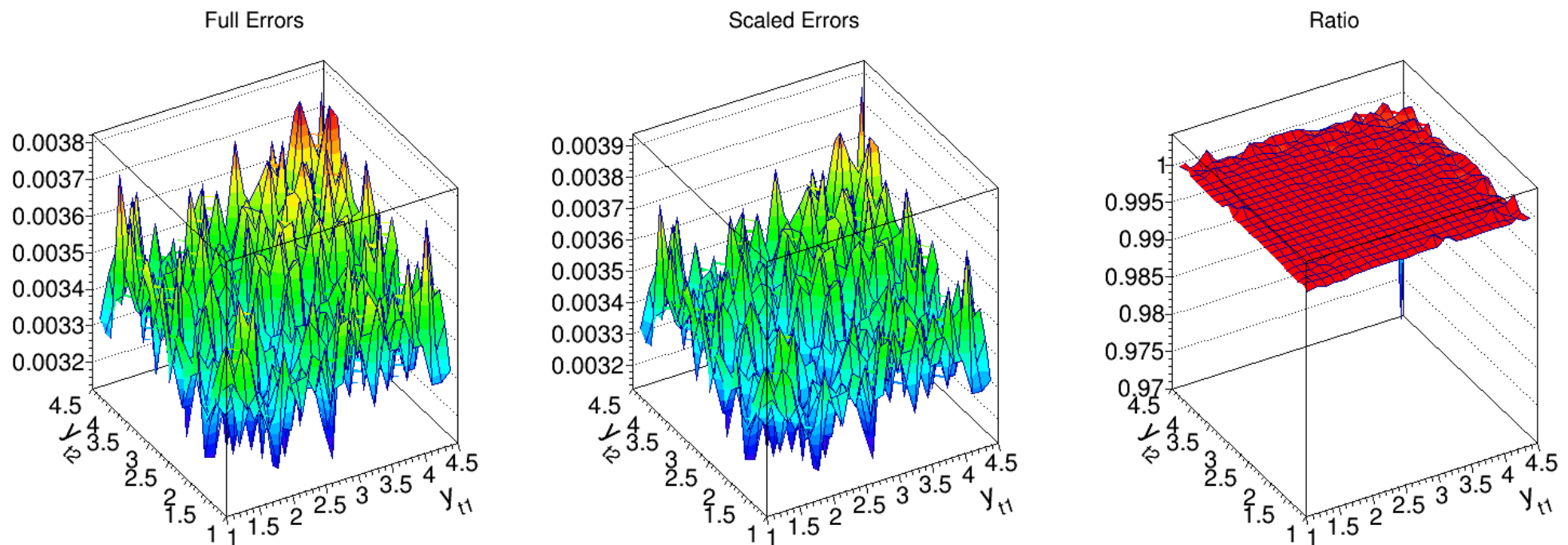
Monte Carlo study of statistical errors

The Monte Carlo model includes the following:

- 1) two-component multiplicity production where the soft component is represented with a Levy distribution with temperature (T) and exponent (n); the hard component with a Gaussian on y_t , matched to a power-law tail.
- 2) event-wise T is sampled from a Gaussian with $\sigma \sim$ few percent of $\langle T \rangle$
- 3) event-wise number of semi-hard particles is sampled from a Poisson
- 4) soft and hard component particle y_t values are determined by sampling the Levy and Gaussian + power-law distributions, respectively.

Simulations were run for the 38-46% centrality bin where all events had a total soft plus hard multiplicity of 240 in the TPC acceptance with average soft and hard component multiplicities of 160 and 80, respectively. Levy parameters T and n were determined by fits to the measured p_t spectra. The parameters of the hard component distribution were taken from the estimates in Trainor, Phys. Rev. C **80**, 044901 (2009). The analysis included 1000 independent event collections, each having 100,000 events. The results are shown on the next page.

The plot on the left shows the simulated errors for $\Delta\rho/\sqrt{\rho_{\text{mix}}}$, the middle plot shows the scaled errors given by $\sqrt{\rho_{\text{mix}}} \times \text{errors in } \Delta\rho/\rho_{\text{mix}}$, and the right-hand plot shows the ratio of the left-hand plot to the middle. The two methods for calculating errors are consistent.



Part 2: Estimates of the Systematic Uncertainties

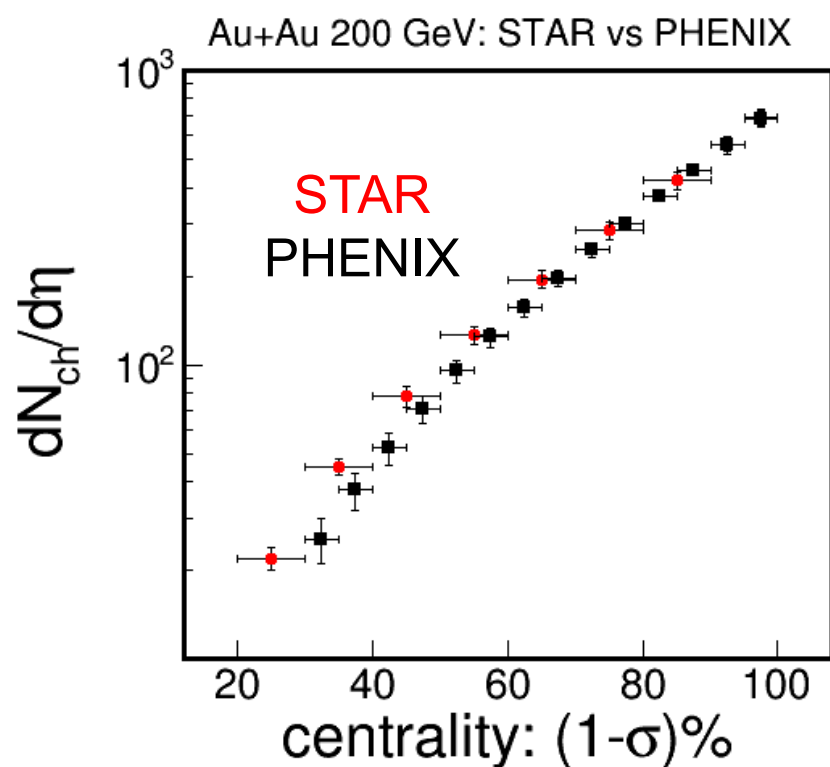
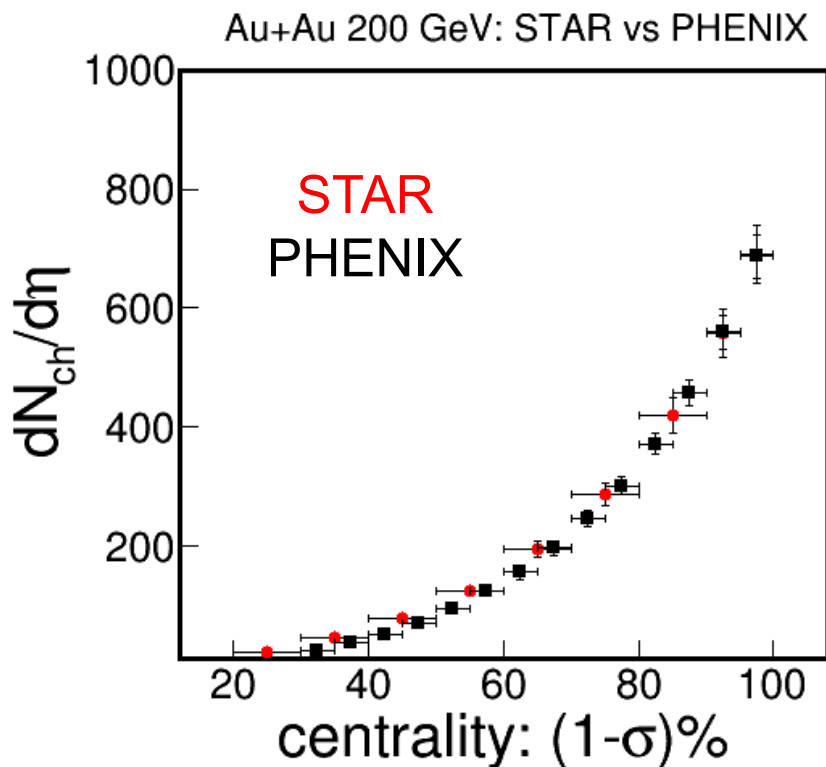
Systematic uncertainties in the charge-particle pre-factor derive from those in the measured spectra data, the interpolation required to convert the published spectra data to the Run 2 and 4 offset centrality bins, and the Levy model used to represent the distribution. The relevant information includes the following:

- 1) The STAR and PHENIX spectra data and errors which are dominated by systematic uncertainties
- 2) The STAR and PHENIX centrality dependent multiplicity uncertainties
- 3) Uncertainties in the centrality cross section fractions for the Runs 2 and 4 bins
- 4) The Levy model fit quality to the spectra data used to interpolate to the Run 4 bins

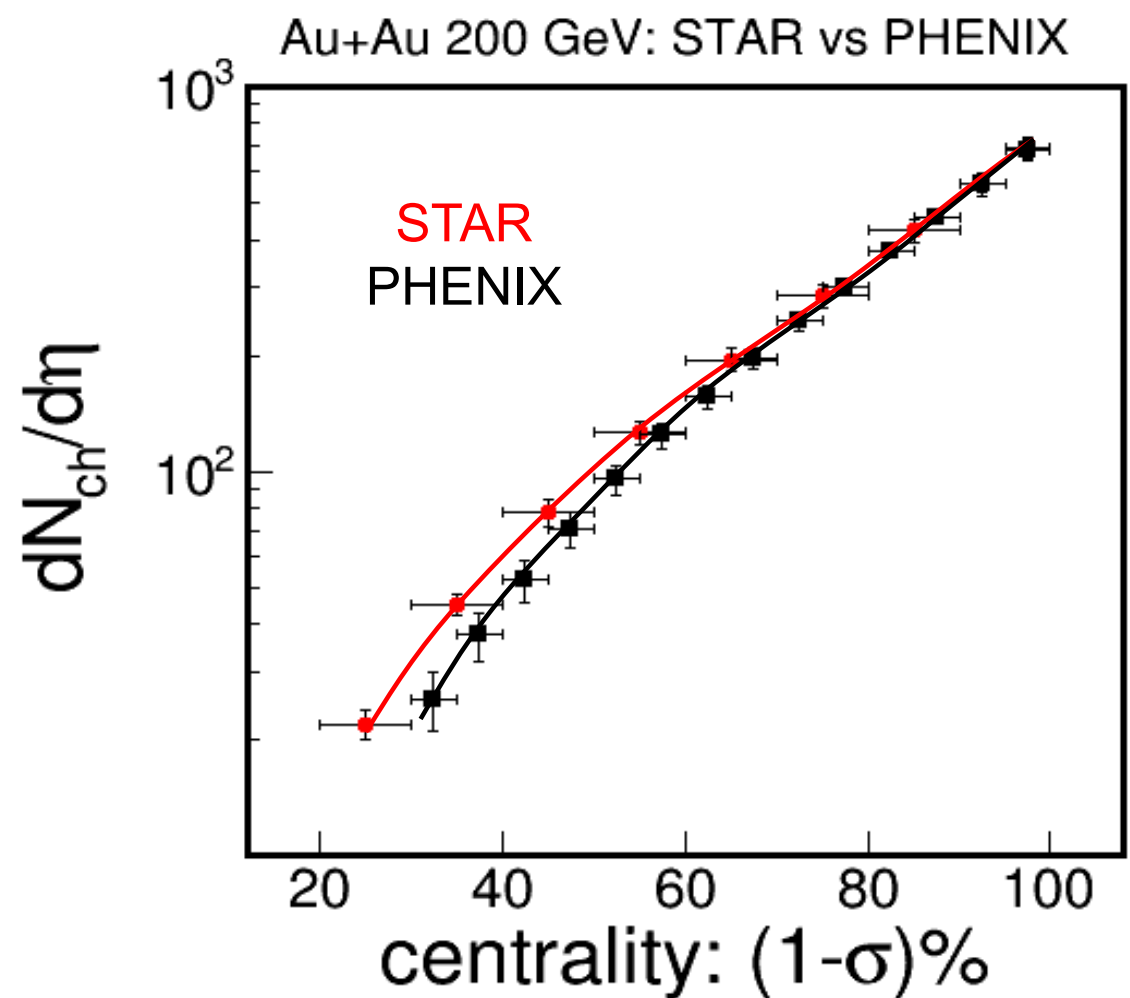
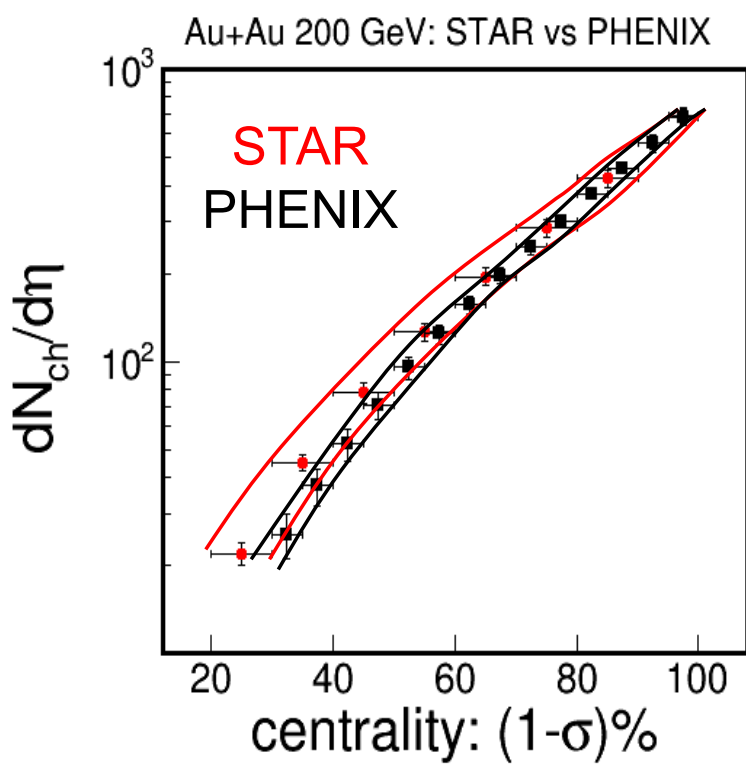
Each of these were studied; the effects deemed to be significant include the systematic uncertainties in the measured multiplicity densities $dN_{ch}/d\eta$ from STAR. The systematic differences between the STAR and PHENIX $dN_{ch}/d\eta$ were not included for reasons given below. The STAR versus PHENIX p_t spectra distribution shape differences, and the statistically significant Levy model fit residuals for the PHENIX spectra were not included because the systematic uncertainties in the pre-factor we are reporting should be consistent within the STAR experiment correction procedures. The Levy model fit residuals for the STAR spectra data were within 1 to 2-sigma and therefore do not add to the systematic uncertainties. Further details of the analysis are discussed in the following pages. The method for estimating the systematic uncertainties for all charge-particle pre-factors used in the analysis is given at the end.

Normalization uncertainty in $dN_{ch}/d\eta$:

Efficiency, acceptance and background contamination corrected measurements of $dN_{ch}/d\eta$ for minimum-bias Au+Au collisions at 200 GeV were reported by STAR [Phys. Rev. C **79**, 034909 (2009) in Table II] and by PHENIX [Phys. Rev. C **71**, 034908 (2005) in Table XIII]. Uncertainties vary from about 7% to 9% and 5% to 18% for STAR and PHENIX, respectively, from most-central to most-peripheral collisions. Uncertainties are dominated by systematics. The data are compared below in both linear and semi-log scales.



Although the error bands for the two data sets tend to overlap (see left panel below), the PHENIX and STAR data systematically diverge for more peripheral collisions (right panel, left-hand side of plot).



The PHENIX $dN_{ch}/d\eta$ also tend to fall below the RHIC average for more-peripheral collisions and the STAR measurements tend to agree with PHOBOS and BRAHMS in peripheral. We therefore have adopted the STAR $dN_{ch}/d\eta$ data for the present Run-4 analysis and pre-factor.

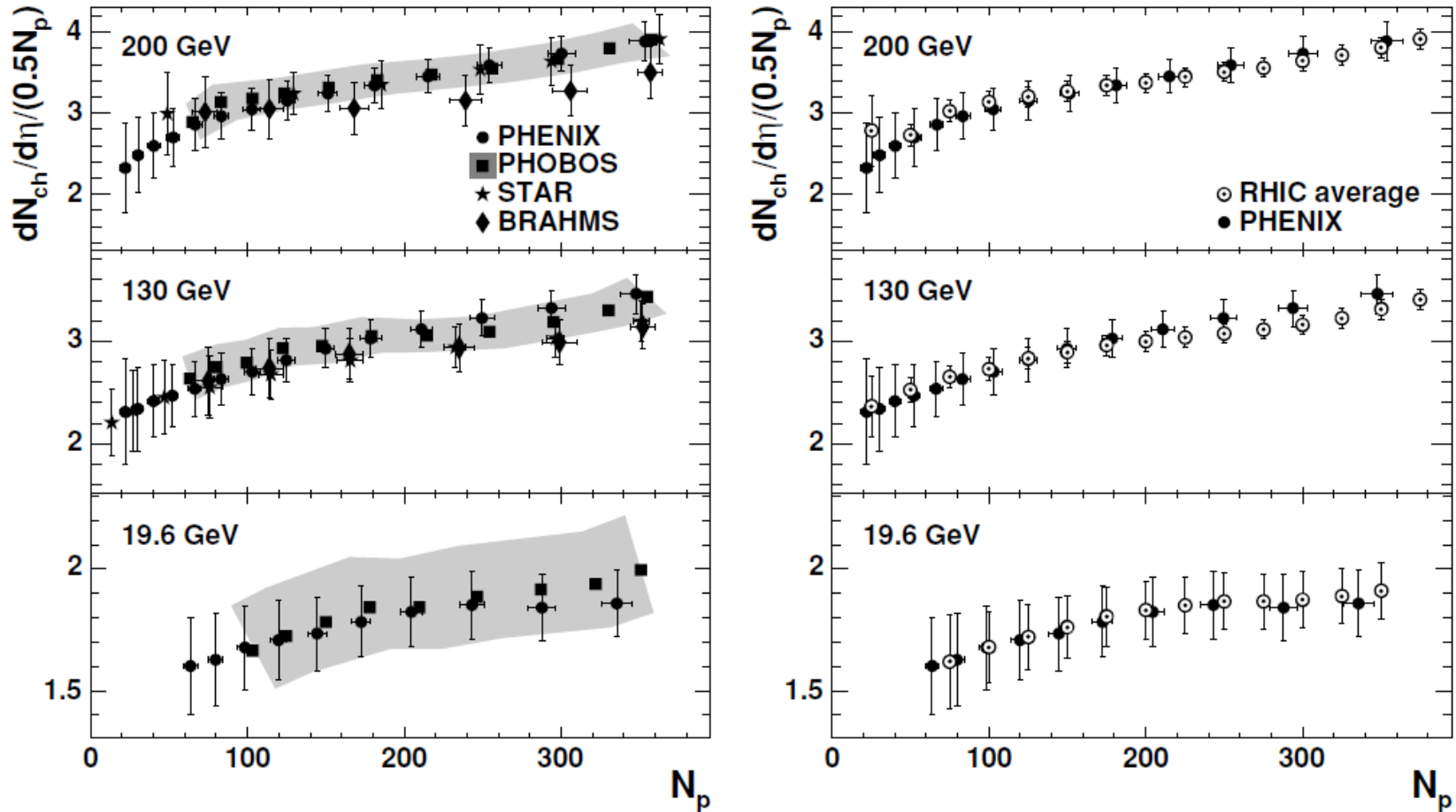
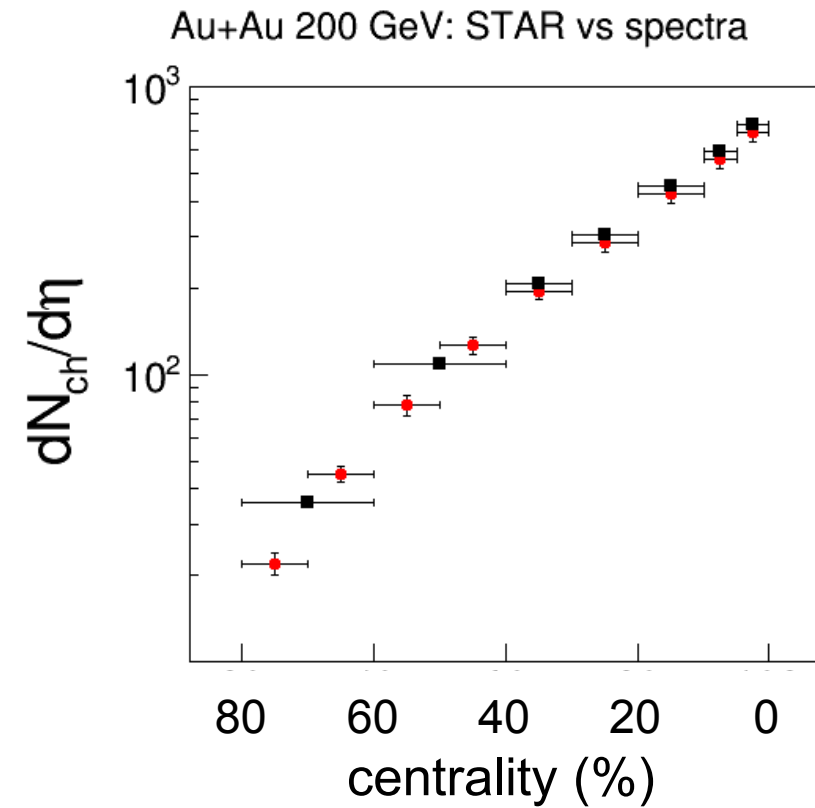
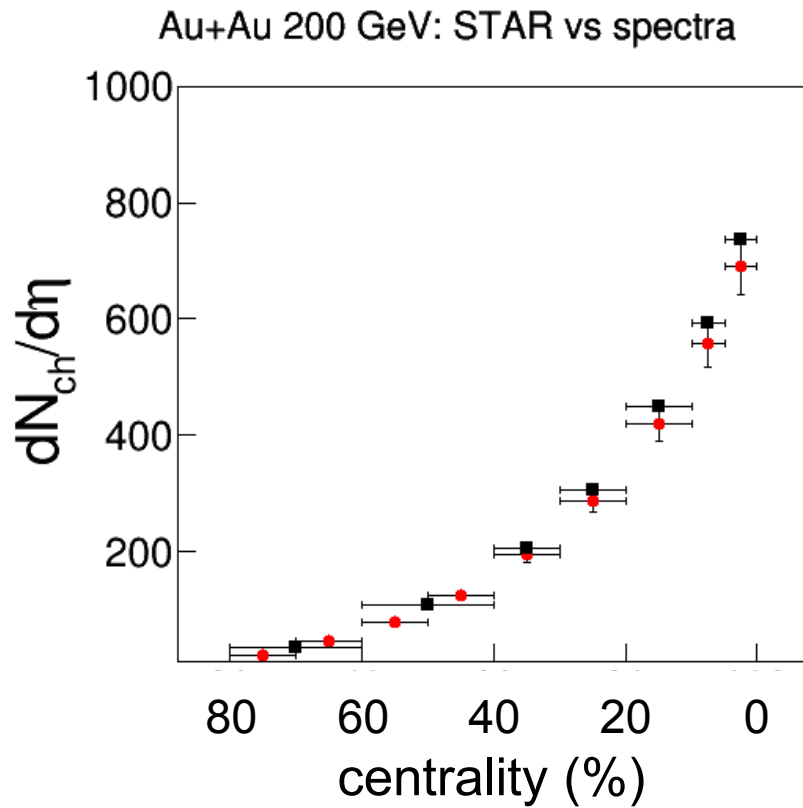


FIG. 9. Left panel: $dN_{ch}/d\eta$ per pair of N_p measured by the four RHIC experiments at different energies. The shaded area is the PHOBOS systematic error. Right panel: RHIC average values (including PHENIX) compared to the PHENIX results.

We also compared the STAR published $dN_{ch}/d\eta$ with the STAR spectra data extrapolated to $p_T = 0$ and integrated from $p_T = 0$ to ~ 11 GeV/c, to check the consistency. We used the STAR published $dN_{ch}/d\eta$ in Phys. Rev. C **79**, 034909 (2009), Table II which is from STAR Phys Rev Lett **92**, 112301 (2004) shown only in two figures.

We compared these results with the spectra data in STAR Phys Rev Lett **91**, 172302 (2003) which were fitted with a Maxwell-Boltzmann distribution from $p_T = 0.2$ to 1 GeV/c and extrapolated to $p_T = 0$. The MB and data were integrated from 0 to the maximum $p_T \sim 11$ GeV/c.

Published STAR $dN_{ch}/d\eta$
Integrated STAR spectra

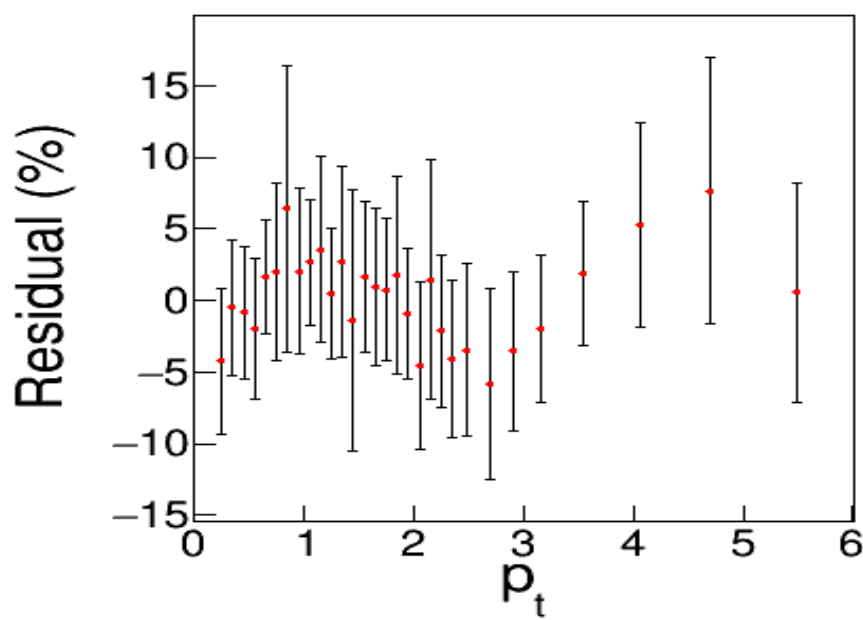


The spectra estimate is about 7% larger than the published data, uniform across all centralities. Each centrality bin is within 1-sigma of the quoted uncertainties in PRC 79, 034909 (2009) Table II.

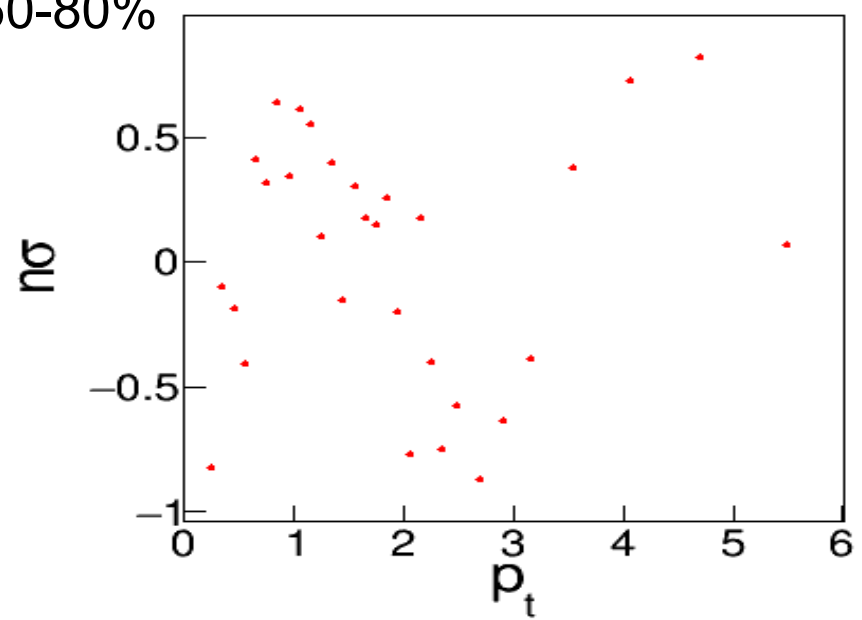
Systematic discrepancies between spectra data and Levy model fits:

Levy model fits to the STAR spectra distributions are used to estimate the actual distributions for the Run 4 centrality bins. The fits are generally good out to about 5 GeV/c. It is possible however that the model cannot account for all statistically significant shapes in the data, leading to systematic error. In the following plots we show the Levy model fit residuals for the available STAR [Phys. Rev. Lett. 91, 172302 (2003)] p_t spectra. Each pair of figures shows the fit residuals as a function of p_t . The left figure shows the residual as a percentage of the yield; the percentage errors in the spectra data are also included for reference. The right-hand figure shows the ratio $n\sigma = \text{residual}/(\text{total error})$, where the total error is the quadrature sum of the statistical and systematic errors.

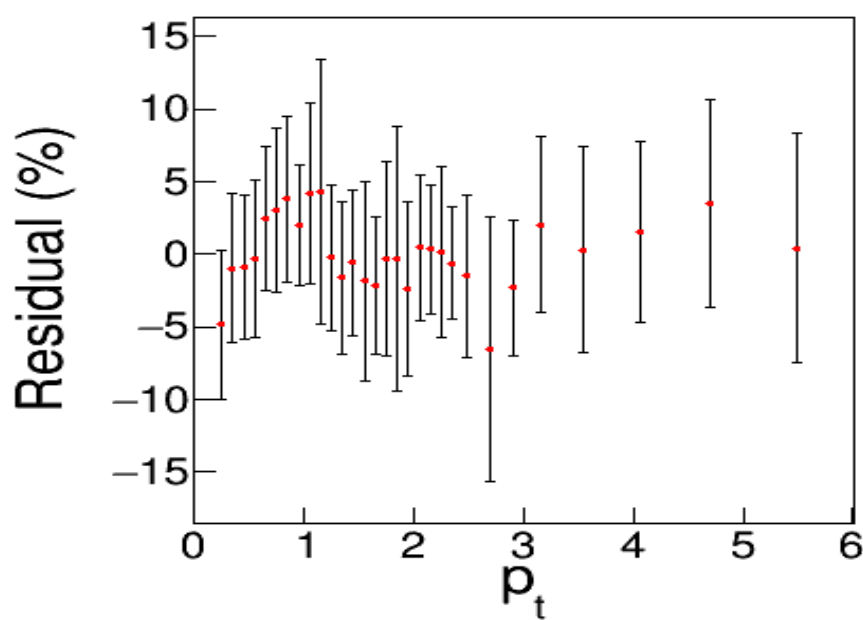
STAR: Au+Au 200 GeV 60-80% Residual (%)



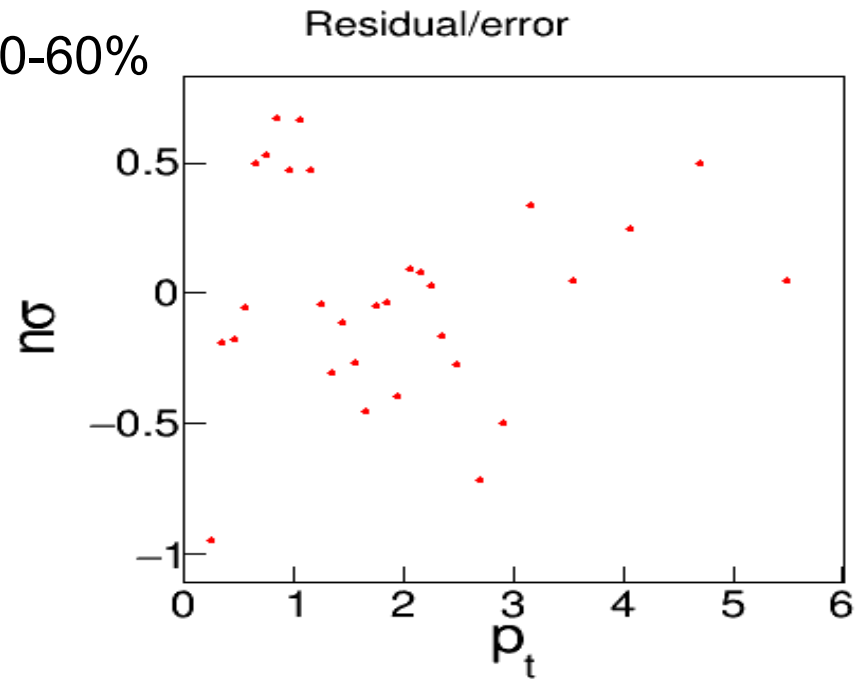
STAR: 60-80%



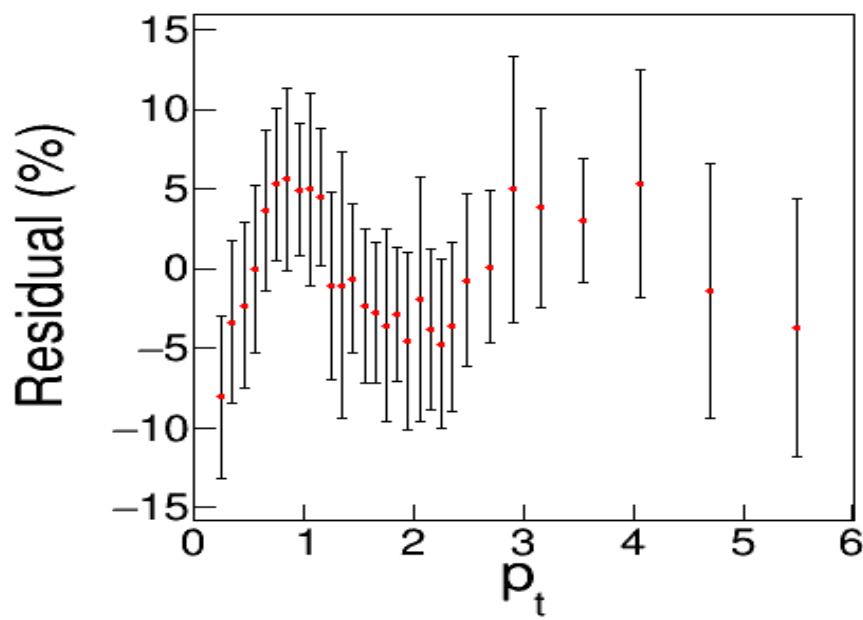
STAR: Au+Au 200 GeV 40-60% Residual (%)



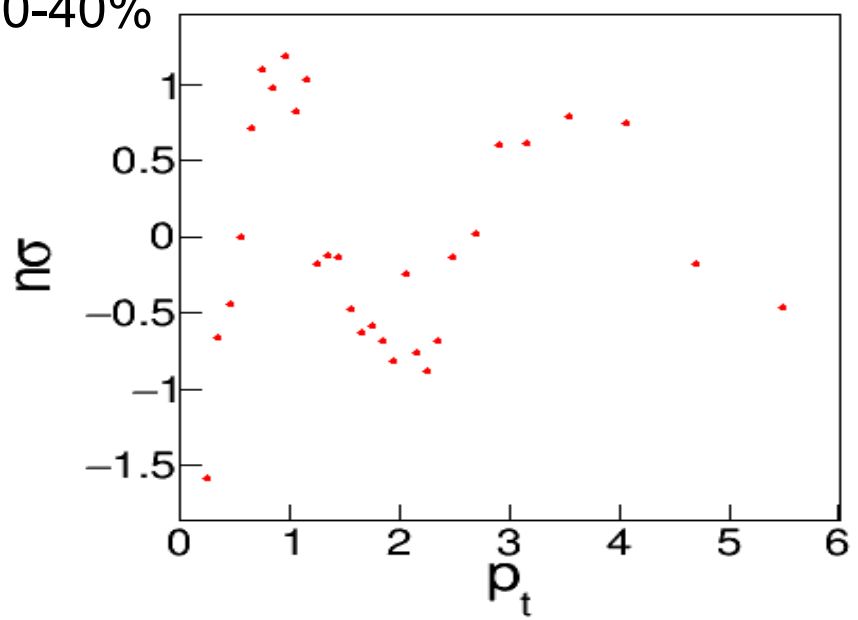
STAR: 40-60%



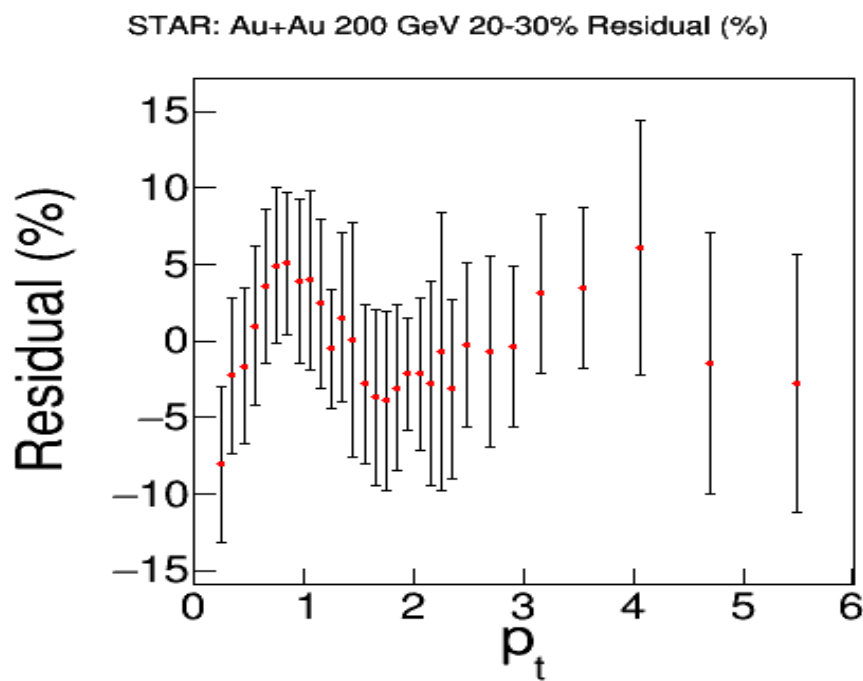
STAR: Au+Au 200 GeV 30-40% Residual (%)



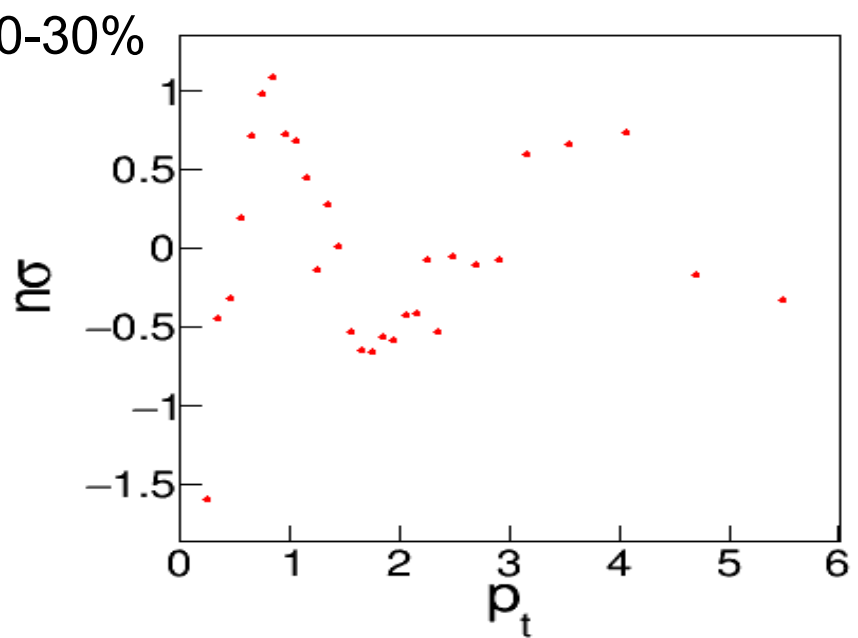
STAR: 30-40%



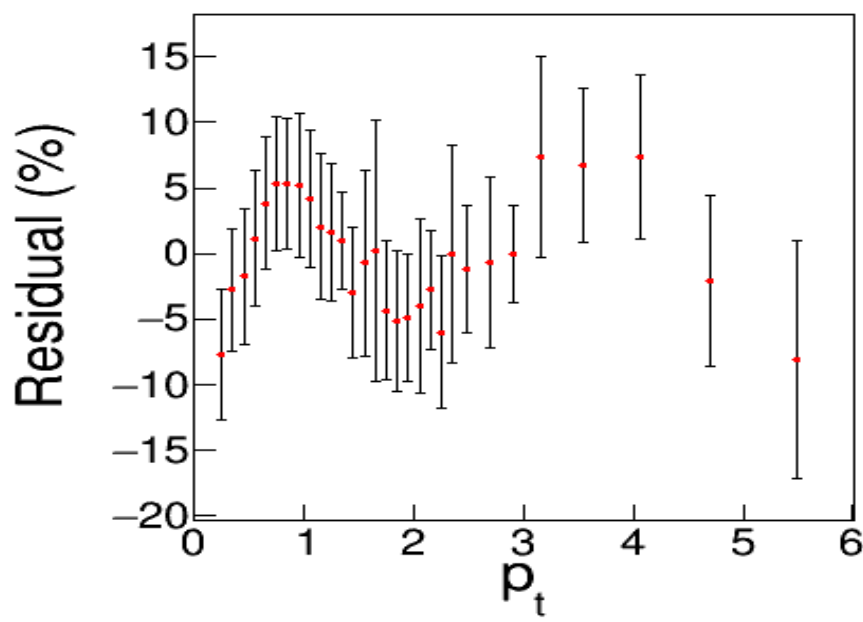
Residual/error



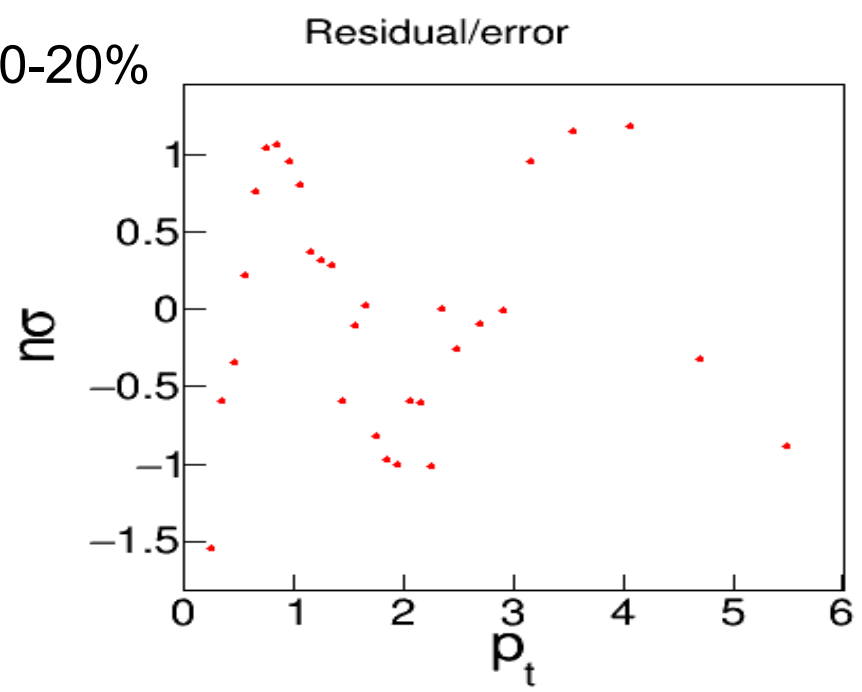
STAR: 20-30%



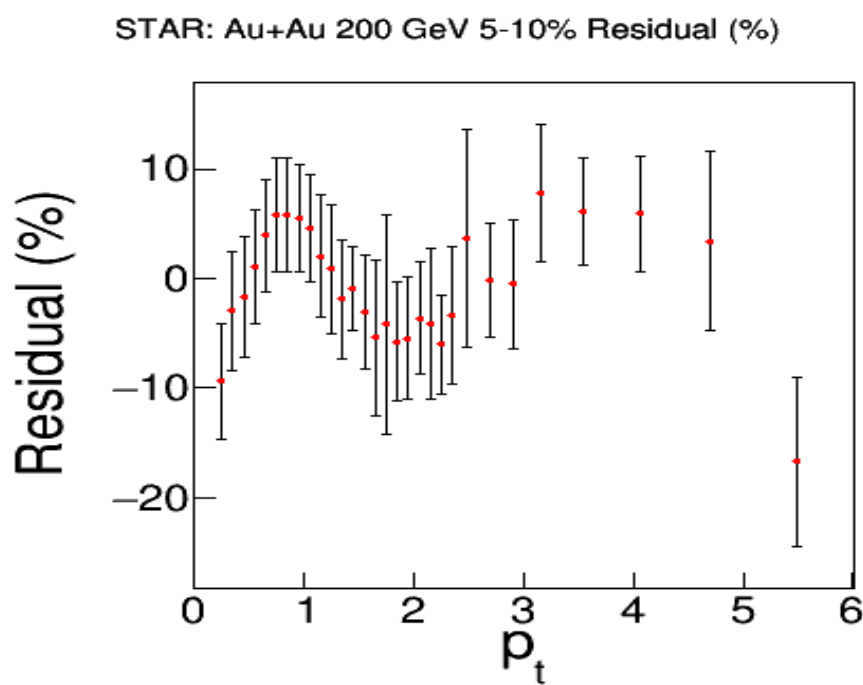
STAR: Au+Au 200 GeV 10-20% Residual (%)



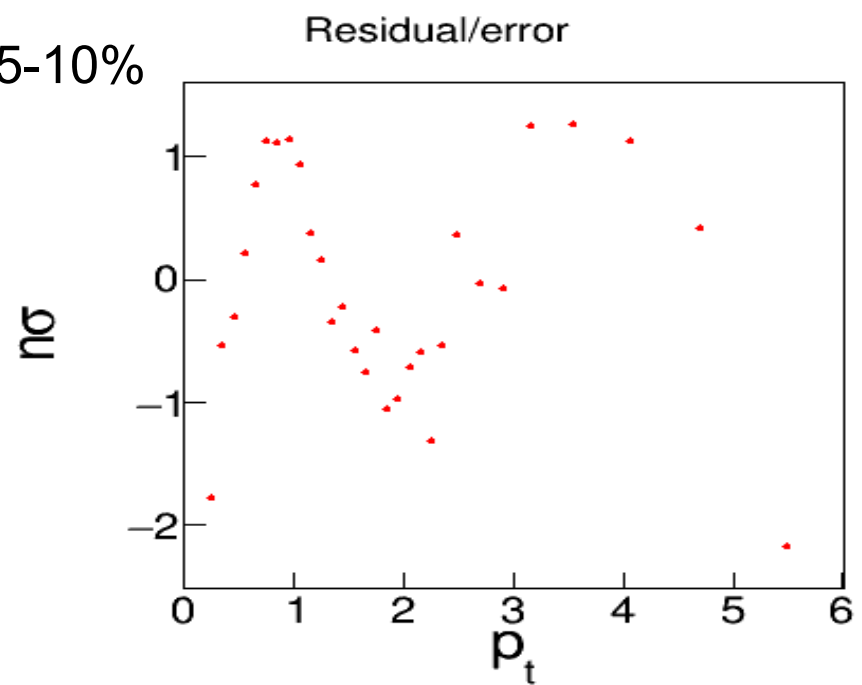
STAR: 10-20%



Residual/error

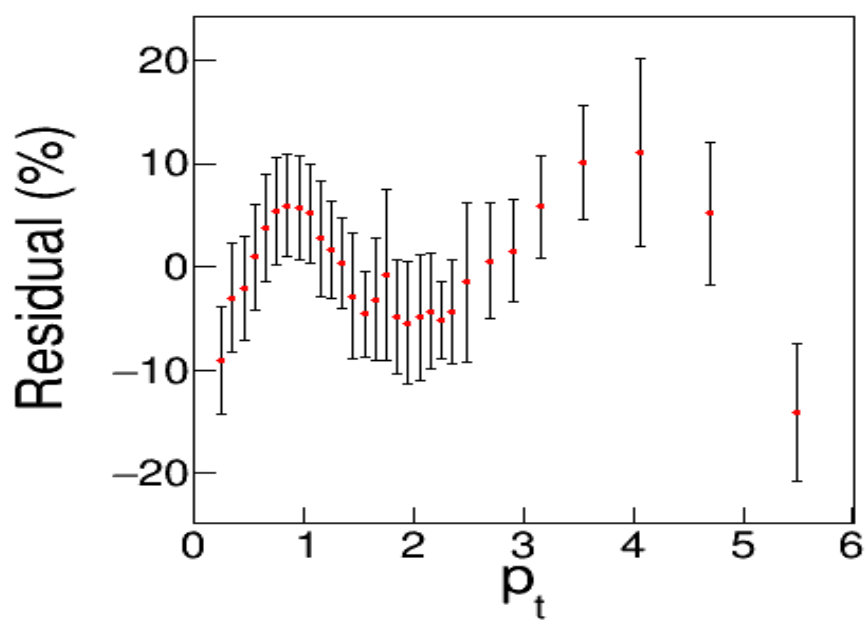


STAR: 5-10%

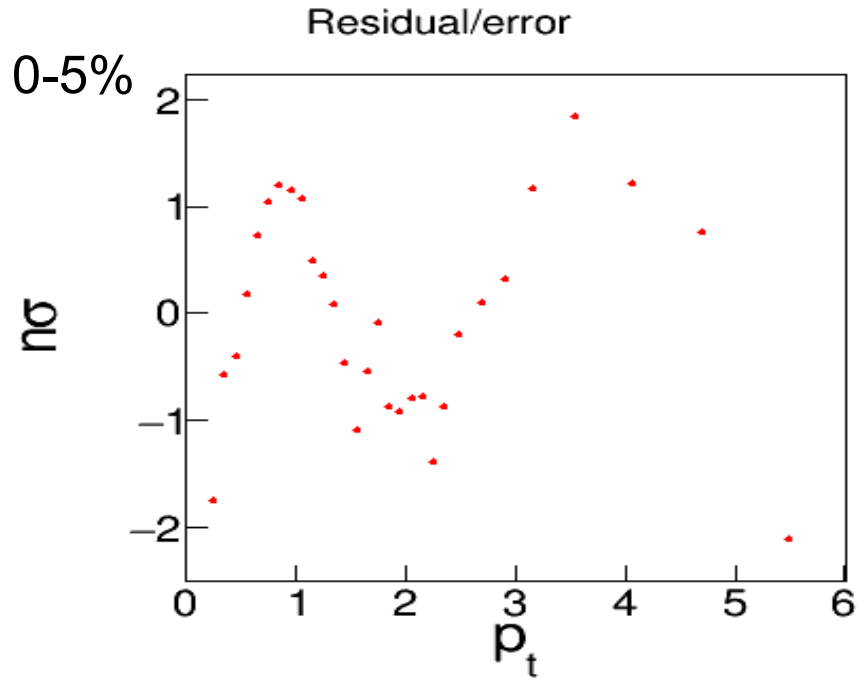


Residual/error

STAR: Au+Au 200 GeV 0-5% Residual (%)



STAR: 0-5%



Although a systematic shape difference appears between the Levy model fit residuals for the STAR spectra data, all are within about 1-sigma. No additional systematic error will be included here.

Final systematic uncertainty in *Pre-Factor*:

The uncertainties in $dN_{ch}/d\eta$ from STAR are:

Centrality	70-80%	60-70%	50-60%	40-50%	30-40%	20-30%	10-20%	5-10%	0-5%
Error (%)	9.1	6.7	7.7	7.1	7.2	7.0	7.1	7.2	7.1

For the analysis in STAR, Phys. Rev. C **86**, 064902 (2012), the companion paper on 2D angular correlations, the $dN_{ch}/d\eta$ values were estimated using a Monte-Carlo Glauber model fit to the above, STAR $dN_{ch}/d\eta$ values after accounting for trigger and primary vertex finding inefficiencies. The assumed values are listed in Table III of the preceding reference and are repeated here for convenience. The corresponding uncertainties, interpolated from the above errors are taken to be:

Centrality	84-93%	74-84%	64-74%	55-64%	46-55%	38-46%	28-38%	18-28%	9-18%	5-9%	0-5%
Bin #	0	1	2	3	4	5	6	7	8	9	10
$dN_{ch}/d\eta$	5.2	13.9	28.8	52.8	89	139	209	307	440	564	671
Error (%)	10.	9.3	8.6	8.0	7.6	7.4	7.2	7.2	7.2	7.2	7.2

From the Monte-Carlo Glauber analysis in STAR, Phys. Rev. C **86**, 064902 (2012) the uncertainties in the centrality cross section percentage assignments were estimated to be about ± 1 to 2%.

The above systematic uncertainties are the only ones assumed for the charged-particle pre-factor. This normalization error is added in quadrature with the other eight systematic error sources for the final, total systematic uncertainty in $\Delta\rho/\sqrt{\rho_{chrg}}$.

Systematic Uncertainties for the other azimuthal and charge-pair selected Pre-Factors:

All pre-factors in the (y_t, y_t) correlation analysis are based on the all azimuth, charge-independent pre-factor discussed in this document. Multiplicative factors of 1, $1/\sqrt{2}$ and $\frac{1}{2}$ are applied for all other projections of relative azimuthal angle, i.e. all angles, near-side, away-side, and for all combinations of charge-pair selections, i.e. all charge pairs, like-sign and unlike-sign. The multiplicative factors account for the reduced number of pairs used in each selection.